Predicting response to immunotherapy in metastatic melanoma by a personalized mathematical model

Von der Fakultät Energie-, Verfahrens- und Biotechnik der Universität Stuttgart

zur Erlangung der Würde eines

Doktors der Naturwissenschaften (Dr. rer. nat.) genehmigte Abhandlung

Vorgelegt von

Neta Tsur

aus Ramat Gan

Hauptberichter: Prof. Dr. Markus Morrison

Mitberichter: Prof. Dr. Thomas Sauter, Universität Luxemburg

Tag der mündlichen Prüfung: 18.06.2020

Institut für Zellbiologie und Immunologie der Universität Stuttgart
2020

Abstract

At present, immune checkpoint inhibitors, such as pembrolizumab, are widely used for the treatment of advanced non resectable melanoma, as they induce more durable responses than other available treatments. However, the overall response rate does not exceed 50%, and prediction of the individual benefit of patients from these therapeutics remains an unmet clinical need. Mathematical models that predict the response of patients with advanced melanoma to immune checkpoint inhibitors can contribute to better informed clinical decisions. The aim of this work was to develop a new personalization algorithm for predicting time to disease progression under pembrolizumab treatment, based on personal mathematical models of patients with advanced melanoma. First, a simple mathematical model was developed for describing the interactions of an advanced melanoma tumor with both the patient's immune system and the immunotherapeutic drug, pembrolizumab. The local and global dynamics of the treatment-free model was analyzed analytically and numerically. The complete model was then implemented in conjunction with clinical pre-treatment data, in an algorithm which enables prediction of the personal response to the drug. To develop the algorithm, clinical data of 54 patients with advanced melanoma under pembrolizumab were collected retrospectively. In the following, clinical parameters before checkpoint inhibition and in the early course of pembrolizumab treatment were correlated to the mathematical model parameters. Using the algorithm together with the longitudinal tumor burden of each patient, the personal mathematical models were identified and used in simulations to predict the patient's time to progression. The prediction capacity of the algorithm was validated by the Leave-One-Out cross validation methodology. The results show that zero, one, or two steady states of the treatment-free mathematical model exist in the phase plane, depending on the parameter values of individual patients. Without treatment, the simulated tumors grew uncontrollably. At increased efficacy of the immune system, i.e. due to immunotherapy, two steady states were found, one leading to uncontrollable tumor growth, whereas the other resulted in tumor size stabilization. The model analysis indicates that a sufficient increase in the activation of $CD8^+$ T cells

results in stable disease, whereas a significant reduction in T-cell exhaustion, which indirectly promotes $CD8^+$ T cell activity, entails a temporal reduction in the tumor mass, but fails to control disease progression in the long run. Importantly, the initial tumor burden influences the in-treatment dynamics: small tumors responded better to treatment than larger tumors. Among the analyzed clinical parameters, the baseline tumor load, the Breslow tumor thickness, and the status of nodular melanoma were significantly correlated with the activation and exhaustion rates of $CD8^+$ T cells. Using the measurements of these correlates to personalize the mathematical model, the time to progression of individual patients was predicted (Cohen's $\kappa = 0.489$). Comparison of the predicted and clinical time to progression in patients progressing during the follow-up period showed moderate accuracy ($R^2=0.505$). The treatment-free model analysis suggests that disease progression and response to immune checkpoint inhibitors depend on the ratio between activation and exhaustion rates of $CD8^+$ T cells as well as the tumor growth rate. This analysis provides a foundation for the use of computational methods to personalize immunotherapy. Furthermore, the results suggest that a relatively simple mathematical mechanistic model, implemented in a computational algorithm, can be personalized by baseline clinical data before immunotherapy onset. The algorithm, currently yielding moderately accurate predictions of individual patients' response to pembrolizumab, can be improved by using a larger number of patient files. Validation of the algorithm by an independent clinical dataset will enable its use as a tool for treatment personalization.

Zusammenfassung

Derzeit werden Immun-Checkpoint-Inhibitoren wie Pembrolizumab häufig zur Behandlung fortgeschrittener, nicht-resektabler Melanome eingesetzt, da sie zu einer dauerhafteren Ansprache auf die Therapie führen als andere verfügbare Behandlungen. Die Gesamtansprechrate liegt jedoch nicht über 50% und die Vorhersage des individuellen Patientennutzens dieser Therapeutika bleibt eine unerfüllte klinische Notwendigkeit. Mathematische Modelle, die das Ansprechen von Patienten mit fortgeschrittenem Melanom auf Immun-Checkpoint-Inhibitoren vorhersagen, können die fundierte klinische Entscheidungsfindung verbessern. Das Ziel der vorliegenden Arbeit war es, basierend auf persönlichen mathematischen Modellen von Patienten mit fortgeschrittenem Melanom, einen neuen Personalisierungsalgorithmus zur Vorhersage der progressionsfreien Zeit unter Pembrolizumab zu entwickeln. Zunächst wurde ein einfaches mathematisches Modell entwickelt, das die Wechselwirkungen des Tumors mit dem Immunsystem des Patienten und dem Checkpoint-Inhibitor Pembrolizumab beschreibt. Die lokale und globale Dynamik des behandlungsfreien Modells wurde analytisch und numerisch analysiert. Das komplette Modell wurde dann in Verbindung mit den Daten der klinischen Vorbehandlung in einem Algorithmus implementiert, der die Vorhersage des individuellen Ansprechens auf das Medikament ermöglicht. Zur Entwicklung des Algorithmus wurden retrospektiv klinische Daten von 54 Patienten mit fortgeschrittenem Melanom unter Behandlung mit Pembrolizumab erhoben. Anschließend wurden klinische Parameter vor Behandlungsbeginn sowie aus einem frühen Behandlungsstadium mit den mathematischen Modellparametern korreliert. Mithilfe des Algorithmus und des zeitlichen Verlaufs der Tumorlast jedes Patienten wurden die persönlichen mathematischen Modelle identifiziert und verwendet, um in Simulationen das progressionsfreie Überleben vorherzusagen. Die Vorhersagekapazität des Algorithmus wurde durch die „Leave-One-Out“-Cross-Validierungsmethode gemessen. Die Ergebnisse zeigen, dass abhängig von den Parameterwerten der einzelnen Patienten, null, ein oder zwei stationäre Zustände des behandlungsfreien mathematischen Modells in der Phasenebene existieren. Ohne

Behandlung wuchsen die simulierten Tumore unkontrolliert. Bei erhöhter Wirksamkeit des Immunsystems, d.h. durch Immuntherapie, wurden zwei stationäre Zustände gefunden. Einer führte zu unkontrollierbarem Tumorwachstum, der andere zu einer Stabilisierung der Tumorgröße. Die Modellanalyse zeigt, dass ein ausreichender Anstieg der Aktivierung von $CD8^+$ T-Zellen zu einer Stabilisierung der Erkrankung führt, während eine signifikante Reduktion der T-cell exhaustion, die indirekt die Aktivität von $CD8^+$ T-Zellen steigert, eine vorübergehende Reduktion der Tumormasse zur Folge hat, das Fortschreiten der Erkrankung jedoch nicht langfristig kontrolliert. Wesentlich ist dabei, dass die anfängliche Tumorlast die Dynamik während der Behandlung beeinflusst: Kleine Tumore reagierten besser auf die Behandlung als größere Tumore. Von den analysierten klinischen Parametern sind die initiale Tumorgrundlast, die Breslow-Tumordicke und der Status des nodulären Melanoms signifikant mit den Aktivierungs- und exhaustion-Raten von $CD8^+$ T-Zellen korreliert. Anhand der Messungen dieser Korrelationen zur Personalisierung des mathematischen Modells wurde die progressionsfreie Zeit einzelner Patienten vorhergesagt (Cohens $\kappa = 0{,}489$). Der Vergleich der vorhergesagten und der tatsächlichen Zeit bis zur Progression bei Patienten, die in der Nachfolgezeit fortschreiten, zeigte eine moderate Genauigkeit ($R^2=0{,}505$). Die behandlungsfreie Modellanalyse deutet darauf hin, dass das Fortschreiten der Erkrankung und die Reaktion auf Immun-Checkpoint-Inhibitoren vom Verhältnis zwischen Aktivierungs- und exhaustion-Raten der $CD8^+$ T-Zellen sowie der Tumorwachstumsrate abhängen. Diese Analyse bietet eine Grundlage für den Einsatz von Berechnungsmethoden zur Personalisierung der Immuntherapie. Darüber hinaus deuten die Ergebnisse darauf hin, dass ein relativ einfaches, mathematisch-mechanistisches Modell, das in einem Computeralgorithmus implementiert ist, durch klinische Basisdaten vor Beginn der Immuntherapie personalisiert werden kann. Der Algorithmus, der derzeit mäßig genaue Vorhersagen über die Reaktion einzelner Patienten auf Pembrolizumab liefert, kann durch die Verwendung einer größeren Anzahl von Patientenakten verbessert werden. Die Validierung des Algorithmus durch einen unabhängigen klinischen Datensatz wird seine Verwendung als Werkzeug zur Personalisierung der Behandlung ermöglichen.

Table of Contents

Abbreviations

ADT Androgen deprivation therapy

AJCC American Joint Committee on Cancer

α-MSH Melanocyte-stimulating hormone

APCs Antigen-presenting cells

CRP C-reactive protein

CT Computed tomography

CTL Cytotoxic T cell

CTLA-4 Cytotoxic T-lymphocyte antigen 4

DC Dendritic cell

FAMMM Familial atypical multiple mole melanoma syndrome

FP Fixed point

HDI Human development index

HMC Hadassah Medical Center

HTLV-1 Human T cell leukemia virus type 1

IARC International Agency for Research on Cancer

ICI Immune checkpoint inhibitor

irRECIST Immune-related RECIST

k-NN k-Nearest Neighbors

LAS Locally asymptotically stable

LDH Lactate dehydrogenase

L.h.s Left-hand side

LN Lymph node

LOO CV Leave-One-Out cross validation

LY% Relative counts of blood lymphocytes

MAGE Melanoma-associated antigen

MC1R Melanocortin receptor 1

MDSC Myeloid-derived suppressor cell

MEL PLEX MELanoma disease comPLEXity network

MHC Major histocompatibility complex

MRI Magnetic resonance imaging

NK cells Natural killer cells

ORR Overall response rate

OS Overall survival

PD Progressive disease

PD-1 Programmed cell death 1

PD-L1 Programmed death-ligand 1

PD-L2 Programmed cell death ligand 2

Pembro Pembrolizumab

PET-CT Positron emission tomography CT

PFP Positive fixed point

POMC Proopiomelanocortin peptide

PSA Prostate specific antigen

RECIST 1.1 Response Evaluation Criteria In Solid Tumors 1.1

R.h.s Right-hand side

ROC Receiver operating characteristic

SOC Standard of care

SOD Sum of diameters

SSE Sum of squared errors

TCR T cell receptor

TILs Tumor infiltrating lymphocytes

TTP Time to progression

UMM University Medical Centre Mannheim

UVR Ultraviolet radiation

XP Xeroderma pigmentosum

1. Introduction

This section provides background about the immune system, cancer and its interaction with the immune system, melanoma, immunotherapy of melanoma, and the use of mathematical models for outcome prediction.

1.1. The immune system and its defense mechanisms

The human immune system consists of blood cells and organ complexes, which recognize and provide protection against pathogens, but also respond to damaged tissues and transformed cells, out of which otherwise cancers might arise. Pathogens include non-self and harmful particles, such as bacteria, viruses, and fungi. They contain molecular structures, which can be recognized as “non-self”. These structures can serve as non-self-antigens and stimulate the immune system to dismiss the pathogens. Similarly, intracellular content spilled by cells in damaged tissues, or altered surface structures of transformed potential cancer cells can be recognized as non-self. Communication between immune cells and other cells in the body is mediated by secretable proteins, called cytokines, which affect intracellular processes and can change properties of cells, such as accelerating cell proliferation, directing immune cells to their target cells or molecules, and regulating the infection after elimination of most of the harmful factors. An immune response to remove or eliminate pathogens in vertebrates consists of two main stages, including an innate response, and an adaptive response.

1.1.1. Innate versus adaptive immunity

At first, the immune system blocks invasion of pathogens by physical barriers. These include the skin, hair, cilia, as well as mucosal tissues lining the respiratory and gastrointestinal tracts [1-4]. Invasion of a pathogen into the body initiates an immediate innate response, which begins early after exposure. The response is rapid, non-specific, and can provide protection during the first week after infection. The adaptive immune response requires four to seven days after pathogen invasion for substantial activation and active responses, and plays a key role if the innate immune

response is evaded. This type of response is more complex and sophisticated, and involves processes that are directed in a highly specific manner against pathogen-derived antigens. There are two classes of both innate and adaptive defense mechanisms, which provide protection in different parts of the body. One is the humoral defense, and the other is the cellular defense. The following paragraphs describe both of these defense mechanisms.

1.1.2. Humoral immune response

This type of response provides protection against circulating pathogens in the extracellular space, the blood system and body fluids. One of the main components of humoral immunity are molecules called antibodies or immunoglobulins, which bind to non-self-antigens and make them recognizable by the innate and adaptive immune system. These molecules have a “Y” shape, with a constant region on the stem of the “Y”, and a variable region on the “arms” of the “Y”. The constant region can have four or five biochemical forms (isotypes). The isotypes define the class of the antibody and determine the pathogen disposal mechanism. The variable region appears in an infinite variety of forms. It is identical in each side of the antibody, and determines the specific receptor on the pathogen, to which the antibody can bind [5].

Antibodies bind to pathogens and mark them as dangerous by different mechanisms, called neutralization, opsonization, activation of the complement, and antimicrobial activity [6]. Neutralization means binding of antibodies to pathogens, preventing them from entering into cells. Opsonization, also called coating, refers to binding of immune cells to pathogens, by antibodies. In addition, antibodies can activate the complement system, which consists of plasma proteins that signal information about the pathogen to different immune cells. Additionally to marking, antibodies can induce internal changes in the structure and function of pathogens.

The humoral innate response is composed of several components, each having a different function [7]. First are the complement proteins, which induce recruitment of immune cells that bind to pathogens and coat them [8]. Second is the coagulation system, which entails clotting of the infected area. Third are different proteins, called pentraxins, which activate different mechanisms of the innate immunity. Among them

is the C-reactive protein (CRP), which is responsible for reducing inflammation and inducing the adaptive immune response [9]. Lastly, naturally occurring antibodies circulate in the body to provide a non-specific protection against a wide variety of pathogens.

The humoral adaptive response is mediated by B cells, or B lymphocytes, which produce antigen-specific antibodies, and release them into the blood sera [5]. The activation mechanism of B cells is termed clonal selection theory, and is based on the following principles [5, 10]:

1. Each lymphocyte has one type of receptor with a specific binding characteristic.
2. Each lymphocyte becomes activated upon binding to an antigen with high affinity to its specific receptor. This results in proliferation and clones of daughter lymphocytes.
3. Daughter cells express the same specific receptor like the parental cell.
4. Central tolerance (clonal deletion): self-molecules are identified in the embryo stage and self-reactive cells are eliminated from the system to prevent autoimmunity.

In case the humoral immune response is not sufficient, the infection may become intracellular and initiate a cellular immune response.

1.1.3. Cellular immune response

The cellular immunity provides protection against intracellular pathogens and involves the activation of white blood cells, also called leukocytes. These cells are generated in the bone marrow from stem cells. They divide into three different precursors named granulocytes, monocytes, and lymphocytes, each having a distinct structure. Every precursor further divides into different types of cells, as summarized in Figure 1.1.

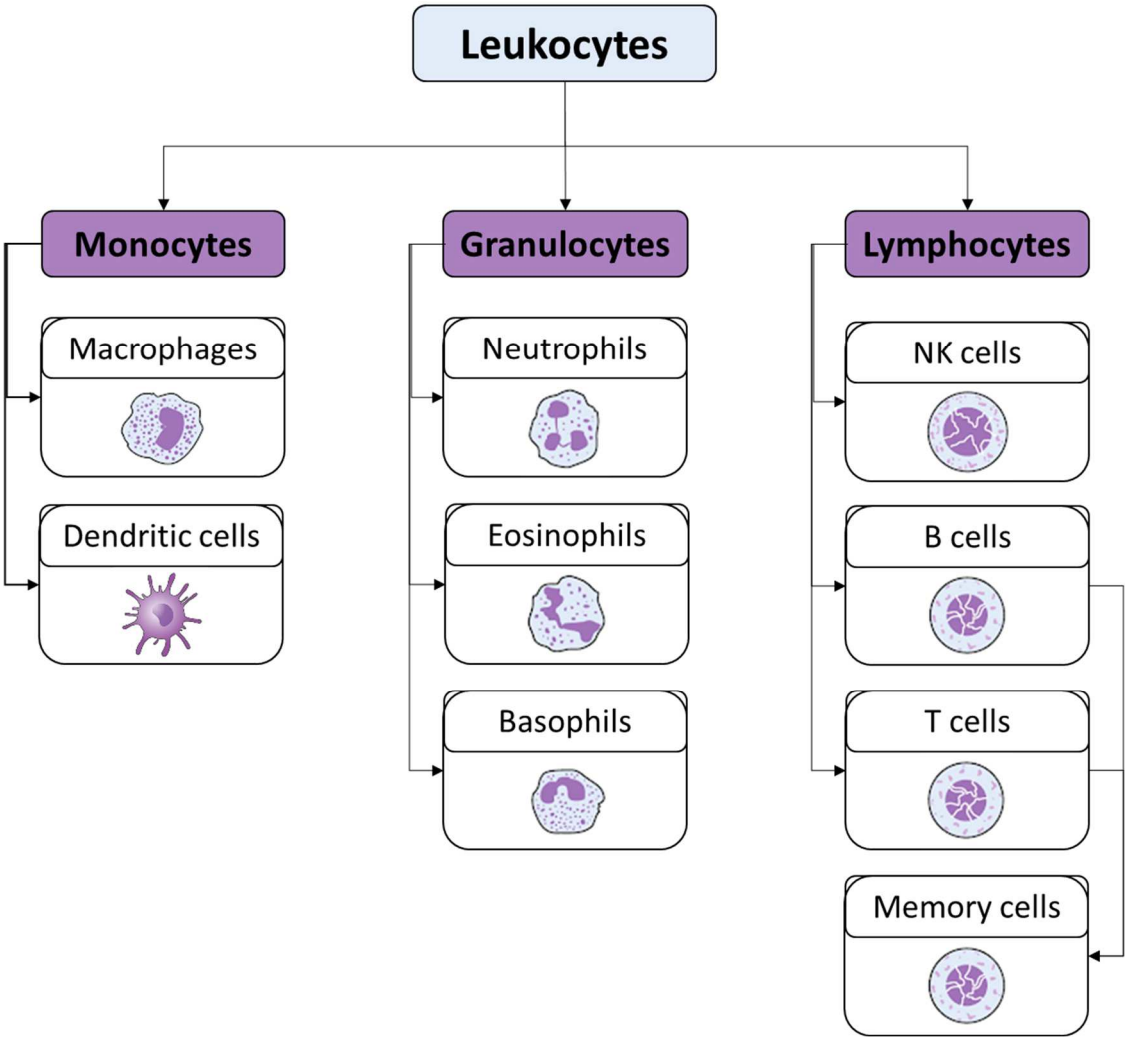

Figure 1.1. Overview of different types of white blood cells (leukocytes).
This lineage tree is simplified and introduces mostly those cell populations relevant in the context of this thesis. NK stands for natural killer. Cell illustrations were adapted from [11] and [12].

The cellular innate immune response is mostly mediated by monocytes and granulocytes, which are generated and developed in the bone marrow. Monocytes constitute 5% - 10% of the leukocytes in the peripheral blood [13]. They usually circulate in the blood system for 24-48 hours. Afterwards most of them migrate into tissues, and remove pathogens by cellular ingestion, termed phagocytosis [14]. They display the remnants of the ingested pathogens as antigens on their surface, thus are also known as antigen-presenting cells (APCs). Inside the tissues, monocytes develop into macrophages and dendritic cells (DCs). Macrophages constitute a major component of tumor infiltrating leukocytes. They destroy intracellular invaders, induce tumor necrosis, and contribute to tissue repair [15, 16]. It is common to

distinguish two types of macrophages. The M1 type is known for their anti-tumor effects, and the M2 is known as a pro-tumorigenesis type [17]. The other subgroup of monocytes, DCs, migrate from the tissues into the lymph system, where they play a major role in antigen presentation to lymphocytes, including $CD8^+$ T cells [18]. In addition, DCs secrete different cytokines, which induce activation and recruitment of other cell types, such as granulocytes, to the infection site [19].

Granulocytes are named after their characteristic nuclear morphology, which contains multi-cytoplasmic granules and secretory vesicles. They play a major role in the elimination of pathogens that are too large to be ingested by phagocytes, by surrounding them and secreting digestive enzymes. The most common type of granulocytes are neutrophils, which constitute 50% - 70% of the leukocytes [20]. Neutrophils eliminate a variety of pathogens and tumor cells by phagocytosis. However, elevated levels of circulating neutrophils are associated with poor cancer prognosis [21]. Only part of them, called N1 neutrophils, are associated with tumor control, while N2 neutrophils are a pro-tumor phenotype [22]. Eosinophils are mostly responsible for destruction of parasites. In cancer, a large eosinophilic infiltrate is associated with good prognosis [23]. Basophils are mainly responsible for regulation of allergic reactions and parasitic intrusions [24]. Infiltration of basophils into tumors is associated with increased activity of $CD8^+$ T cells [25]. The latter play a major role in the elimination of melanoma cells, as will be described later in this chapter.

Lymphocytes constitute 20% to 45% of the white blood cells [26]. They originate from primary lymphoid organs, including the bone marrow (B cells and natural killer cells) and the thymus (T cells). Natural killer (NK) cells participate in the innate immune response [27] and interact with APCs and T cells to regulate their activity [28, 29]. The other types of lymphocytes, namely T cells and B cells, are assigned to identify specific antigens. They provide a pathogen-specific protection in frame of the cellular adaptive immune response. As mentioned above, B cells participate in the humoral immune response, while T cells play an important role in the cellular-mediated immunity. These cells circulate through the secondary lymphoid organs (spleen, lymph nodes (LNs), and mucosal-associated lymphoid tissues), where they are introduced to

different antigens, become activated, and proliferate according to the abovementioned clonal selection theory.

The activation of T cells follows the antigen presentation by APCs, which migrate from the site of infection to the lymphoid organs, where they interact with the T cells. The non-self-particles that are digested by an APC, are captured by certain proteins, called major histocompatibility complex (MHC) molecules. These molecules present the digested peptides to the T cell receptor (TCR) on the surface of T cells. The form of the TCR is specific for each T cell, thus recognition of a particular peptide depends on its affinity to the specific TCR. The recognition results in binding between the TCR and the MHC molecule, and formation of a conjugate between the T cell and the APC, also called specific adhesion. In order to initiate the T cell response, co-stimulation by binding of the CD28 receptor on the T cell, which binds to its ligands B7-1 (CD80), or B7-2 (CD86) on the APC is required [30]. This mechanism prevents autoimmune reactions, since imperfection in the clonal deletion of T cells in the embryo stage may leave T cells in the lymphoid tissues which recognize self-peptides. The co-stimulation signal induces T cell responses only in cases of a “threat recognition” by APCs. Absence of this signal leads to anergy, i.e., a failed reaction of a T cell to an antigen. The T cell-APC junction formed during the activation is called the immunological synapse. This interface contains different proteins, such as receptors and adhesion molecules, which regulate the balance between immune evasion and autoimmunity [31].

The population of T cells is divided into $CD8^+$ T cells and $CD4^+$ T cells. $CD8^+$ T cells – also called cytotoxic T cells, CTLs, or effector cells, kill a variety of infected and damaged cells, including cancerous cells. As explained above, the type of the target cell each CTL can eliminate depends on the specification of its TCR. The killing mechanism of CTLs involves secretion of lytic granules into the immunological synapse, which cling to the target cell, release their toxic content, and induce apoptosis [32]. While $CD8^+$ T cells specify in destroying target cells, $CD4^+$ T cells, also called T-helper cells, participate in activation and recruitment of other immune cells, including $CD8^+$ T cells, during all types of infections. While DCs can directly activate naïve $CD8^+$ T cells, other APCs, such as macrophages, entail specific adhesion, but their costimulatory signal is not strong enough to activate the $CD8^+$ T cells. Effector $CD4^+$ T cells recognize their

specific peptides on the APCs and become activated upon binding to it, which thereby enhances the stimulation of the naïve $CD8^+$ T cell. Furthermore, T-helper cells take part in the immune response against allergens and activation of B cells to mediate long-lived antibody responses.

Besides effector functions, which are necessary for defense, there exist multiple mechanisms, which tone down the T cell-mediated response in order to prevent autoimmunity. Among them are inhibitory receptors on the T cells, which bind to different ligands on APCs and other cells, such as tumor cells, and induce regulatory signals on the T cells [33, 34]. Two pathways, namely the cytotoxic T lymphocyte antigen 4 (CTLA-4) pathway, and the programmed cell death 1 (PD-1) pathway, serve as targets for immunotherapy. Since the response to immune therapies targeting these pathways is the focus of my dissertation, I will provide a summary of the regulatory role of the CTLA-4 and PD-1 pathways. Visualization of the signaling concept of both pathways is shown in Figure 1.2. According to Jago et al. 2004 [35] and Walker et al. 2011 [36] CTLA-4 in naïve T cells is found in a soluble state, isolated in intracellular vesicles. Stimulation of the TCR by APCs entails deposition of CTLA-4 to the cell surface [37, 38]. The amount of expressed CTLA-4 receptors depends on the strength of the specific adhesion between the TCR and MHC molecule [39]. The CTLA-4 receptor is more similar to B7 than CD28, thus CTLA-4 can bind to B7 and physically block the co-stimulation signal [40]. Besides that, CTLA-4 expressed on one T cell can also inhibit the activation of other T cells [36].

Besides the CTLA-4 pathway, the PD-1 pathway plays a role in the regulation of activated T cells. This pathway is triggered by binding of PD-1 to its ligands: programmed cell death ligand 1 (PD-L1), and programmed cell death ligand 2 (PD-L2), which are expressed on different cells, such as activated APCs and cancerous cells [41, 42]. The inhibitory signal induced by upregulation of PD-1 has both strengthening and weakening influence on the effector function of T cells [43]. On the one hand, it downregulates T cell priming to prevent over-activation and plays a role in clonal deletion of T cells that recognize self-antigens. Moreover, following infection clearance, the PD-1 pathway limits the T cell response to prevent destruction of tissues. On the other hand, in case of persisting presence of antigens, which can be

caused by chronic infections or cancer, the PD-1 pathway induces T cell exhaustion, during which the T cell loses its effector function. At the end, this pathway helps to return the body to homeostasis.

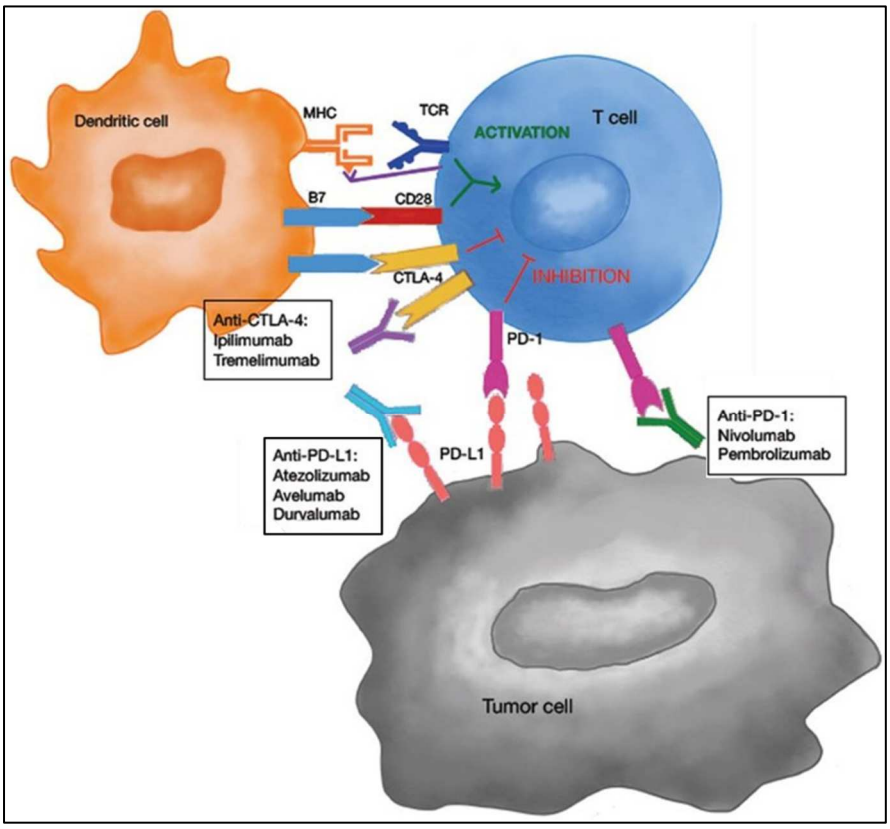

Figure 1.2. The CTLA-4 and PD-1 pathways.
Activation of T cells by APC involves two signals. It is composed of MHC:TCR binding, where the MHC molecules present specific peptides, which are recognized by the TCR, whose form matches the presented antigen. The other signal is induced by binding between CD28 and CD80/CD86 (B7). CTLA-4 competes with CD28 on the B7 ligand. Its binding to B7 leads to inhibition of the T cells, which regulates the immune response. Furthermore, binding between PD-1 and its ligands PD-L1 and PD-L2, which are expressed on tumor cells, also leads to inhibition of the T cell. Both CTLA-4 and PD-1 pathways are targeted by different drugs, which are listed in the small frames. Figure is adapted from Muñoz-Unceta et al. [44].

As part of the adaptive immune response, a small number of antigen-specific B and T lymphocytes remain in the host to build up immunological memory. In case of repeated antigen exposure, such memory cells enable a stronger repetitive reaction of the immune system. Memory cells can retain their effector functions for decades but need to be reactivated in order to respond. Activated memory B cells rapidly produce antibodies with high affinity to the specific antigen they are exposed to.

Activated memory T cells are divided into two subsets: central memory T cells, and effector memory T cells. Each subset has a different nature of homing and effector functions [45]: Upon activation, effector memory T cells acquire effector function and migrate to infected tissues, while central memory cells home to secondary lymphoid organs, and can proliferate and differentiate into effector T cells after antigen encounter.

In summary, the immune response is comprised of many mechanisms and elements, which interact to clear multiple causes of infection. Some of these defense mechanisms provide unspecific protection, while others are aimed to eliminate specific threats. Moreover, different types of immune responses control infection inside the host cells and in the extracellular fluids.

1.2. Cancer statistics and tumor antigenicity

Cancer is one of the most fatal diseases worldwide. According to the International Agency for Research on Cancer (IARC), around 18.1 million new incidences were diagnosed in 2018. Of these, 48.4% were diagnosed in Asia, 23.4% in Europe, 21% in America, 5.8% in Africa and 1.4% cases were diagnosed in Oceania. Furthermore, 9.6 million deaths were reported worldwide in 2018. The most common cancer indications diagnosed last year were lung cancer, female breast cancer, and colorectal cancer. The top five deadly cancer indications in 2018 were lung cancer, colorectal cancer, stomach cancer, liver cancer, and female breast cancer. The most common cancer diagnosis in men and women were lung and breast, respectively. These cancer types were also responsible for most of the deaths in the respective sexes. In addition, the overall incidence rate was significantly higher in countries with a high human development index (HDI), compared to countries with a medium or low HDI [46].

Cancer is caused by an uncontrollable growth of mutated somatic cells. Normally, failed repair of DNA mutations can induce autonomous programmed cell death (apoptosis). Cells with a multiplicity of growth promoting mutations can become cancerous, proliferate faster and form a benign tumor. The last has similar characteristics to healthy tissue and can be usually removed by a surgery. Further malignant transformation leads to expansion out of the tissue, angiogenesis,

penetration of tumor cells into the blood and lymph systems, and metastasis formation. In particular metastasized tumors cannot easily be operated on and require systemic treatment, according to the American Cancer Society (https://www.cancer.org/treatment/understanding-your-diagnosis/advanced-cancer/treatment.html).

Tumor cells can express different antigens, which can be identified by the immune system. The antigens can be produced by several causes, as summarized by Blankenstein et al. [47]. First are cancer germline antigen genes, such as melanoma-associated antigen (MAGE), which are not expressed in healthy tissues, and therefore can be recognized by the immune system as non-self. Second, genetic mutations can cause the expression of altered surface proteins. Third, oncogenic viruses, such as helicobacter pylori and human papilloma virus (HPV) can induce the expression of unique peptides in infected cells. Lastly, tissue-specific genes are sometimes overexpressed, notably in melanoma and prostate cancer. Even though all tumors would be expected to express antigen signatures, their level of expression differs between different cancer types [48]. As shown in Figure 1.3, melanoma tumors, which are in the focus of this thesis, tend to express the strong antigen profiles. Moreover, other cancers, or cancer subtypes, which tend to contain more than 10 somatic mutations per megabase, are considered to present more antigens than other cancers with lower mutational loads. Thus, their antigenicity, as well as their ability or probability to elicit immune responses, are higher [48]. Besides melanoma, these cancer indications include all the most commonly diagnosed ones in 2018, namely lung cancer, breast cancer, and colorectal cancer, according to the IARC.

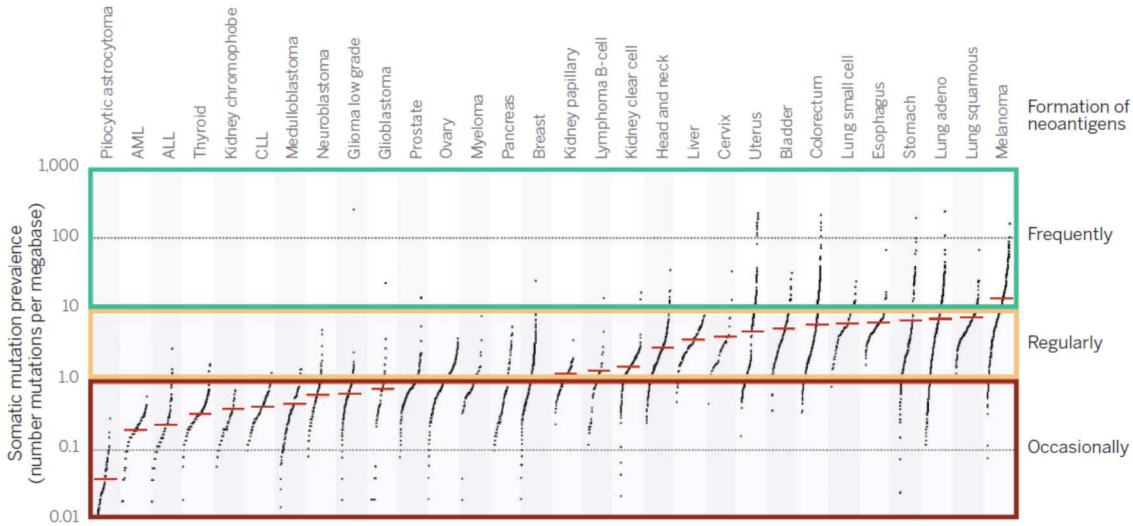

Figure 1.3. Antigenicity of different tumor types.
The left axis represents the level of expression of somatic mutations, and the right axis shows the corresponding likelihood of antigen formation. Adapted from Schumacher et al. [48].

1.3. Melanoma

Advanced melanoma is the most deadly skin cancer, with a total of 288,000 new incidences, and 61,000 deaths worldwide in 2018, according to IARC. Out of the 35 most common cancer indications last year, melanoma is ranked the 20th cancer in the number of new cases, and 23rd place in the number of deaths. While early-detected melanoma is mostly curable [49, 50], advanced melanoma with metastases is associated with poor prognosis and survival.

1.3.1. Development and risk factors of melanoma

Melanoma is caused by mutations in melanocytes, which produce the pigment melanin. Normally, melanin is transferred from melanocytes to keratinocytes in the so-called tanning mechanism, to absorb the harmful ultraviolet radiation (UVR) from the sun. As a result, the UVR damages the DNA in keratinocytes, which leads to activation of the protein p53 in keratinocytes, up-regulation of the proopiomelanocortin peptide (POMC), and secretion of its downstream product α-Melanocyte-stimulating hormone (α-MSH). The latter stimulates the melanocortin receptor 1 (MC1R) on the neighboring melanocytes, and as a result, melanin is synthesized and secreted out of the melanocytes in vesicles, called melanosomes. These melanosomes enter into the keratinocytes, which tans the skin [51, 52].

Development of melanoma is classically described by the Clark model [52, 53], which outlines the transformation of melanocytes to metastatic melanoma in five steps (Figure 1.4). In the first step, melanocytes proliferate to a colony and form a benign nevus. In the second step, a pre-existing or a new nevus turns into a multi-colored cutaneous lesion, also called dysplastic nevus, with asymmetric borders, and increasing diameter. In the third step, also called radial-growth phase, the lesion spreads into the dermis, and turns into a tumor. The radial phase is usually slow and can be cured by resection. In the fourth step tumor cells grow vertically, further invade into the dermis, and begin to metastasize. In the last step, tumor cells spread to other skin parts and other organs, and form expansile nodules.

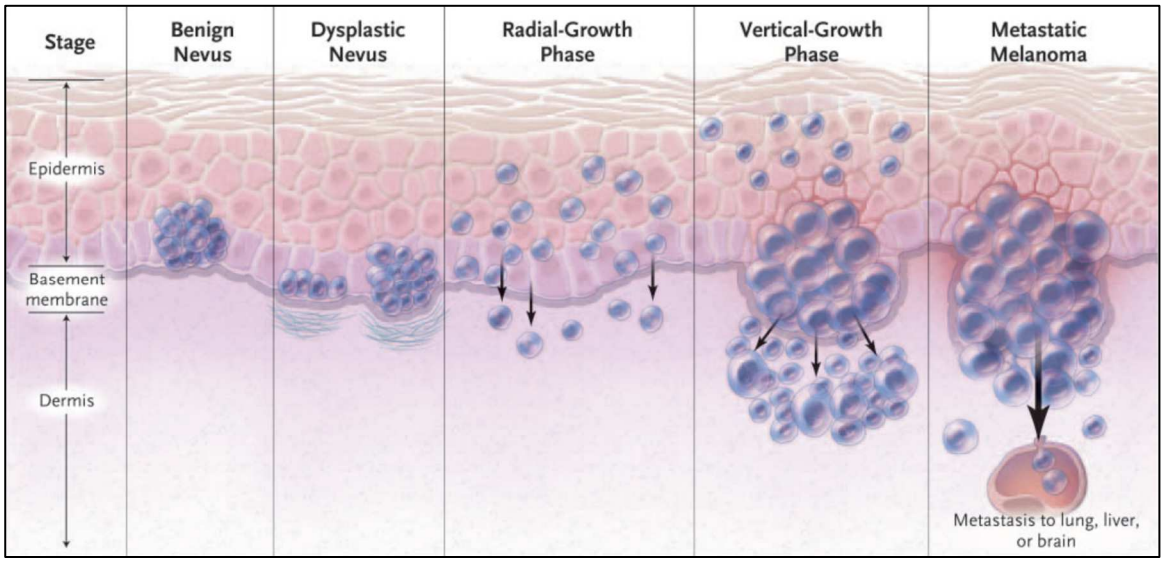

Figure 1.4. Melanoma development, according to the Clark model.
The disease development is shown from left to right, on a vertical section of the skin. In the first step, melanocytes proliferate to form a benign nevus, which is limited to the epidermis. Further proliferation of the melanocytes may turn the lesion into a dysplastic nevus, which is multi-colored and has asymmetric borders. In the following step, this lesion spreads radially, exceeds the epidermis and turns into a tumor. Afterwards, the growth becomes vertical, the tumor continues to spread in the dermis and begins to metastasize. In the last step, metastasis develop further from the primary tumor, in distant organs, such as the lung, liver and brain. The figure is adapted from Miller et al. [52].

There are several environmental and inherited risk factors, which increase the probability to develop melanoma during the lifetime [54, 55]. Exposure to the UVR component of the sun radiation spectrum is the main environmental risk factor associated with melanoma. The critical UVR wavelengths, which mostly increase the

risk to develop melanoma are UVA (320-400 nm), and UVB (290-320 nm). Furthermore, intermittent sun exposure, as well as episodes of severe sunburns, are considered to have a more significant contribution to development of melanoma. In addition, exposure to artificial UVR sources, such as indoor tanning, is also harmful. While environmental risk factors affect the entire population, heredity risk factors enhance the hazard in part of the population. These factors mainly include a fair skin hue, light hair color, tendency to develop multiple common and dysplastic nevi and family history of melanoma. Other less common inherited risk factors include passing of rare mutations in specific genes, which may lead to development of familial melanoma. Furthermore, some inherited genetic conditions increase the probability to develop melanoma. These include xeroderma pigmentosum (XP) [56], characterized by a very high sensitivity to sun exposure, and the familial atypical multiple mole melanoma syndrome (FAMMM), which causes development of multiple dysplastic nevi [57].

1.3.2. Clinical diagnosis

Melanoma can appear anywhere on the skin, as well as some mucosal tissues and eyes. The most common sites include the face, scalp, trunk, limbs, and arms. Nevi suspected as melanoma usually have a changing size, shape, and may be itchy. These changes may appear in preexisting or recently appeared nevi. The main warning signs are gathered in the ABCDE rule. The letter “A” stands for Asymmetry, meaning that the shape of one half of the nevus is different than the shape of the other half. The letter “B” stands for Border, which can be uneven, or blurred. The letter “C” stands for Color, indicating that black or brown nevi, as well as nevi with changing colors and spots of colors different from the normal skin color, such as white, grey, red or blue, are suspected as melanoma. The letter “D” stands for Diameter, which is usually larger than the size of a pencil eraser, and/ or had grown in size, in the case of melanoma. The letter “E” stands for Evolving, namely any changes in a pre-existing nevus, whether in the size, shape, color or any other change in its appearance. In addition, any skin abnormalities, as well as appearance of a new nevus, should be carefully examined.

For further diagnosis of a suspected melanoma lesion, it is partially or completely removed and a pathological analysis is performed, including determination of the

following parameters. First, the tumor thickness is determined by evaluation of its Breslow tumor thickness and Clark level. The Breslow tumor thickness serves as an indicator of the depth of invasion of the melanoma. It is measured in millimeters, and classified according to four different ranges: ≤ 1 mm, > 1 mm and ≤ 2 mm, > 2 mm and ≤ 4 mm, or > 4 mm. Clark level indicates the development stage of the melanoma, and has five levels. Level 1: the melanoma is confined to the epidermis. Level 2: the melanoma has invaded the papillary dermis. Level 3: the melanoma exceeds the papillary dermis and is touching the boarder of the dermis. Level 4: the melanoma presents in the reticular dermis. Level 5: the melanoma has invaded the subcutaneous fat. Another evaluated parameter is the presence of ulceration, which refers to loss of the skin surface on the tumor. Furthermore, the mitotic rate is measured, namely the number of cell mitoses per millimeter squared. Additionally, the presence and stage of tumor infiltrating lymphocytes is evaluated. It can be absent, scarce, or dense. At last, presence of melanoma cells in the margins of the removed skin is checked.

In case it is suspected that the melanoma has spread, involvement of the lymphatic system and other organs is investigated. First, a biopsy is taken from the sentinel LN, which is the first LN that drains the cancer from the site of the primary tumor. In case spreading to other parts of the body is suspected, a complementary LN dissection is performed, and the number of removed LNs, as well as the number of infected LNs are evaluated. Infection of other internal organs is usually determined by physical examination and imaging scans, such as computed tomography (CT), positron emission tomography (PET-CT) or magnetic resonance imaging (MRI). Based on the information gained from these diagnostic tests, the stage of the melanoma, between zero and four, is assigned. Stage 0 refers to melanoma in situ, which has a low chance of spreading to other parts of the body. Stage I refers to a thin primary tumor, which persists only in the skin. A stage II melanoma is thicker than stage I, persists in the dermis, and is more likely to spread to other body parts. Stage III describes local spreading of the melanoma on the skin, close to the primary tumor (satellites), or spreading into the regional LN (in-transit metastasis). Stage IV describes spreading of the melanoma to distant body parts, such as soft tissues, distant LNs, lungs, liver, or brain. In addition, the TNM melanoma stage is determined, according to the

melanoma staging system of the American Joint Committee on Cancer (AJCC) [58]. Each staging category, namely T, N, and M, is accompanied by a number. Category T refers to the primary tumor. It has four subcategories (1-4), depending on the size and location of the primary tumor. In case the primary tumor is not identified, stage Tx is assigned. Category N describes the status of local spreading and has four subcategories (0-3), depending on the level of the spreading. Category M describes distant spreading of the melanoma, and has five subcategories (0, 1a, 1b, 1c, and 1d).

Melanoma comprise different types, most of them are cutaneous and some are non-cutaneous [54]. There are four main types of cutaneous melanoma. The most common one is superficial spreading melanoma, which usually develops from a pre-existing nevus, and accounts for 70% of the melanoma cases (Figure 1.5a). According to its name, this type of melanoma usually spreads on the surface of the skin for a while, before it penetrates to deeper layers. The second common type is nodular melanoma, which accounts for 10% - 25% of the cases, and is more common in elderly people. It usually develops rapidly to a bump on the skin, and most frequently on the trunk, legs and arms (Figure 1.5b). Its color is mostly black, but may be red or pink. The third common type is acral lentiginous melanoma, which is diagnosed in 5% of the cases, and more commonly in people with dark skin. It develops on the palms of the hands, soles of the feet, or underneath the nail bed (Figure 1.5c). The fourth type is lentigo maligna melanoma, which is diagnosed in less than 1% of the cases, mostly in elderly people. It is usually associated with high sun exposure, and its most frequent sites are face, ears, arms, and upper trunk (Figure 1.5d). Non-cutaneous melanoma is mainly divided into ocular (uveal) melanoma of the eye (Figure 1.5e), and mucosal melanoma, which begins from mucosal tissues, such as the inner cavity of the mouth (Figure 1.5f).

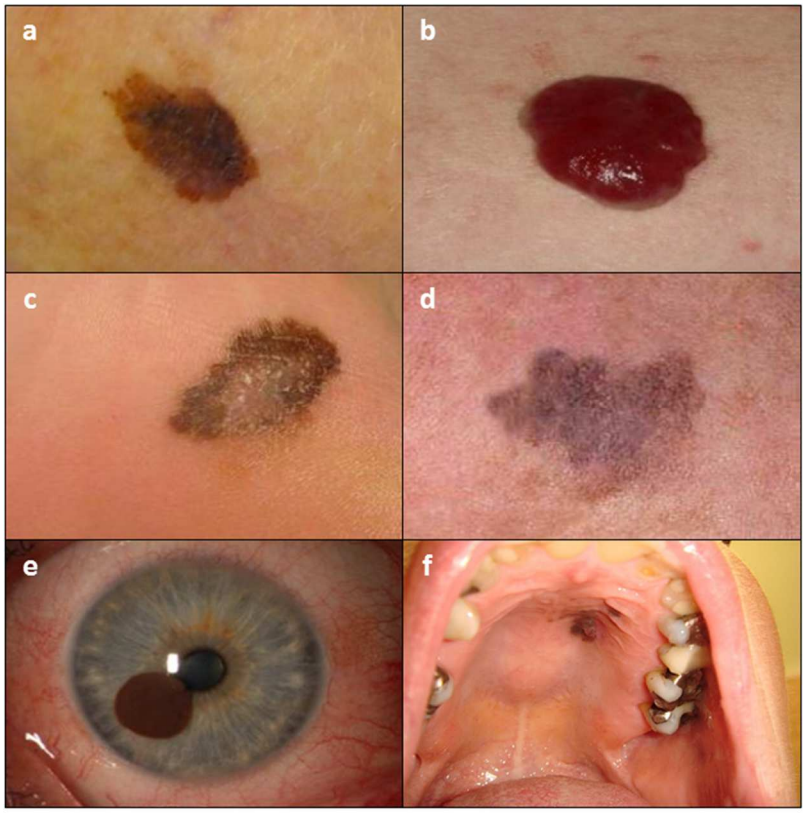

Figure 1.5. Melanoma classifications- specific examples.
There are four main types of cutaneous melanoma. (a) Superficial spreading melanoma, which is the most common type. (b) Nodular melanoma, which is most aggressive type. (c) Acral lentiginous and (d) Lentigo maligna melanoma. Other types of melanoma are non-cutaneous: (e) Ocular melanoma of the eye and (f) mucosal melanoma. Photos are adapted from AlAsadi et al. [59], Kaliki and Shields [60] and Tacastacas [61].

1.4. Immune checkpoint inhibitors for treatment of advanced melanoma

Over the past 10 years, increased biological understanding and access to innovative therapeutic modalities have transformed advanced melanoma into a new oncological model for treating solid cancers [62]. In particular, immune checkpoint inhibitors (ICI) have shown a major success in the treatment of advanced melanoma [37, 39, 63]. The monoclonal antibody ipilimumab, blocking the CTLA-4, was the first checkpoint inhibitor approved for the treatment of advanced melanoma, since it shows an objective response rate of 6-11% [64, 65]. This approval was then followed by the one of pembrolizumab (pembro) and nivolumab. These monoclonal antibodies block the PD-1 receptor, and show response rates of 30-40 % [66, 67]. More recently, a highly

toxic combination of ipilimumab and nivolumab was also approved for the treatment of advanced melanoma, with a resulting response rate of about 60% [68, 69]. But in spite of this relatively high response rate of the combination, PD-1 monotherapy, such as the one with pembro, still remains a pivotal treatment for patients with advanced melanoma, due to its relatively low toxicity and acceptable response rate. Moreover, results of the phase Ib KEYNOTE-001 trial, show that a high proportion of patients with metastatic melanoma achieving a complete response on pembro maintained their complete response for prolonged durations after treatment discontinuation [70]. However, other patients experience disease progression within the first months of treatment. As ICI become widely available, the ability to identify clinical benefit at the baseline stage, may be critical in avoiding either rapid disease acceleration or premature withdrawal of treatment. How to predict individual responses and accordingly adjust treatment plans is a big challenge in the current immunotherapy practice.

The State-of-the-Art approach to solving this problem is the search and identification of reliable response markers [71, 72]. Several biomarkers for response to pembro have been analyzed and the expression of PD-L1 on tumor and immune cells emerged as a potential response marker [73, 74]. Yet, a significant fraction of PD-L1- negative patients, who benefit from pembro [75, 76], suggest that PD-L1 cannot serve as a reliable response biomarker, on its own. In another endeavor, response scales were developed, based on several clinical factors, including localization of metastases, different blood measures, age and sex. These scoring systems enable to stratify the patient cohort according to the overall response rate (ORR), and the probability to survive a year from treatment initiation [72, 77]. In other attempts, certain immune signatures on tumor tissue samples [78, 79], and blood samples [80] were associated with response as well, but the utility of these methodologies has yet to be validated [80].

Even though there exist multiple biomarkers for response prediction under pembro, validation of them for clinical use is still required. Moreover, the outcome information from these biomarkers is rather general for the whole patient population, for example, distinguishing responses of over three months from shorter ones. This information

does not meet the current clinical need of patient-specific outcome prediction. The new approach presented in this thesis forecasts the personal response to immunotherapy, prior to therapy.

1.5. Mathematical models

The complex interplay of cancer cells and the host immune system, as affected by immunotherapy, renders the reasoning of treatment causality difficult. Having the capacity to succinctly integrate this interplay in one coherent framework, and enable its analysis, mathematical models may become instrumental in predicting the interactive dynamics of host immunity, cancer progression and immunotherapy. Thereby, when integrated with clinical data, mathematical models provide a new powerful tool for treatment personalization. Mathematical models have been previously employed for studying the interactions of cancer with the immune system, for investigating the response to different immunotherapies, and for patient-specific regimen personalization [81-89]. For example, Kogan et al. [88] proposed a general algorithm for personalizing cancer immunotherapy, and validated its prediction accuracy and efficiency by clinical trial data on the response to prostate cancer vaccine. The authors constructed and validated personalized mathematical models in the early phases of treatment, by an iterative real-time In-treatment evaluation of patient-specific parameters from the accruing clinical data. Thereafter, they simulated and validated the personal models to predict response to the ongoing therapy, and, in some cases, suggested potentially improved patient-specific treatments. A similar methodology is used in this thesis to predict the response of patients with metastatic melanoma under pembro. The main difference between the approach of Kogan et al [88] and the one presented in this dissertation lies in the model personalization method. In Kogan et al., personalization is achieved by iteratively adjusting model parameters by counts of the prostate specific antigen (PSA) during early treatment. In contrast, the approach in this thesis uses clinical properties measured before treatment onset to adjust the personal model parameters. Another use of a mechanistic model to predict treatment outcomes is made in Elishmereni et al. [90], attacking hormonal treatment of patients with prostate cancer. Elishmereni et al. [90] developed personal mathematical models, describing the dynamic pattern of PSA, as

affected by androgen deprivation therapy (ADT). By simulating the personal models, they predicted the time of biochemical failure, .i.e., onset of resistance to hormonal therapy, in 19 out of 21 (90%) patients with hormone-sensitive prostate cancer. While suited to their specific aims, none of these models included cellular immunity in a way that enables analysis of treatment by ICI. In particular, previous models did not address the recently discovered effects of Effector T cell exhaustion on the treatment. The elucidation of these effects is crucial for evaluating the efficacy of ICI and, therefore, these effects are introduced into the mathematical model developed and analyzed in this thesis.

1.6. The aims of this study

The first aim of this work is to develop a mathematical mechanistic model for the interplay of melanoma cells with the host immune system, as well as the effects of ICIs on this interplay. This is done in order to learn about the relationships between efficacy enhancement of $CD8^+$ T cells, and different tumor dynamics or disease fates, under the influence of ICIs. This contributes to the understanding of potential effects of immunotherapy on the melanoma tumor, before including the actual treatment effects in the mathematical model, which makes it more complicated for analysis.

The second aim of this work is to develop a computational algorithm, whose core is the mechanistic model and its input are different clinical measurements of the patients. Personal mathematical models are generated and simulated to predict the time to progression (TTP) of each patient under pembro. Such predictions are expected to assist the treating oncologists in planning the therapy program of each patient.

2. Methods and data collection

This section describes the mathematical mechanistic model development, the model personalization method, the clinical data collection, and their application for the model calibration and development of the personalization algorithm.

2.1. Mathematical model implementation

The model takes into account the following assumptions:

1. Mutated tumor cells express non-self-antigens and activate APCs. The number of activated functional APCs, denoted A, depends on the tumor immunogenicity [48, 91-93], which is reflected in the activation rate of APCs, α_A [48, 91-93]. The activation of APCs increases with the tumor load, towards saturation. The number of tumor cells required to reach half of the maximal activation rate of APCs is denoted by the coefficient b.
2. Functional APCs die with a rate μ_A.
3. Functional APCs activate effector antigen-specific CD8$^+$ T cells (T) [37, 94, 95], at a rate α_e.
4. Effector CD8$^+$ T cells eliminate tumor cells [37, 96].
5. Effector CD8$^+$ T cells are eliminated at a rate, μ_e. This term accounts for the cell death and exhaustion due to the encounter with tumor cells and regulatory cells. For simplicity, assume that this rate does not depend on the tumor size.
6. The number of tumor cells at any moment, M, is determined by their net growth rate (γ_{mel}) and the rate of elimination by effector CD8$^+$ tumor lymphocytes, denoted ν_{mel}. Their death rate due to the immune system is assumed to reach saturation in M, depending on the coefficient g.
7. Administration of pembro increases the activation rate of CD8$^+$ T cells, and reduces the elimination rate of CD8$^+$ T cells.

Model simplification, incorporating only the bare bones of the system, enables to more easily isolate the effect of each chosen variable and to achieve the stated goal,

while retaining the fidelity of description. A graphical representation of the modelled components and their interactions is given in Figure 2.1.

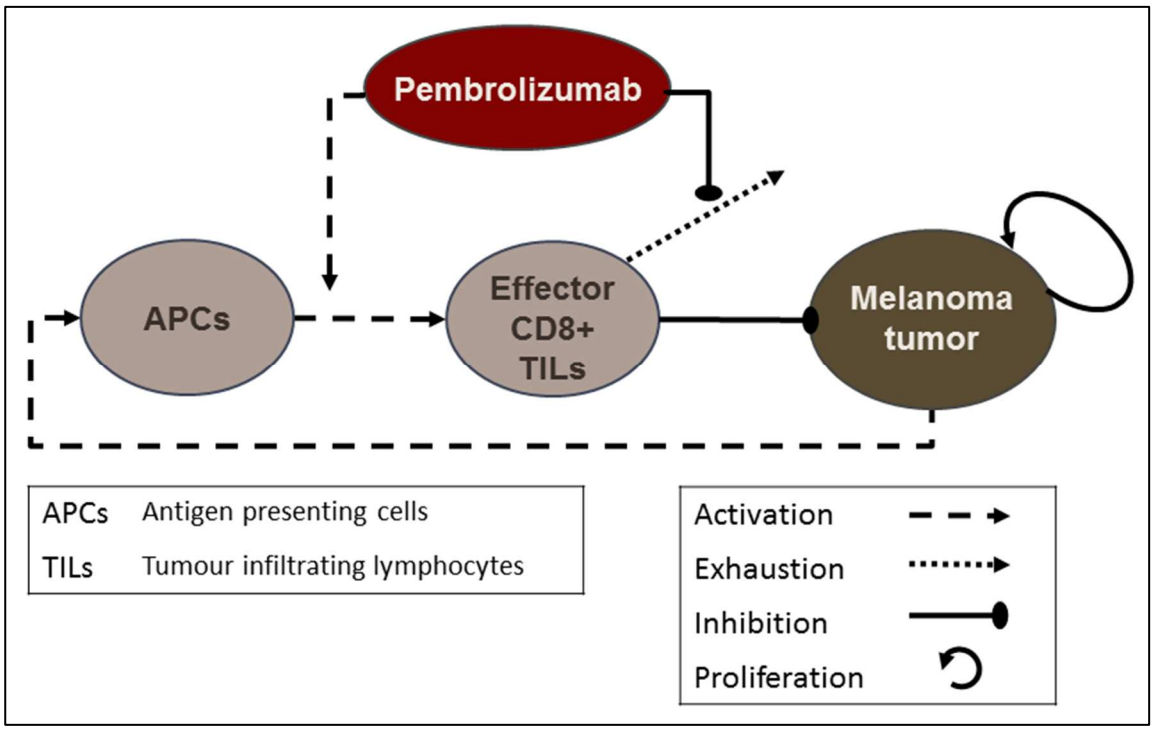

Figure 2.1. A schematic representation of the model.
It describes the main interactions between the melanoma tumor, the cellular immune system, and the immune checkpoint inhibitor pembro. The model is based on the following assumptions: tumor cells stimulate APCs, depending on the tumor immunogenicity; functional APCs activate effector CD8⁺ TILs, which may eliminate tumor cells; effector CD8⁺ TILs become exhausted, independently of the tumor cells elimination; tumor growth is determined by its net growth rate and by the rate of its destruction by Effector CD8⁺ TILs; immunotherapy extends the activation of effector CD8⁺ TILs, and reduces their exhaustion. Annotated ellipses represent the dynamic variables of the model, while arrows represent the interaction between them (see legend).

The model equations for the dynamics of APC (A), CD8⁺ T cells (T) and melanoma cells (M) are given in Equation (1), while the definitions and estimated values of the model parameters are summarized in Table 2.1.

a) $$\frac{dA}{dt} = \alpha_A \cdot \frac{M}{M+b} - \mu_A \cdot A,$$ Eq. (1)

b) $$\frac{dT}{dt} = a_{pem} \cdot \alpha_e \cdot A - b_{pem} \cdot \mu_e \cdot T,$$

c) $$\frac{dM}{dt} = \gamma_{mel} \cdot M - \upsilon_{mel} \cdot \frac{T \cdot M}{M+g}.$$

The effect of pembro on the immune system and the tumor was represented by the parameters a_{pem}, and b_{pem}. From the initial time of the simulation (t=0) to the time of treatment initiation (t = t_1), the treatment-free model ($a_{pem} = b_{pem} = 1$) was simulated, and from t_1 until the end of the simulation period, the complete model in Equation (1) was simulated.

2.2. Parameter definition and estimation

In order to perform simulations in realistic parameter ranges, the latter were either directly referenced or estimated from published experimental and clinical data, as summarized in Table 2.1.

Table 2.1. Estimated parameter values.

Parameter name	Definition	Estimated value	Units	Source
α_A	Activation rate of APCs	$1.161 \cdot 10^3$ to $2.986 \cdot 10^3$	cells/d	[97, 98]
b	Number of tumor cells, required for reaching half of the maximal APC activation rate	$3.704 \cdot 10^4$ to $1.476 \cdot 10^5$	cells	[97-99]
μ_A	Death rate of APCs	0.2310	d^{-1}	[100, 101]
a_{pem}	Maximum effect of pembro on activation of $CD8^+$ T cells	$1 \cdot 10$ to $1 \cdot 10^4$	-	Model simulations
α_e	Activation rate of naïve antigen-specific $CD8^+$ T cells	0.8318	d^{-1}	[102]
b_{pem}	Maximum effect of pembro on the exhaustion rate of $CD8^+$ T cells	0.9	-	Model simulations
μ_e	Death rate of Effector $CD8^+$ T cells	0.1777	d^{-1}	[103]

γ_{mel}	Net growth rate of tumor cells	0.003269 to 0.08664	d^{-1}	[104, 105]
υ_{mel}	Innate death rate of tumor cells by effector $CD8^+$ T cells	0.1245	d^{-1}	[106-108]
g	Number of tumor cells, at which the elimination rate reaches half of its maximal value	$2.019 \cdot 10^7$ to $1 \cdot 10^8$	cells	[89, 108, 109]

In-depth parameter estimation methods

The following paragraphs describe the parameter estimation methods in more detail.

α_A , b**: Activation of Antigen presenting cells by tumor cells**

These two parameters are related to activation of APCs by tumor cells. For their estimation DCs were considered solely, since they constitute the majority of APCs and play the main role in $CD8^+$ T cells activation. Activation rate of functional DCs depends on the immunogenicity of the tumor, in terms of antigen availability, as well as DCs maturation, determined here by migration rate of DCs into the LNs. The level of antigen, which varies among patients, is proportional to the number of antigen-expressing melanoma cells.

Both α_A and b were estimated from co-culture experiments of DCs with irradiated melanoma cells [97, 98]. The relation of these parameters to DCs activation is derived from Equation (1a):

$$\frac{dA}{dt} \approx \frac{\%phago \cdot \%migration \cdot A_0}{\Delta t} \approx \alpha_A \cdot \frac{M_0}{M_o + b}. \qquad \text{Eq. (2)}$$

The variables A_0 and M_0 denote the number of co-cultured APCs and melanoma cells, respectively. The variable M_0 was held constant for simplicity. The variable $\%phago$ denotes the calculated rate of melanoma cells phagocytosis by APCs, $\%migration$ is migration rate of APCs from the skin to LNs, which is assumed as an indicator of APCs

maturation, and estimated around 2% [110, 111]. Lastly, Δt is the duration of the co-culture experiment.

The co-culture results of human melanoma cell lines with APCs from healthy donors are summarized in Table 2.2.

Table 2.2. Experimental results of human APCs and melanoma cells co-culture. The parameters are defined under Equation (2).

$A_0 : M_0$ ratio	$A_0\ [cells]$	$M_0\ [cells]$	$\%phago$	$\Delta t\ [d]$	Source
3:1	$1{\cdot}10^5$ (a)	$3.33{\cdot}10^4$	55	2	[98]
3:1	$1.05{\cdot}10^6$ (b)	$3.5{\cdot}10^5$ (c)	10 – 20	2	[97]

(a) *Estimated number of cells.*
(b) *The experiment was performed in wells, containing $3{\cdot}10^5$/ml DCs. The volume of each well was 3.5 ml.*
(c) *Mostly MART-1+ melanoma cells.*

Substitution of the data in Table 2.2 into Equation (2) yields

$$\alpha_A = 1.161 \cdot 10^3 \text{ to } 2.986 \cdot 10^3 \ \left[\frac{cells}{d}\right], \qquad \text{Eq. (3)}$$
$$b = 3.704 \cdot 10^4 \text{ to } 1.476 \cdot 10^5 \ [cells].$$

For analysis of the treatment-free model, the center value of b was used, namely $9.233{\cdot}10^4$ cells.

μ_A: Death rate of APCs

The death rate of DCs was estimated from the half-life time of splenic murine DCs, which is three days [112]. Accordingly, $\mu_A = \frac{\ln(2)}{3} = 0.2310\ [d^{-1}]$.

α_e: Activation rate of antigen-specific CD8⁺ T cells

According to [102], the half-life of binding between a T cell and its conjugant epitope on an APC is 20 hours. This corresponds to an activation rate $\alpha_e = \frac{\ln(2)}{\frac{20}{24}} = 0.8318\ [d^{-1}]$.

μ_e: Exhaustion rate of Effector CD8⁺ T cells

The exhaustion rate of effector CD8⁺ T cells was calculated from their half life time, τ: $\mu_e = \frac{ln(2)}{\tau}$.

Estimation of the half-life time is based on experimental examination of different immunogens as triggers for the T cell activation. The influence of the immunogen nature on T cells life span was assumed to be negligible. Taylor et al. [103] estimated a half-life time of 3.9 days for effector T cells in peripheral blood of patients with human T-cell leukemia virus type 1 (HTLV-1). This corresponds to an exhaustion rate of $\mu_e = 0.1777\ [d^{-1}]$.

γ_{mel}: Net growth rate of tumor cells

In the model, an exponential cancer growth is assumed (Equation (1c)). The parameter γ_{mel} is calculated from the doubling time of melanoma metastasis: $\gamma_{mel} = \frac{\ln(2)}{\Delta t}$, where Δt is the doubling time. Carlson [104] estimated the tumor doubling time from clinical data of three patients as $\Delta t = 8 - 212\ [d]$. The corresponding growth rate is $0.003269 < \gamma_{mel} < 0.086643\ [d^{-1}]$. This is a few orders of magnitude smaller than the tumor growth rate calculated from *ex vivo* murine models. In addition, an average doubling time of 32 days had been measured in three patients with pulmonary melanoma metastasis [105]. The resulting tumor growth rate is $\gamma_{mel} < 0.02166\ [d^{-1}]$. For the model analysis the average tumor growth rate of $0.04496\ [d^{-1}]$ was taken.

g: Michaelis-Menten constant of effector-tumor cells interaction

The value $g = 2.019 \cdot 10^7\ cells$ was adapted from [106-108], based on BCL-1 lymphoma cells transplanted in spleens of chimeric mice, and [109] who estimated a value of $g = 10^8\ cells$. For the treatment-free model analysis, the average value of $g = 6.01 \cdot 10^7\ cells$ was considered.

2.3. Software in use

Numerical analyses and simulations were performed using the ode15s Runge-Kutta ODE solver of Matlab R2016a (The Mathsworks, UK).

2.4. Patient data collection

The study population included 54 patients with advanced melanoma, who were treated in the past or still receive pembro as a single-agent between 09/01/2013 and 03/03/2017, at Hadassah Medical Center (HMC, 33 patients), and the University Medical Centre Mannheim (UMM, 21 patients). Recruitment to the retrospective clinical trial was subjected to compliance with the following criteria.

2.4.1. Inclusion criteria formulation

1. Gender: Female, Male.
2. Age: Eighteen years and older at the start of treatment.
3. Histologically confirmed unresectable Stage III or Stage IV melanoma, as per AJCC staging system.
4. Prior radiotherapy or other oncological treatments must have been completed at least two weeks prior to drug administration.
5. Measurable disease by CT or PET-CT or MRI per Response Evaluation Criteria In Solid Tumors 1.1 (RECIST 1.1) [113].
6. The patient has at least one quantitative measurement of at least one target lesion (primary tumor or metastasis) before treatment.
7. The patient has at least one quantitative measurement of at least one target lesion (primary tumor or metastasis) during or after the treatment.
8. The patient has at least one recorded visit to the treating oncologist before treatment.
9. The patient has at least one recorded visit to the treating oncologist during or after the treatment.
10. Treatment as per Standard of care (SOC) for melanoma.

2.4.2. Exclusion criteria formulation

1. History of another malignancy within the previous two years, except for adequately treated Stage I or II cancer currently in complete remission, or any other cancer that has been in complete remission for at least two years.
2. Ocular melanoma

The data collected from the medical records included the following: demographics, information about the diagnosis and the primary tumor, staging, given oncological treatments, detailed information about administration of pembro (specific protocols), imaging data, and blood measures, including relative counts of blood lymphocytes (LY%). Baseline information and patients' follow-up period are summarized in Table 2.3.

Table 2.3. Characteristics of the patient cohort, and baseline information.

Age mean (range), years	68.5 (32.5 – 91.5)
Sex	
Male n (%)	39 (72%)
Female n (%)	15 (28%)
Primary nodular melanoma	
Yes n (%)	11 (20%)
No n (%)	41 (76%)
Undetermined n (%)	2 (4%)
Breslow tumor thickness average (range), mm	4.11 (0.37 – 28)
BRAF V600 status	
Wild type n (%)	33 (61%)
Mutant n (%)	13 (24%)
Undetermined n (%)	8 (15%)
Previous ipilimumab n (%)	22 (41%)
Previous nivolumab n (%)	0 (0%)
Baseline tumor size before pembro average (range), mm	79 (5 – 247)
Follow-up period median (range), months	9 (2 – 35)

2.5. Imaging data assessment

Baseline and follow-up CT and MRI scans were retrospectively reviewed by radiologists at HMC and UMM. The time interval between consecutive scans was around three months. In each scan the maximal and perpendicular diameters of each morphologic detectable lesion in the x-y plane were evaluated, using the GE Centricity

PACS software of GE Healthcare at HMC, and a dedicated post processing software (Syngo.Via, Siemens Healthineers, Erlangen, Germany) at UMM. The organ of each lesion was documented, as well as appearance of new lesions in follow-up scans.

2.6. Response evaluation

Response evaluation and identification of target lesions was made based on the RECIST 1.1 guidelines. According to Eisenhauer et al. [113], a target lesion is defined by its size, having a minimum diameter of 10 mm for a non-nodal lesion, or a minimum diameter of 15 mm in case of LNs. In accordance with RECIST 1.1, up to two target lesions per organ and a maximum of five in total were selected. The target lesions diameters were summed up to obtain the sum of diameters (SOD) at each tumor size assessment for every patient. At each time of clinical tumor size evaluation, one of the RECIST 1.1-defined response types were assigned, as specified in [113].

2.7. Development of the personalization algorithm

2.7.1. Selection of the personalized model parameters

In order to personalize the model, the parameters which are expected to significantly affect the response and to vary among patients were first selected. The following two parameters were personalized, namely, their values were adjusted within a certain range: (i) effect of pembro on the activation of $CD8^+$ T cells (a_{pem}) and (ii) tumor growth rate (γ_{mel}). The choice to personalize these two parameters was based on the theoretical analysis of the above described mathematical model in [Tsur et al., peer-reviewed], showing that changes in the maximum effect of pembro on the activation of $CD8^+$ T cells, a_{pem}, affect the balance between tumor growth rate and the efficacy of the immune system. This parameter was inferred to vary among patients. Furthermore, stability analysis of the mathematical model shows that in an untreated host, the net growth rate of tumor cells, γ_{mel}, is the most significant contributor to tumor dynamics [Tsur et al., peer-reviewed], therefore it is considered as an individual parameter as well.

For personalizing the mathematical model, the range of a_{pem} was set to obtain different tumor dynamics, as a result of the therapy. The range of γ_{mel} was estimated

from the doubling time (Δt) of human melanoma metastases, $\gamma_{mel} = \frac{\ln(2)}{\Delta t}$, which was estimated by [104] and [105], as described in detail in Table 2.1. In order to improve parameter identifiability, the parameter γ_{mel} was dichotomized to be equal to either the minimum or the median of its range. The ranges of the personal parameters are summarized in Table 2.4. For the first iteration of the fitting algorithm, the initial guess of each decision parameter was chosen as the median of its range. As mentioned above, all other parameters were fixed to their values reported in Table 2.1.

Table 2.4. Ranges of the decision parameters for identifying the patient's personal model parameters.

Model parameter	Definition	Personal parameter range	Units
a_{pem}	Maximum effect of pembro on activation of $CD8^+$ T cells	10 to 10^4	-
γ_{mel}	Tumor growth rate	$3.269 \cdot 10^{-3}$ or $5 \cdot 10^{-3}$	d^{-1}

2.7.2. Creating the personalized models

To fit the model to data from the training set, the sum of squared errors (SSE) of the observed and the simulated tumor size was minimized, using the '*fmincon'* function in Matlab. The goodness of fit was determined by calculating the coefficient of determination, R-squared, for the fitted versus clinically measured tumor sizes of all the patients in the dataset. Subsequently, the functions that enable personalization of the mathematical model were determined, by considering several clinically measured factors, whose values were available for the majority of the patients in this study, in at least one time point before treatment onset, or at least in one time point at an early stage of the treatment (Table 2.5). Some of these factors, including lactate dehydrogenase (LDH) levels, LY%, and baseline SOD, are known to be related to the response to pembro [72, 114]. The relationships between the other clinical variables considered for the personalization functions, and outcome under pembro, were examined by correlation analysis. Three standard statistical methods were used to

analyze the relationships between personal clinical data and model parameters: the Pearson coefficient, the receiver operating characteristic (ROC) analysis, confusion table and Cohen's kappa (κ). The obtained relationships were the basis for the formulation of the personalization functions.

Table 2.5. Availability of measurements in the recruited patient dataset.
The measured parameters are potential covariates for determination of the personal models.

Potential Covariate	Availability (number of patients, out of 54)
Age	54
Breslow tumor thickness	43
LDH (lactate dehydrogenase)	51
LY% (relative lymphocyte count in the blood)	53
SOD at the baseline (*)	54
Cutaneous malignant melanoma (Y/N)	52
Nodular melanoma (Y/N)	52
BRAF V600 mutation (Y/N)	46

Y/N refers to a test outcome. (*) Sum of Diameters of measurable lesions at the baseline, as defined by RECIST 1.1 [113].

To normalize variations in the clinical and molecular values, due to differences in the measurement and calibration techniques used in each medical center, each measured value (X) was normalized relative to its given range, between X_{min} and X_{max}, as specified. This was performed for each of the two subsets. The normalized covariate value ($\hat{X}$) is denoted

$$\hat{X} = \frac{X - X_{min}}{X_{max} - X_{min}}. \qquad \text{Eq. (4)}$$

From the individual model fits the personal model parameters were obtained for all patients in the training set. The relevant clinical measurements for all patients were

retrieved from the clinical record files of each patient, at baseline, and around the time of the first follow-up imaging assessment. For estimation of a_{pem} from the clinical/molecular measurements, the k-Nearest Neighbors (k-NN) algorithm was used. The number of nearest neighbors, k, was taken to be the integer part of the square root of the total number of patients (N=54), i.e., k=7. In case of missing data of a clinical/molecular measurements, the missing value was replaced by the average value for this clinical factor, obtained from the data of the rest of the patients. Missing values of binary clinical/molecular factors were set to 0. The resulting personalization functions were validated by the Leave-One-Out cross validation (LOO CV) method. In order to evaluate the personal γ_{mel} values from the clinical measurements, a classification tree was trained, using the LOO CV, as above. After predicting the parameter values of each patient, the personalized models were simulated (using the ode15s solver of Matlab), the simulated tumor size at the days of the imaging assessments was derived, and the TTP was evaluated based on RECIST 1.1 [113].

2.8. Analysis of the time to progression results

To evaluate the quality of the TTP prediction, the predicted versus the clinically observed TTP was compared in three time intervals, including 0 – 90 days, 91 – 150 days, and 151 – 365 days, from pembro initiation. The number of patients, for whom no disease progression was indicated during their follow-up period, was also taken into account.

Predictions were categorized according to these time intervals, and generated a confusion table. The data in the confusion table was categorized according to six different outcomes:

1. Progressive disease (PD) was clinically evidenced by imaging assessments, as well as predicted by the algorithm, at the same time interval ($t_r = t_s$), where t_r and t_s denote the reference and simulated time intervals of the TTP, respectively.
2. The algorithm's simulated TTP was predicted to precede the observed TTP ($t_s < t_r$)

3. The algorithm's simulated TTP was predicted to occur later than the observed TTP ($t_s > t_r$)
4. Disease progression was not clinically observed, but was predicted by the algorithm ($r = 4; s = 1,2,3$)
5. Disease progression was clinically observed, but was not predicted by the algorithm ($r = 1,2,3; s = 4$)
6. Disease progression was neither observed nor predicted by the algorithm, during the follow-up period ($r = s = 4$)

To calculate the corresponding value of Cohen's kappa (κ), the multidimensional formula of Warrens [115] was applied, which defines the ratio p_1, between the number of patients with outcomes 1 and 6 (see above), denoted $N_{TTP}(t_s = t_r)$, and the total number of patients in the cohort ($N = 54$)

$$p_1 \equiv \sum_{r,s=1}^{4} \frac{N_{TTP}(t_r = t_s)}{N}. \qquad \text{Eq. (5)}$$

The proportion of patients in each time interval is denoted p_2. It is calculated from the number of simulated, and observed disease progression incidences in each time interval, denoted $N_{TTP}(t_s)$, and $N_{TTP}(t_r)$, respectively

$$p_2 \equiv \sum_{\mathrm{r,s=1}}^{4} \frac{N_{TTP}(t_s)}{N} \cdot \frac{N_{TTP}(t_r)}{N}. \qquad \text{Eq. (6)}$$

The multidimensional Cohen's kappa (κ) is

$$\kappa = \frac{p_1 - p_2}{1 - p_2}. \qquad \text{Eq. (7)}$$

3. Results

This section is divided into three parts. The first part (3.1) describes the analysis of the mathematical model for interaction between the melanoma tumor and the host immune system. To render the model tractable to analysis, the effect of ICI treatment was simplified and took the form of changes in the activation rate of $CD8^+$ T cells, and the net growth rate of the tumor. The second part (3.2) describes the personalization algorithm and its development, taking into consideration the results of the first part. The third part (3.3) shows the prediction results of the personal TTP of the patients, obtained by using the personalization algorithm. The results of the treatment-free model analysis were submitted for publication to the Journal of Theoretical Biology (**Tsur et al. Response of Patients with Melanoma to Immune Checkpoint Blockade – Insights Gleaned from Analysis of a New Mathematical Mechanistic Model**, *Journal of theoretical biology* 2019, revised version submitted). The results of the algorithm development and TTP prediction were submitted for publication to the Journal of Translational Medicine (**Tsur et al. Predicting Response to Pembrolizumab in Metastatic Melanoma by a New Personalization Algorithm,** *Journal of Translational Medicine* 2019, revised version submitted).

3.1. Response of Patients with Melanoma to Immune Checkpoint Blockade – Insights Gleaned from Analysis of a New Mathematical Mechanistic Model

Summary: immune checkpoint inhibitors (ICI) are becoming widely used for treatment of metastatic melanoma. However, prediction of the individual benefit of patients from these therapeutics remains an unmet clinical need. Mathematical models that predict response of patients with melanoma to ICI can contribute to better informed clinical decisions. This chapter describes the development of a simple ODE-based mathematical population model for pembro-treated patients with advanced melanoma, and analysis of the local and global dynamics of the system. The results show that zero, one, or two steady states of the mathematical system exist in the

phase plane, depending on the parameter values of individual patients. Without treatment, the simulated tumors grew uncontrollably. At increased efficacy of the immune system, i.e. due to immunotherapy, two steady states were found, one leading to uncontrollable tumor growth, whereas the other resulted in tumor size stabilization. The model analysis indicates that a sufficient increase in the activation of $CD8^+$ T cells results in stable disease, whereas a significant reduction in T-cell exhaustion, another process contributing to $CD8^+$ T cell activity, entails a temporal reduction in the tumor mass, but fails to control disease progression in the long run. Importantly, the initial tumor burden influences the in-treatment dynamics: small tumors responded better to treatment than larger tumors. In conclusion, the model suggests that disease progression and response to ICI depend on the ratio between activation and exhaustion rates of $CD8^+$ T cells. The model analysis provides a foundation for the use of computational methods to personalize immunotherapy.

3.1.1. Defining a biologically relevant domain for model analysis

Asymptotic solutions for the treatment-free model, defined in Equation (1) (see methods section 2.1), under substitution of $a_{pem} = b_{pem} = 1$, are of interest, since they indicate the potential fates of the system. For example, a positive, steadily growing number of cancer cells over time suggests inability to cure the disease. Additional potential solutions include, for instance, a decrease in the number of tumor cells down to a constant amount, indicating shrinkage and tumor stabilization thereafter. Further solutions may present oscillations that might indicate alternating periods of tumor shrinkage and growth.

Assuming $A(t_0) \geq 0$, $T(t_0) \geq 0$, $M(t_0) \geq 0$, solutions for Equation (1) exist for any $t > t_0$, and the domain defined by

$$0 \leq A \leq \frac{\alpha_A}{\mu_A},$$
$$0 \leq T \leq \frac{\alpha_e \cdot \alpha_A}{\mu_e \cdot \mu_A},$$
$$0 \leq M.$$

Eq. (8)

is invariant (i.e., if a trajectory has initial values inside this domain, it will remain there). To see this, note that from Equation (1) one can deduce the following two differential inequalities $-\mu_A \cdot A \leq \frac{dA}{dt} \leq \alpha_A - \mu_A \cdot A$ and $-\mu_e \cdot T \leq \frac{dT}{dt} \leq \alpha_e \cdot A - \mu_e \cdot T$.

From the former, by the comparison theorem for ODEs it follows that $A(t)$ is bounded from above and below by the trajectories of the equations $\dot{x} = -\mu_A \cdot x$ and $\dot{x} = \alpha_A - \mu_A \cdot x$, with the same initial value, correspondingly. Hence, if $A(t_0) \in [0, \frac{\alpha_A}{\mu_A}]$, then for each $t > t_0$, $A(t) \in [0, \frac{\alpha_A}{\mu_A}]$. Similar reasoning, taking into account the bounds obtained for $A(t)$ gives the bounds for $T(t)$. Finally, $\dot{M} \geq (\gamma_{mel} - \nu_{mel} \cdot T) \cdot M$, from which it follows by comparison that if $M(t_0) \geq 0$, then $M(t) \geq 0$ for any $t \geq t_0$.

In the following, the analysis was limited to the biologically relevant domain, defined in Equation (8), additionally assuming that all the system parameters are positive.

Multiple steady states and their stability analysis

Theoretical and numerical analysis of the model enables to determine the number of steady states in the system, and the conditions for their stability, as well as to identify the critical bifurcation points. The steady states and the critical bifurcation points can pinpoint parameter ranges for which treatment with ICIs can turn persistent tumor growth in an untreated host into conditions under which the immune system can control the disease. Therefore, the fixed points (FPs) in Equation (1) were determined by nullifying the derivatives and solving the resulting algebraic system, obtaining one trivial solution, for $M = 0$ and two non-trivial solutions, for $M > 0$:

a) $A = \frac{\alpha_A}{\mu_A} \cdot \frac{M}{M + b}$, Eq. (9)

b) $T = \frac{\alpha_e}{\mu_e} \cdot A$,

c) $M \cdot [\gamma_{mel} \cdot (M + g) - \nu_{mel} \cdot T] = 0$.

Immune cells are not activated in a tumor-free state

In order to analyze the tumor dynamics around the trivial steady state, the stability of the associated steady state solution of Equation (1) was determined. Substituting $M = 0$ in Equation (9) reflects the case of a tumor-free host. This yields the FP

$(A^*, T^*, M^*) = (0,0,0)$, which indicates correctly that for this condition tumor-specific immune cells are not activated.

The Jacobi matrix of this FP is:

$$\begin{pmatrix} -\mu_A & 0 & \frac{\alpha_A}{b} \\ \alpha_e & -\mu_e & 0 \\ 0 & 0 & \gamma_{mel} \end{pmatrix}$$

The characteristic polynomial of this matrix is:

$$\mathrm{P}(\lambda) = (\mu_A + \lambda) \cdot (\mu_e + \lambda) \cdot (-\gamma_{mel} + \lambda). \quad \text{Eq. (10)}$$

The eigenvalues of the Jacobi matrix are $(-\mu_A, -\mu_e, \gamma_{mel})$. Since not all real parts of the matrix are negative, the FP $(A^*, T^*, M^*) = (0,0,0)$ is unstable. From this it is concluded that if a tumor exists at time zero in the model, namely $M(0) > 0$, it will not disappear, and, plausibly, the number of tumor cells will diverge from zero.

3.1.2. Steady states in a tumor-positive scenario can indicate disease progression or treatment efficacy

Next, the conditions, under which steady states of the system can be identified in the presence of tumor, were studied. A steady state solution can be obtained by solving Equation (9) for $M \neq 0$. Substitution of the expression for T in the expression for M in Equation (9) yields

$$M = \frac{\nu_{mel}}{\gamma_{mel}} \cdot \frac{\alpha_e}{\mu_e} \cdot \frac{\alpha_A}{\mu_A} \cdot \frac{M}{M+b} - g. \quad \text{Eq. (11)}$$

By defining $\overline{K} \equiv \frac{\nu_{mel} \cdot \alpha_e \cdot \alpha_A}{\gamma_{mel} \cdot \mu_e \cdot \mu_A}$ for convenience, Equation (11) becomes

$$M^2 + (b + g - \overline{K}) \cdot M + b \cdot g = 0. \quad \text{Eq. (12)}$$

The parameter $\overline{K}$ represents the ratio between the efficacy of the immune response and the tumor growth capacity. Solving Equation (12) yields M at steady state, M^*:

$$M^* = \frac{\overline{K} - (b + g) \pm \sqrt{(b + g - \overline{K})^2 - 4b \cdot g}}{2} \equiv M^{\pm}. \quad \text{Eq. (13)}$$

The two roots $M^{\pm}$ represent two different FP values for the number of cancer cells. The numbers of immune cells in steady state are obtained from substitution of Equation (13) in Equation (9):

a) $A^* = \frac{\alpha_A}{\mu_A} \cdot \frac{M^{\pm}}{M^{\pm}+b} \equiv A^{\pm}$, Eq. (14)

b) $T^* = \frac{\alpha_e}{\mu_e} \cdot A^{\pm}$.

Depending on the value of $\overline{K}$, Equation (12) can have zero, one or two real positive solutions. A necessary condition on $\overline{K}$, for Equation (12) to have real positive roots is given by

$$\overline{K} > (b + g). \quad \text{Eq. (15)}$$

By nullifying the discriminant of M^* in Equation (13), one obtains the condition on $\overline{K}$ for a single root, that is, a single FP:

$$\overline{K}_{1,2} = b + g \pm 2\sqrt{b \cdot g} = \left(\sqrt{b} \pm \sqrt{g}\right)^2. \quad \text{Eq. (16)}$$

$\overline{K}_{1,2}$ are the values of $\overline{K}$, which correspond to a single FP.

The system in Equation (1) has one real positive FP (PFP), when conditions (15) and (16) are satisfied i.e., when

$$\overline{K} = \left(\sqrt{b} + \sqrt{g}\right)^2. \quad \text{Eq. (17)}$$

The discriminant in Equation (13) is positive when $\overline{K} < \left(\sqrt{b} - \sqrt{g}\right)^2$, or $\overline{K} > \left(\sqrt{b} + \sqrt{g}\right)^2$. Together with the positivity condition in Equation (15), Equation (12) has two real positive roots, that is, two PFPs, when:

$$\overline{K} > \left(\sqrt{b} + \sqrt{g}\right)^2. \quad \text{Eq. (18)}$$

From this it can be concluded that different values of $\overline{K}$ impose different stability patterns on the system, including a possible saddle-node bifurcation, when two FPs collide and disappear. To visualize this, Equation (12) was rewritten in the form

$$(M + b) \cdot (M + g) = \overline{K} \cdot M. \quad \text{Eq. (19)}$$

The left-hand side (l.h.s) of Equation (19) is a parabola and its right-hand side (r.h.s) is a straight line. In Figure 3.1, both sides of Equation (19) are plotted against each other for different parameter values. Intersections of the lines mark the FPs, and their number depends on the values of $\overline{K}$, b and g. For $\overline{K} > \left(\sqrt{b} + \sqrt{g}\right)^2$, the lines intersect twice on $M > 0$, resulting in two PFPs (dashed line). As $\overline{K}$ decreases, the intersections

approach each other, until they collide when $\overline{K} = \left(\sqrt{b} + \sqrt{g}\right)^2$ (grey solid line). The corresponding system has a single FP. For $\overline{K} < \left(\sqrt{b} + \sqrt{g}\right)^2$, the lines in Equation (19) do not intersect on $M > 0$ and therefore Equation (12) has no positive solutions (dashed-dotted line).

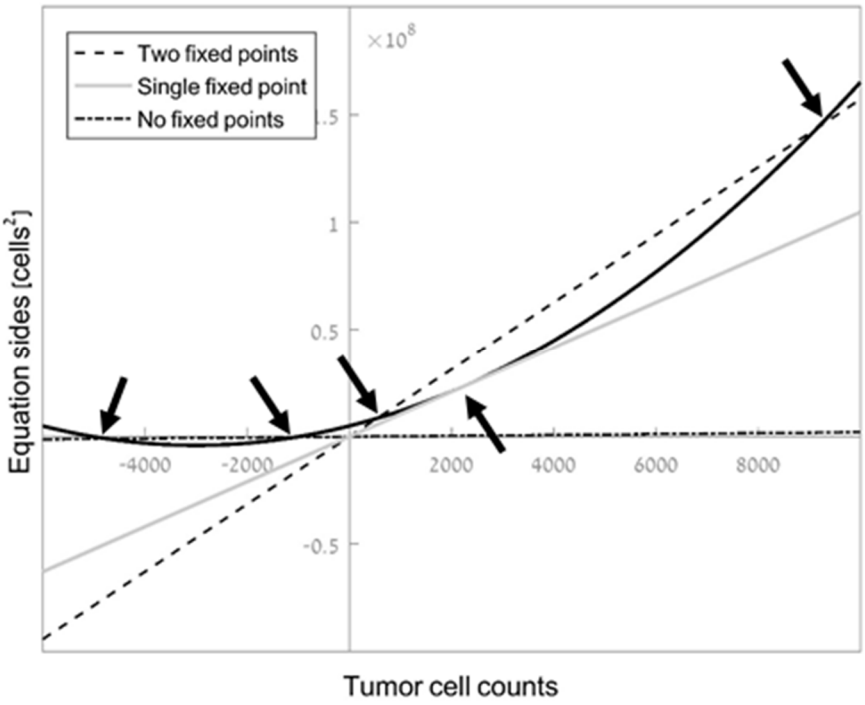

Figure 3.1. Existence and number of PFPs.
This number depends on the value of $\overline{K}$. This figure is a graphical analysis of Equation (19). The black solid curve represents the left-hand side (l.h.s) of the equation, the others represent the right-hand side (r.h.s) of Equation (19) for different values of $\overline{K}$. The arrows mark the intersections between the r.h.s and l.h.s of Equation (19). The grey solid line demonstrates the case of a single tangential intersection of the equation sides (for $\overline{K} = \left(\sqrt{b} + \sqrt{g}\right)^2$). This corresponds to a single solution, i.e., one PFP. If the r.h.s line has a steeper slope than the grey solid line, two intersections are obtained (dashed line), and the system has two PFPs. In case the r.h.s line has a lower slope than the grey line (dashed-dotted line), the system has no PFPs.

The value of $\overline{K}$ for which the system has a single FP (see Equation (17)), is $\overline{K} \approx 6.5 \cdot 10^7$cells (Table 2.1). As demonstrated in Figure 3.2, for smaller $\overline{K}$, no PFPs exist, and as will be shown later, the corresponding tumors grow uncontrollably. For larger values of $\overline{K}$, the system has two PFPs, biologically corresponding to tumor shrinkage or disease stabilization, due to immune control, *i.e.*, by ICI treatments.

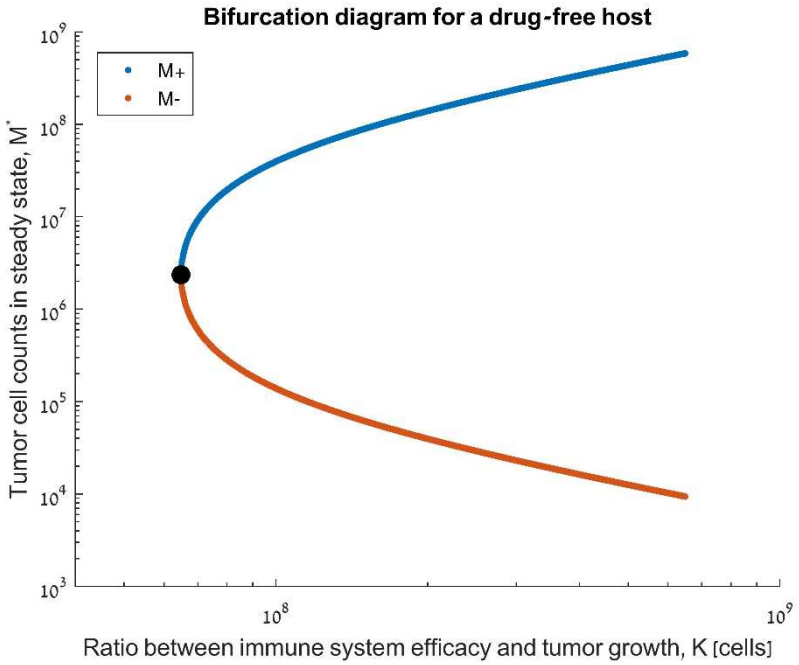

Figure 3.2. Bifurcation diagram displaying positive steady states of Equation (1). The number of melanoma cells in steady state ($\boldsymbol{M^*}$) is plotted versus the parameter $\boldsymbol{\overline{K} \equiv \frac{\nu_{mel} \cdot \alpha_e \cdot \alpha_A}{\gamma_{mel} \cdot \mu_e \cdot \mu_A}}$. As shown in Figure 3.1, the number of FPs depends on the value of $\boldsymbol{\overline{K}}$. Under the estimated parameter values in Table 2.1 and according to Equation (17), the system has a single PFP when $\boldsymbol{\overline{K} \approx 6.5 \cdot 10^7 cells}$, with $\boldsymbol{M^* = 2.35 \cdot 10^6\ cells}$ (marked by a black circle). When the value of $\boldsymbol{\overline{K}}$ is below this threshold, the system has no PFPs, resulting in an uncontrollable tumor growth. Otherwise, when the value of $\boldsymbol{\overline{K}}$ is above the threshold, the system has two PFPs, denoted by $\boldsymbol{M^+}$ and $\boldsymbol{M^-}$ (Equation (13)).

Tumor PFPs can be locally stable under increased activation or reduced exhaustion rates of CD8+ T cells, and when the tumor growth rate is low.

To learn about the stability properties of the PFPs of Equation (1), their local stability was first studied. This included calculation of the eigenvalues, λ, of the Jacobi matrix of the system, $\hat{J}$, as shown below:

$$\begin{pmatrix} -\mu_A & 0 & \frac{\alpha_A \cdot b}{(M^* + b)^2} \\ \alpha_e & -\mu_e & 0 \\ 0 & -\frac{\nu_{mel} \cdot M^*}{M^* + g} & \gamma_{mel} - \frac{\nu_{mel} \cdot T^* \cdot g}{(M^* + g)^2} \end{pmatrix}$$

Note that this matrix depends on the steady state values: (A^*, T^*, M^*).

The determinant of $\hat{J} - \lambda \hat{I}$ is a 3rd order characteristic polynomial:

$$\mathrm{P}(\lambda) = (\mu_A + \lambda) \cdot (\mu_e + \lambda) \cdot \left[\frac{\nu_{mel} \cdot g \cdot T^*}{(M^* + g)^2} - \gamma_{mel} + \lambda\right] + \alpha_A \cdot \alpha_e \cdot \nu_{mel} \cdot \frac{b}{(M^* + b)^2} \cdot \frac{M^*}{M^* + g}. \quad \text{Eq. (20)}$$

By defining $\overline{\Delta}_1 \equiv \gamma_{mel} - \frac{\nu_{mel} \cdot g \cdot T^*}{(M^* + g)^2}$ and $\overline{\Delta}_2 \equiv \alpha_A \cdot \alpha_e \cdot \nu_{mel} \cdot \frac{b}{(M^* + b)^2} \cdot \frac{M^*}{M^* + g}$, Equation (20) becomes

$$\mathrm{P}(\lambda) = (\lambda + \mu_A) \cdot (\lambda + \mu_e) \cdot (\lambda - \overline{\Delta}_1) + \overline{\Delta}_2. \quad \text{Eq. (21)}$$

Further simplification of $\overline{\Delta}_1$ and $\overline{\Delta}_2$ is achieved by substituting T^* from Equation (9b), $\overline{K}$, and Equation (19) into Equation (21):

a) $$\overline{\Delta}_1 = \gamma_{mel} \cdot \frac{M^*}{M^* + g}, \quad \text{Eq. (22)}$$

b) $$\overline{\Delta}_2 = \gamma_{mel} \cdot \mu_A \cdot \mu_e \cdot \frac{b}{M^* + b}.$$

The values of $\overline{\Delta}_1$ and $\overline{\Delta}_2$ are limited to the following ranges (Equation (23)), considering that $M^* \geq 0$ (Equation (8)).

a) $$0 < \overline{\Delta}_1 < \gamma_{mel}, \quad \text{Eq. (23)}$$

b) $$0 < \overline{\Delta}_2 < \gamma_{mel} \cdot \mu_e \cdot \mu_A.$$

A FP is locally asymptotically stable (LAS) if all the real parts of its corresponding eigenvalues are negative. To study the signs of the real parts, Equation (21) was graphically analyzed for different values of $\overline{\Delta}_1$ and $\overline{\Delta}_2$ (Figure 3.3).

Claim 1: Given that all the eigenvalues of a PFP of Equation (1) are real, there exists $\overline{\Delta}_{2_{crit}}$ such that this point is LAS if

a) $$\overline{\Delta}_2 > \overline{\Delta}_{2_{crit}}, \quad \text{Eq. (24)}$$

b) $$\frac{dP(\lambda, \overline{\Delta}_2 = 0)}{d\lambda}\Big|_{\lambda=0} > 0.$$

Proof of Claim 1. To prove sufficiency, assume that Equation (24b) holds. When $\overline{\Delta}_2 = 0$, all the roots of the polynomial in Equation (21) are real. As shown in Figure 3.3a, the largest zero is positive and the rest are negative. A positive value of $\overline{\Delta}_2$ shifts the polynomial graph upwards, leading to a decrease in the value of the largest root, until it changes sign (Figure 3.3b). As a result, the corresponding FP becomes LAS. The

critical value of $\overline{\Delta}_2$, at which the largest root changes sign, is defined by the intersection of the characteristic polynomial with $\lambda = 0$

$$\mathrm{P}\left(\lambda = 0, \overline{\Delta}_2 = \overline{\Delta}_{2_{crit}}\right) = 0. \qquad \text{Eq. (25)}$$

Substitution of Equation (21) in Equation (25) yields

$$\overline{\Delta}_{2_{crit}} = \mu_A \cdot \mu_e \cdot \overline{\Delta}_1. \qquad \text{Eq. (26)}$$

To prove necessity, assume that Equation (24) is violated. As shown in Figure 3.3c, when $\frac{dP(\lambda,\overline{\Delta}_2=0)}{d\lambda}\Big|_{\lambda=0} < 0$ and $\overline{\Delta}_2 = 0$ the largest polynomial zero is positive and the rest are negative, similarly to the condition in Figure 3.3a. A larger value of $\overline{\Delta}_2$ shifts the polynomial upwards, but here the largest zero remains positive and the second biggest one becomes positive (Figure 3.3d). Together, both conditions in Equations (24) are therefore necessary and sufficient for local stability of a PFP with corresponding real eigenvalues.

□

Next, the parameter ranges for which Equation (24b) is satisfied, were determined, in order to express the stability conditions in terms of the parameter space. Equation (21) was differentiated and $\lambda = 0$ was substituted, as follows

$$\frac{dP(\lambda, \overline{\Delta}_2 = 0)}{d\lambda}\Big|_{\lambda=0} = \mu_A \cdot \mu_e - \overline{\Delta}_1 \cdot (\mu_A + \mu_e). \qquad \text{Eq. (27)}$$

Thus, the second necessary parametric condition for stability of a PFP is

$$\overline{\Delta}_1 < \frac{\mu_A \cdot \mu_e}{\mu_A + \mu_e}. \qquad \text{Eq. (28)}$$

Under the estimated parameter values from Table 2.1, the r.h.s of Equation (28) equals about 10 d^{-1}, and the value of $\overline{\Delta}_1$ is about 0.05 d^{-1}. Since according to Equation (23a), the maximum value of $\overline{\Delta}_1$ is γ_{mel} (0.08664 d^{-1}), Equation (28) always holds, and thereby the stability condition in Equation (24b) is always satisfied in the parameter ranges in Table 2.1. In conclusion, increase in the activation rate of $CD8^+$ T cells, reduction of their exhaustion rate, as well as low tumor growth rates enable stability of the corresponding PFP.

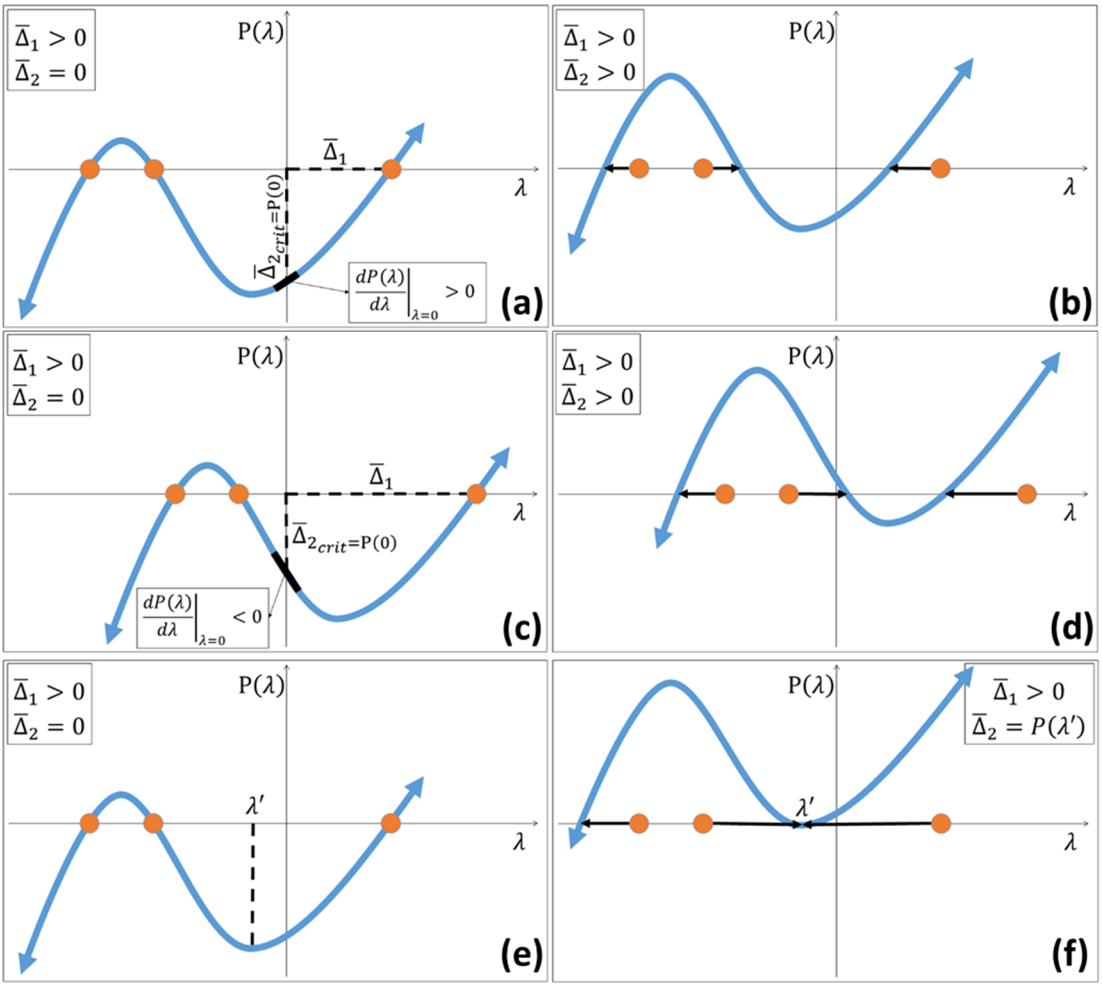

Figure 3.3. Negativity of the real parts of the zeros of the characteristic polynomial from Equation (21).
The sign of the real parts depends on the slope of the polynomial, $\boldsymbol{P(\lambda)}$, at $\boldsymbol{\lambda = 0}$, and the values of $\boldsymbol{\bar{\Delta}_1}$ and $\boldsymbol{\bar{\Delta}_2}$ (Equation (22)). The circles represent the zeros, $\boldsymbol{\lambda}$, of $\boldsymbol{P(\lambda, \bar{\Delta}_2 = 0)}$. The largest zero is $\boldsymbol{\lambda = \bar{\Delta}_1}$. Figures 3.3a,c,e show three different types of polynomials which satisfy $\boldsymbol{\bar{\Delta}_1 > 0}$, according to Equation (23), and $\boldsymbol{\bar{\Delta}_2 = 0}$. These polynomials have two negative and one positive zeros. Figures 3.3b,d,f demonstrate a sign change of one of the zeros of $\boldsymbol{P(\lambda)}$ in (3.3a), (3.3c), and (3.3e), respectively, when $\boldsymbol{\bar{\Delta}_2}$ increases. First, the polynomial in (3.3a) intersects $\boldsymbol{\lambda = 0}$ on the right side of its local minimum, thus satisfying $\boldsymbol{\left.\frac{dP(\lambda)}{d\lambda}\right|_{\lambda=0} > 0}$. If $\boldsymbol{\bar{\Delta}_2 > 0}$ the largest zero approaches the origin until it becomes negative for $\boldsymbol{\bar{\Delta}_2 \geq \bar{\Delta}_{2_{crit}}}$ (3.3b). In this case, all zeros have negative real parts and therefore the corresponding FP is stable. In contrast, if the intersection of $\boldsymbol{P(\lambda)}$ with $\boldsymbol{\lambda = 0}$ lies left of the local minimum, as shown in (3.3c), and if $\boldsymbol{\bar{\Delta}_2 > 0}$, the second large zero changes sign from negative to positive (3.3d). Hence, either one or two zeros have a positive real part and therefore the corresponding FP is unstable. Lastly, zeros can become complex, as shown in (3.3e) and (3.3f). Consider for instance the local minimum on $\boldsymbol{\lambda = \lambda'}$, shown in (3.3e). For $\boldsymbol{\bar{\Delta}_2 = \lambda'}$ the two closest zeros to the minimum coincide and become a complex conjugate for $\boldsymbol{\bar{\Delta}_2 > \lambda'}$, as shown in (3.3f). Sign determination of their real part is graphically not possible and further analytical and numerical calculations are required.

Claim 2: If a pair of PFPs of Equation (1) has only real eigenvalues and if the condition in Equation (24b) is satisfied, the larger PFP (with a larger value of M^*) is always unstable and the smaller one is always LAS.

Proof of Claim 2. Substitution of $\bar{\Delta}_1$, $\bar{\Delta}_2$ and $\bar{\Delta}_{2_{crit}}$ expressions from Equations (22) and (26) in the first necessary stability condition (Equation (24a)) yields

$$\frac{b}{M^* + b} > \frac{M^*}{M^* + g}. \quad \text{Eq. (29)}$$

Simplifying it yields

$$M^{*2} < bg. \quad \text{Eq. (30)}$$

Substitution of M^{*2} from Equation (12) in Equation (30) yields

$$M^* < -\frac{2bg}{b + g - \bar{K}}. \quad \text{Eq. (31)}$$

In order to determine the stability of each FP in a system with two FPs, the expression of M^* from Equation (13) was substituted into Equation (31):

$$\pm\sqrt{(b + g - \bar{K})^2 - 4b \cdot g} < -\frac{4b \cdot g}{b + g - \bar{K}} - \bar{K} + (b + g). \quad \text{Eq. (32)}$$

The r.h.s of Equation (32) can be written as:

$$-\frac{4b \cdot g}{b + g - \bar{K}} - \bar{K} + (b + g) = \frac{(b + g - \bar{K})^2 - 4b \cdot g}{b + g - \bar{K}}. \quad \text{Eq. (33)}$$

Substitution of Equation (33) into Equation (32) yields:

$$\pm\sqrt{(b + g - \bar{K})^2 - 4b \cdot g} < \frac{(b + g - \bar{K})^2 - 4b \cdot g}{b + g - \bar{K}}. \quad \text{Eq. (34)}$$

According to Equation (18), the r.h.s of Equation (34) is negative, and therefore this inequality is never satisfied for a plus sign in the l.h.s. Therefore, the necessary condition in Equation (24a) does not hold for the larger PFP, M^+, indicating that it is always unstable.

For the lower PFP, M^-, both sides of Equation (34) were multiplied with -1 and squared to yield:

$$1 > 1 - \frac{4b \cdot g}{(b + g - \bar{K})^2}. \qquad \text{Eq. (35)}$$

According to Equation (35), the necessary condition in Equation (24a) is always satisfied for M^-. Thus, if the second necessary condition in Equation (24b) is always satisfied for M^-, the corresponding PFP is always stable. This claim implies that stability of the tumor depends on its size, and that large tumors are less likely to be stable.

□

PFPs with complex eigenvalues are unstable in a treatment-free scenario but can be stable under ICI-increased immune efficacy

Both stability conditions described by Equation (24) relate to the case in which all zeros of the characteristic polynomial are real. However, the zeros can also be complex, with positive or negative real parts. The parametric conditions for negativity of the real parts of complex zeros were determined. As shown in Figure 3.3e and Figure 3.3f, two neighboring zeros can collide, subsequently becoming a conjugate complex pair (when $\bar{\Delta}_2$ becomes larger than the local minimum value of the characteristic polynomial with $\bar{\Delta}_2 = 0$, which lies between these zeros; marked by λ' in Figure 3.3e). Due to the continuity of root values in the polynomial coefficients, and since the condition in Equation (24b) is always satisfied under the estimated parameter values, when the conjugate complex pair is close to λ', its real parts are negative. However, for certain parameter values the real parts may change sign, namely, the system undergoes Hopf bifurcation [116]. The biological meaning of this is that tumors, whose system parameters correspond to negative real parts of all the eigenvalues of the Jacobi matrix, can be stabilized, while tumors, whose eigenvalues in the corresponding mathematical system have positive real parts, are unstable.

Since an explicit solution of the characteristic polynomial in its general form is hard to obtain, determination of the sign of the real part of the zeros is not always possible. Therefore, derivation of the stability conditions in this case requires further analysis, for example, by the application of the Hurwitz-Routh stability criterion [117-120], and

numerical calculation of the eigenvalues of the Jacobi matrix. Here, the conditions for a Hopf bifurcation were analytically determined in the system at hand.

Consider a general form of a 3rd order characteristic polynomial with one negative real zero $\lambda = -\lambda_0$, where $\lambda_0 > 0$, and one conjugate pair of complex zeros $\lambda_1 \pm i\omega_1$, where $\omega_1 > 0$. The corresponding system undergoes a Hopf bifurcation when the real parts of the two corresponding zeros are simultaneously zeroed, that is $\lambda_1 = 0$. The general form of the characteristic polynomial is then:

$$(\lambda + i\omega_1) \cdot (\lambda - i\omega_1) \cdot (\lambda + \lambda_0) = 0. \quad \text{Eq. (36)}$$

Opening parenthesis yields:

$$\lambda^3 + \lambda^2 \cdot \lambda_0 + \lambda \cdot {\omega_1}^2 + \lambda_0 \cdot {\omega_1}^2 = 0. \quad \text{Eq. (37)}$$

The necessary conditions for a Hopf bifurcation are deduced from the conditions on the polynomial coefficients (b_i):

$$b_0 = \lambda_0 \cdot {\omega_1}^2 > 0, \quad \text{Eq. (38)}$$
$$b_1 = {\omega_1}^2 > 0,$$
$$b_2 = \lambda_0 > 0,$$
$$b_3 = 1.$$

According to equation (38), a Hopf bifurcation exists in the system when all the coefficients of the characteristic polynomial in Equation (21) are positive.

These coefficients are summarized here:

$$b_0 = \overline{\Delta}_2 - \overline{\Delta}_{2_{crit}}, \quad \text{Eq. (39)}$$
$$b_1 = \mu_A \cdot \mu_e - \overline{\Delta}_1 \cdot (\mu_A + \mu_e),$$
$$b_2 = \mu_A + \mu_e - \overline{\Delta}_1,$$
$$b_3 = 1.$$

The first and second coefficients in Equation (39) are positive when Equations (24a) and (24b) are satisfied. Positivity determination of b_2 under consideration that $\overline{\Delta}_1 > 0$ yields the remaining condition for a Hopf bifurcation:

$$b_2 = \mu_A + \mu_e - \overline{\Delta}_1 > 0, \text{ or} \quad \text{Eq. (40)}$$
$$\overline{\Delta}_1 < \mu_A + \mu_e.$$

Under realistic assumptions on the immune system's parameters (see Table 2.1), $\mu_A + \mu_e$ is approximately 0.4 d^{-1}. Since according to Equation (23a), the maximum value of $\overline{\Delta}_1$ is $\gamma_{mel} \approx 0.004\, d^{-1}$, Equation (40) is always satisfied, and therefore a Hopf bifurcation takes place for all parameter values. Significant reduction of the exhaustion rates, namely μ_A, and μ_e, for example under treatment with ICI, can violate Equation (40), and impose stability on the corresponding PFP, as well as the tumor size.

The condition deduced in above is a consequence of the Ruth Horowitz criterion. The corresponding Routh array of the polynomial is:

b_3	b_1	0
b_2	b_0	0
$\frac{b_1 \cdot b_2 - b_0 \cdot b_3}{b_2}$	0	0
b_0	0	0

According to the Routh Horowitz criterion for stability of the corresponding FP, $b_i > 0$ must hold, as well as that all the terms in the left column of the Routh array must be positive. Here, the first, second, and fourth terms are positive. Substituting $b_3 = 1$ in the third term yields $\frac{b_1 \cdot b_2 - b_0}{b_2}$. In the polynomial of Equation (37), the real parts of the complex roots are zero, and therefore $\frac{b_1 \cdot b_2 - b_0}{b_2} = 0$, namely $b_1 \cdot b_2 = b_0$, and the complex roots are $\lambda = \pm i\sqrt{b_1}$. The condition of stability of the corresponding FP is

$$b_1 \cdot b_2 - b_0 > 0 \qquad \text{Eq. (41)}$$

Substituting b_i from Equation (39) yields

$$\mu_A \cdot \mu_e \cdot \left(\mu_A + \mu_e - \gamma_{mel} \cdot \frac{b}{M+b} - 2 \cdot \overline{\Delta}_1\right) + (\mu_A + \mu_e) \cdot \overline{\Delta}_1 \cdot (\overline{\Delta}_1 - 1) > 0 \qquad \text{Eq. (42)}$$

Stability of PFPs is linked to a small tumor burden and an enhanced activation of CD8⁺ T cells

For a better understanding of the local stability patterns, the FPs and the corresponding eigenvalues were numerically calculated for 62,500 parameter sets. In each set, the values of α_e, and μ_e, specified in Table 2.1, were modified from 1 to 9,000 fold, and 1/9,000 to 1 fold, respectively. The focus was chosen on changes in α_e and μ_e due to their direct effect on the number of CD8⁺ T cells in the host. In addition, the effect of the tumor growth rate on the local stability of the FPs was examined by repeating the above numerical analysis for both the minimal and the maximal estimated value of γ_{mel} in Table 2.1. The rest of the parameters remained unchanged from their reference values in Table 2.1. For each parameter set the stability of each corresponding FP was determined by numerical calculation of the eigenvalues of Equation (21). A FP was recorded as locally asymptotically stable, if all real parts of its corresponding eigenvalues were negative. Otherwise, the FP was flagged as unstable. The results of these computations, are listed below (see also Figure 3.4).

1. In a system with two PFPs, the larger PFP is unstable over the whole range of α_e, μ_e, and γ_{mel}. The numerical analysis indicated that the larger PFP has a single real-positive eigenvalue over the examined range of α_e, μ_e, and γ_{mel}. The rest of the eigenvalues can be real or complex, all having negative real parts (not shown).

2. **Increase in the activation rate of CD8⁺ T cells, α_e, leads to local stability of the smaller PFP, while reduction in the exhaustion rate of CD8⁺ T cells, μ_e, leads to local instability.** Under the minimal and maximal values of γ_{mel} from Table 2.1, locally stable FPs are associated with low values of μ_e, and relatively large values of α_e. In addition, the FPs under the minimal value of γ_{mel} have higher stability when compared to those under the maximal value of γ_{mel}.

3. **Instability of the smaller PFP in a system with two PFPs is due to positive real parts of a single conjugate pair of complex eigenvalues.**

All analyzed unstable FPs have positive real parts of only complex eigenvalues.

Figure 3.4 summarizes the results of both the theoretical and the numerical local stability analyses. One can see in this summary that the larger PFP is always unstable, while the smaller one is unstable only when the corresponding Jacobi matrix has two complex eigenvalues with real parts, which change sign due to Hopf bifurcation.

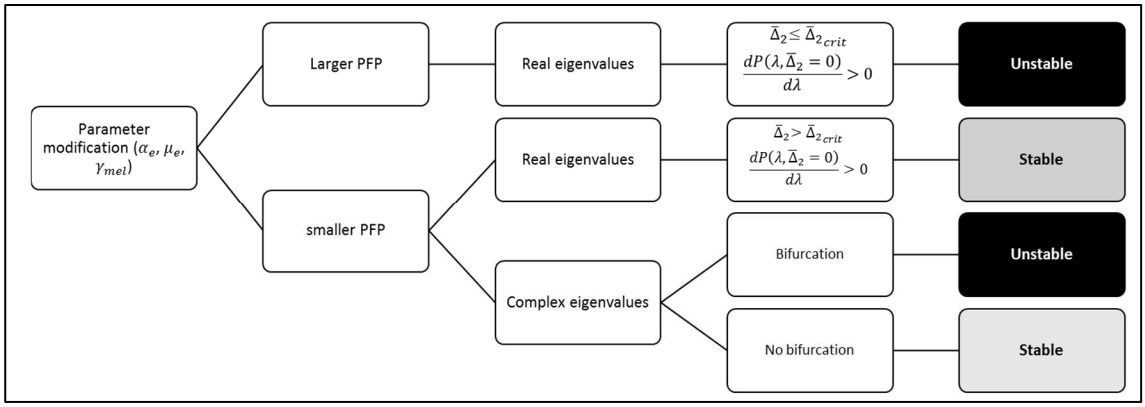

Figure 3.4. Summary of the local stability analysis of systems with two PFPs. The parameters $\boldsymbol{\alpha_e}$, $\boldsymbol{\mu_e}$ and $\boldsymbol{\gamma_{mel}}$ stand for the activation rate of CD8⁺ T cells, their exhaustion rate and the tumor growth rate, respectively. The coefficients $\bar{\Delta}_2$, $\bar{\Delta}_{2_{crit}}$ and the function $\boldsymbol{P}(\boldsymbol{\lambda})$ are defined in Equations (21), (22), and (26).

Phase-plane analysis emphasizes the role of the initial tumor burden on convergence towards a stable PFP, and reveals oscillations around an unstable PFP

Next, the global dynamics of the system was studied by a phase-plane analysis, in order to study the dynamics of the cell populations away from the PFPs. To this end, the time course of the values of the two most relevant variables was plotted, namely effector CD8⁺ T cells (T) and tumor cells (M), versus each other. Representative phase portraits of the system, having zero, one, or two FPs are shown and explained in the following paragraphs. The simulation results are summarized in Figure 3.5.

No PFPs

Under the estimated parameters from Table 2.1, the system has no PFPs. As shown in Figure 3.5a, the number of tumor cells in this case grows uncontrollably, while the number of effector CD8⁺ T cells eventually reaches saturation.

A single PFP

As previously shown in Figure 3.1 and Figure 3.2, for certain parameter values, the condition in Equation (17) is satisfied and the system has a single PFP. In the particular

phase portrait shown in Figure 3.5b, the obtained FP is a saddle node, which refers to a consolidation of a stable and an unstable FP. The part of this phase portrait, for which the initial total number of tumor cells in the host is less than $5 \cdot 10^6$, constitutes the basin of attraction. All trajectories, beginning inside this basin of attraction, converge to the FP, while all trajectories beginning with a larger number of tumor cells diverge away from this point. The biological implication of this is that tumors with initially less than $5 \cdot 10^6$ cells will stabilize.

Two PFPs

Depending on the parameter values, the system can have two PFPs. Exemplary phase portraits of such systems are shown in Figure 3.5c-e. Each of these systems has different parameters, but the same value of $\overline{K}$ and the same number of tumor cells in steady state. It was found that modification of α_e, and μ_e can induce oscillatory changes in the number of tumor cells. First, as shown in Figure 3.5c, increasing the activation rate of $CD8^+$ T cells generates a locally stable PFP and an unstable PFP. If the initial size of the tumor cell population is located within the basin of attraction of the smaller PFP, the number of tumor cells approaches this point with damped oscillations and the disease becomes stable. However, if the initial size of the tumor cell population is located outside the basin of attraction, the corresponding trajectory escapes from the larger PFP, which results in an uncontrollable tumor growth and disease progression. Secondly, as shown in Figure 3.5d, reducing the exhaustion rate of $CD8^+$ T cells generates two PFPs. The number of tumor cells around the smaller FP undergoes increasing oscillations. In some cases, the amplitude is so large that the tumor will virtually disappear and then grow again, escaping from host immunity. When the initial number of cancer cells is close to the value at this FP, the system will eventually converge to this FP (Figure 3.5d, magnified area). When the initial number of cancer cells is close to the larger PFP, it will either escape from it towards the smaller PFP or grow uncontrollably. Thus, considering two similar sets of initial conditions, one mapping a point, located slightly above the larger PFP, and the other mapping a point, located slightly below this point, it is noticeable that each of these points evolves differently in time, corresponding to a different disease fate. The evolution of the first set leads to temporary shrinkage or tumor stability, while the

evolution of the second set leads to disease progression. In addition to the effects of the host immunity, reduction of the tumor growth rate also leads to generation of PFPs in the system. As shown in Figure 3.5e, reducing the value of γ_{mel} leads to a sharp, non-oscillatory decay in the number of tumor cells towards the smaller PFP, or escape from the larger FP (Figure 3.5e), depending on the initial number of tumor cells.

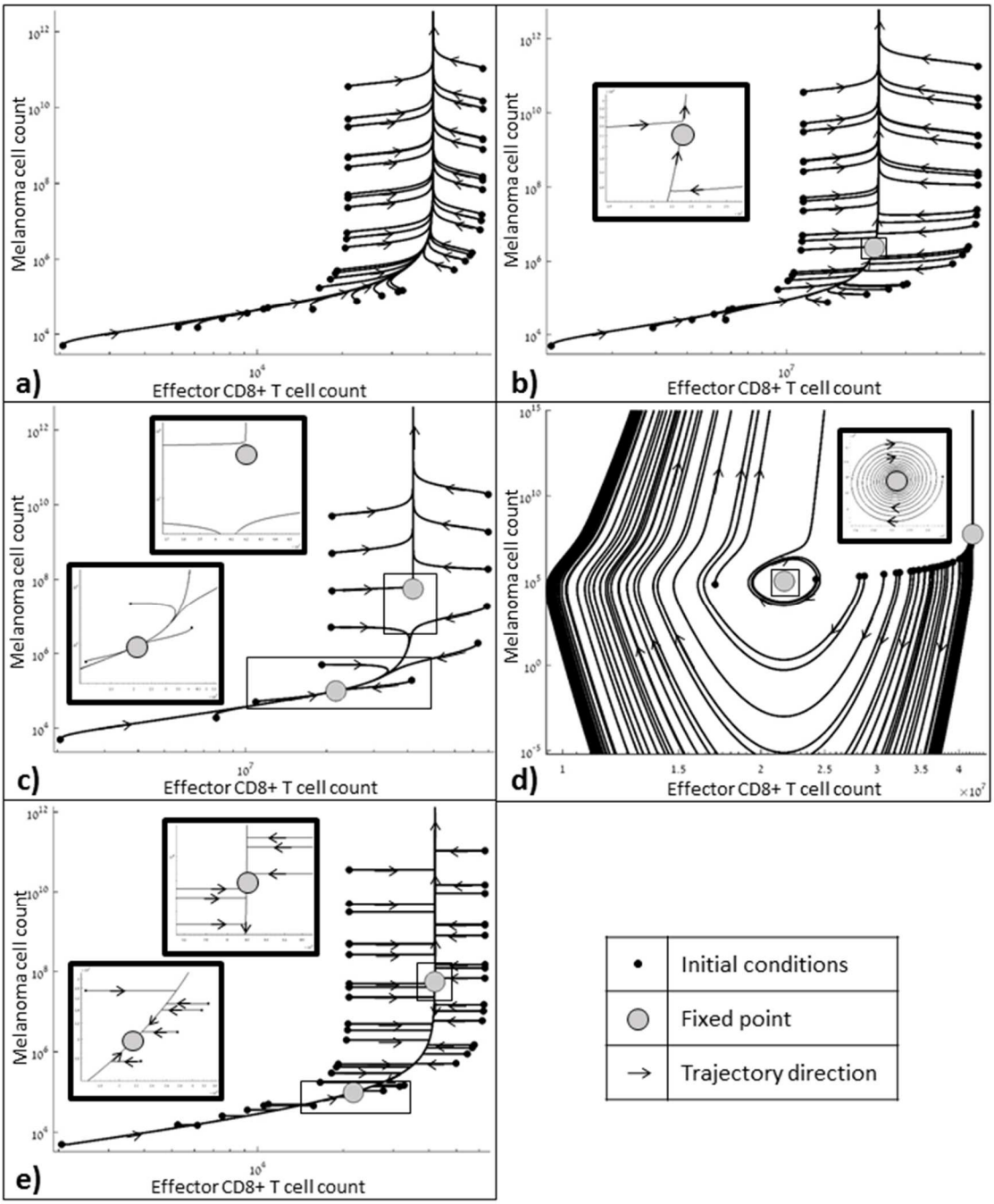

Figure 3.5. Phase plane analysis captures disease control for an initially low tumor burden.

The figure shows representative phase planes of the 3-dimensional treatment-free system described in Equation (1), under substitution of $a_{pem} = b_{pem} = 1$. The phase planes are projected here on the effector CD8⁺ T cells (T) – melanoma cells (M) plane. The black curves represent trajectories of $\left(\boldsymbol{T}(\boldsymbol{t}), \boldsymbol{M}(\boldsymbol{t})\right)$ and the small circles mark the initial points of each curve. Arrows mark the direction of the trajectories. Big circles denote FPs, at which the number of cells remains constant with time. It separates between different dynamic patterns of the cell populations. Information on the parameter values and initial number of cells is summarized in Table 3.1. Figure 3.5a shows a phase portrait of a system with the parameter values estimated from the literature (Table 2.1). No FPs have been identified, indicating tumor escape and its eventual uncontrollable growth. Figure 3.5b shows a phase portrait of a system with a single FP, (thin frame with a zoom in in the thick frame). This point is marked by a black circle in Figure 3.2. Initially large tumors grow in size, while initially small tumors evolve to be limited by the immune system. As shown in (b), starting from an initial number of about 10^7 tumor cells results in different fates of the tumor dynamics. Figure 3.5c, Figure 3.5d, and Figure 3.5e represent phase planes of different systems with two FPs, characterized by different parameter values. (c) Increased $\boldsymbol{\alpha_e}$ generates curved trajectories which tend to the lower FP. This indicates short oscillations (stable focus; thin frame with a zoom-in within the thick frame). Trajectories with the initial number of tumor cells larger than ~$5 \cdot 10^6$ escape from the larger FP (unstable focus; thin frame with a zoom in in the thick frame). (d) Reduced value of $\boldsymbol{\mu_e}$ leads to spiral trajectories, spiraling away from a FP, which indicates growing oscillations. Interestingly, trajectories, which begin close to this FP (thin frame) are attracted to it, as zoomed in the thick frame. (e) Reduced value of $\boldsymbol{\gamma_{mel}}$ results in a non-oscillatory dynamics, such that trajectories, which begin with initially small number of tumor cells converge into a smaller stable focus (lower thin frame with a zoom in in the lower thick frame), and trajectories, which begin with a larger number of tumor cells escape from a larger unstable focus (upper thin frame with a zoom in in the upper thick frame).

Table 3.1. Numerical description of the phase planes shown in Figure 3.5.

Figure	Value of the changed parameter*	Range of initial number of tumor cells ($\boldsymbol{M^0}$)	Initial number of immune cells (perturbation from a quasi-steady state) **
(a)	-	$10^4 – 12^{10}$	(0.5 , 1.5)
(b)	$\alpha_e = 0.8318 \cdot 557.22\ d^{-1}$ ***	$10^4 – 12^{10}$	(0.5 , 2.5)
(c)	$\alpha_e = 0.8318\ \cdot 10^3[d^{-1}]$	$10^4 – 12^{10}$	(0.5 , 1.9)
(d)	$\mu_e = 0.1777 \cdot 10^{-3}[d^{-1}]$	$10^{4.8} – 10^7$	1
(e)	$\gamma_{mel} = 0.0449 \cdot 10^{-3}[d^{-1}]$	$10^4 – 12^{10}$	(0.5 , 1.5)

** Relative to the reference value from Table 2.1.*

*** The initial conditions of immune cells were calculated according to Equation (9), by assuming that the number of immune cells adjusts itself rapidly to any change in the number of tumor cells. In order to determine the dynamic patterns over a larger range of initial conditions, the initial number of cells were perturbed from the ones calculated in Equation (9) by multiplying all the immune cells by a constant, specified here for each subfigure in Figure 3.5.*

**** This value for α_e satisfies the condition for a single FP $\alpha_e \cdot \left(\frac{\nu_{mel} \cdot \alpha_A}{\gamma_{mel} \cdot \mu_e \cdot \mu_A}\right) = b + g + 2 \cdot \sqrt{b \cdot g}$ (see Equation (17)).*

To better visualize the outcome of the model simulation for each steady state, representative initial conditions were chosen around the smaller PFP for each steady state shown in Figure 3.5c-d, and the time series of the corresponding trajectories was plotted (Figure 3.6). It can be seen that under a reduced exhaustion rate of $CD8^+$ T cells, the tumor size oscillates around the smaller PFP. As the initial conditions get closer to this FP, the frequency of the oscillations increases (Figure 3.6b-d). Their amplitude decays and then stabilizes very close to this FP, while increasing in trajectories that are further away from the smaller PFP.

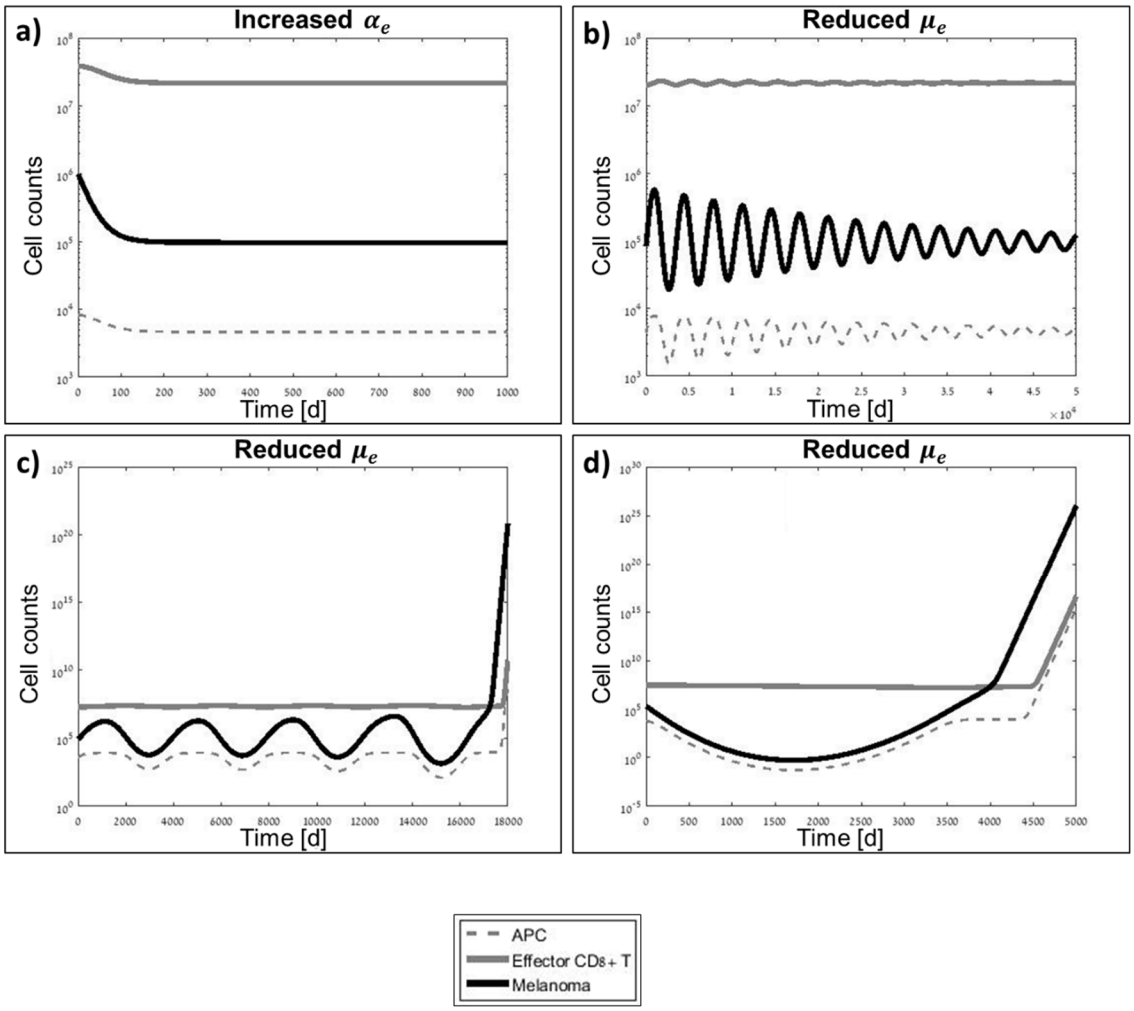

Figure	Initial number of melanoma cells
(a)	10^6
(b)	$8.5 \cdot 10^4$
(c)	$8 \cdot 10^4$
(d)	$2 \cdot 10^5$

Figure 3.6. Representative time series for the number of immune and tumor cells around the fixed points.
Figure 3.6a and Figure 3.6b-d are plotted for the same parameter sets in the phase portraits as in Figure 3.5c, and Figure 3.5d, respectively. The initial number of immune cells was set under the assumption of quasi-steady state, that is, the number of immune cells adjusts itself to the number of tumor cells, according to Equation (9).

The dynamic patterns of tumor growth, shown in Figure 3.6, correspond to different types of response to immunotherapy. It is noticeable in Figure 3.6a, that an increase in the activation rate of $CD8^+$ T cells due to treatment, stabilizes the tumor size within

a period of a few months. The larger the activation rate gets, the smaller is corresponding tumor size at steady state is, and the larger the basin of attraction of this stable FP is. On the other hand, patients whose therapy leads to significant reductions in exhaustion rates of immune cells (Figures 3.6b, 3.6c, 3.6d) can experience different disease fates, depending on the ratio between the activation and the exhaustion rates of $CD8^+$ T cells, as well as on the initial number of tumor cells, and on the number of immune cells. For large ratios between the activation and the exhaustion rates of $CD8^+$ T cells, the value of $\bar{\Delta}_2$ is large enough for two neighboring polynomial zeros to coincide and form a complex-conjugate pair (Figure 3.3e,f). This results in a period of oscillatory tumor dynamics, followed by stability of tumor size or an uncontrollable growth. Under the initial number of tumor and immune cells lying in the closest trajectory to the smaller FP, the oscillations decay, which leads to a stable tumor size (Figure 3.6*b*). In contrast, on a different trajectory, which starts further from this FP, the corresponding tumor size oscillates for a while, followed by an uncontrollable growth (Figure 3.6c). Away from a stable PFP, and when the initial number of $CD8^+$ T cells is larger than its number at steady state, the tumor shrinks considerably, only to reappear after about a decade (Figure 3.6*d*). Taken together, these results suggest that when an immunotherapeutic intervention increases the activation rate of effector CD8+ T cells, immunotherapy will lead to disease stabilization. In contrast, when immunotherapy relieves the exhaustion of $CD8^+$ T cells, the outcomes may vary from decaying oscillatory convergence, through a stable tumor size, to uncontrollable growth, depending on the initial conditions of the tumor and immune cells.

3.2. Predicting Response to Pembrolizumab in Metastatic Melanoma by a New Personalization Algorithm

Summary: At present, immune checkpoint inhibitors, such as pembro, are widely used for the treatment of advanced non-resectable melanoma, as they induce more durable responses than other available treatments. However, the overall response rate does not exceed 50% and, considering the high costs and low life expectancy of nonresponding patients, there is a need to select potential responders before therapy. This chapter describes the development of a new personalization algorithm which can

be useful in the clinical setting, for predicting time to disease progression under pembro treatment. First, a simple mathematical model for the interactions of an advanced melanoma tumor with both the immune system and the immunotherapy drug pembro was developed. The model was implemented in an algorithm which, in conjunction with clinical pre-treatment data, enabled prediction of the personal patient response to the drug. To develop the algorithm, clinical data of 54 patients with advanced melanoma under pembro was retrospectively collected. In addition, personal pretreatment measurements were correlated to the mathematical model parameters. Using the algorithm together with the longitudinal tumor burden of each patient, the personal mathematical models were identified and simulated to predict the patient's time to progression. The algorithm's prediction capacity was validated by the Leave-One-Out cross validation methodology. Among the analyzed clinical parameters, the baseline tumor load, the Breslow tumor thickness, and the status of nodular melanoma were significantly correlated with the activation and exhaustion rates of $CD8^+$ T cells. Using the measurements of these correlates to personalize the mathematical model, the time to progression of individual patients was predicted (Cohen's $\kappa = 0.489$**)**. Comparison of the predicted and the clinical time to progression in patients progressing during the follow-up period showed moderate accuracy ($R^2=0.505$). The results suggest that a relatively simple mathematical mechanistic model, implemented in a personalization algorithm, can be personalized by baseline clinical data before immunotherapy onset. The algorithm, currently yielding moderately accurate predictions of individual patients' response to pembro, can be improved by training on a larger number of patients. Algorithm's validation by an independent clinical dataset will enable its use as a tool for treatment personalization.

3.2.1. Development of the personalization algorithm

The personalization algorithm developed for predicting response to pembro in a patient with advanced melanoma is briefly described in Figure 3.7.

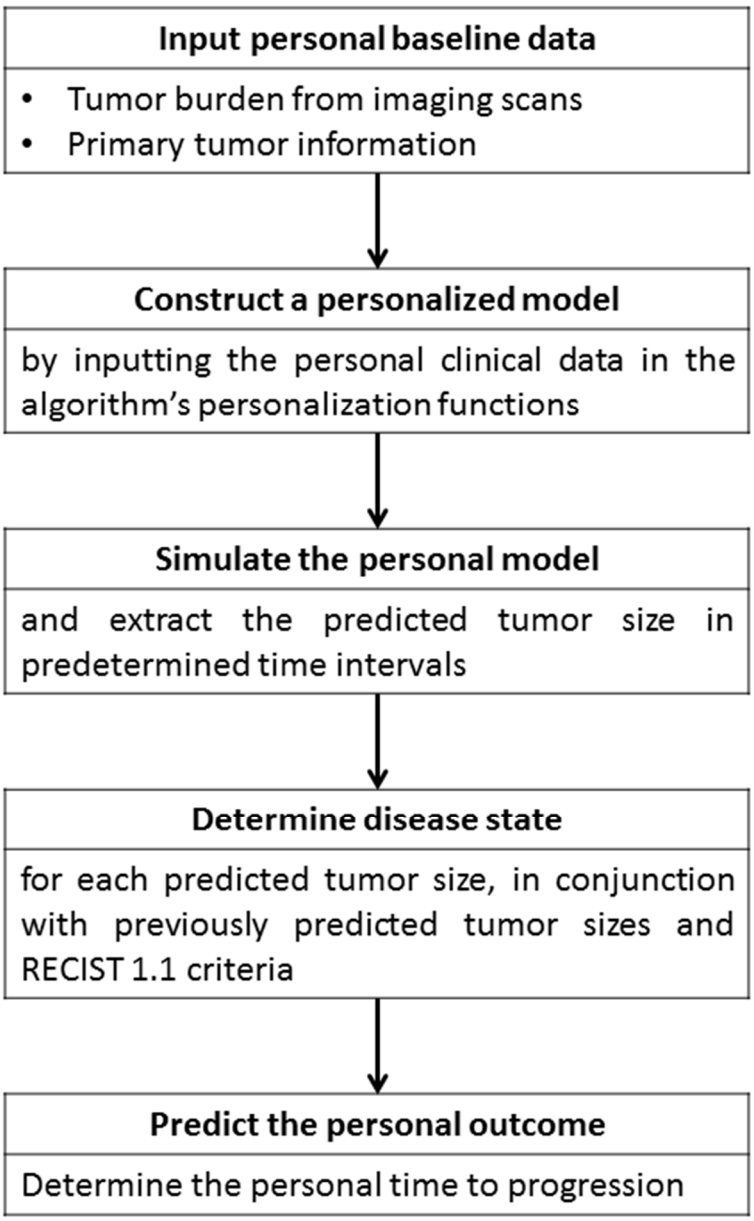

Figure 3.7. Schematic description of the personalization algorithm for response prediction of patients with advanced melanoma to pembro.
The required input includes baseline clinical data, which is generated as part of the standard follow-up routine. The personalization functions of the algorithm are applied on the patient's clinical data to identify their personal model. By simulating this model, the predicted tumor size is extracted in particular time intervals, for example, every three months, and the predicted response status in each time point is determined by RECIST 1.1 guidelines. From predicting the timing of PD, the algorithm provides the personal time to progression (TTP).

3.2.2. Algorithm development: retrieving personal model parameters and evaluating time to progression in the training set

This subsection describes the first development step of the personalization algorithm, namely creation of the training set.

In the clinical results, all four response categories of RECIST 1.1 were observed during the follow-up period: (i) Full response of the target lesions, by the end of the follow-up period (e.g., Figure 3.8a). (ii) Shrinkage of the target lesions by more than 30% from baseline size, by the end of the follow-up period (e.g., Figure 3.8b). (iii) progression of the target lesions, indicated by an increase of ≥ 20% relative to the nadir, by the end of the follow-up period (e.g., Figure 3.8c). (iv) Stability in the size of the target lesions, so that the tumor size at the end of the follow-up period does not meet the aforementioned conditions of shrinkage or progression (e.g., Figure 3.8d). The clinical results were employed for retrieving the individual model parameters by fitting the model to the SOD time series, calculated from the clinical data (see Methods section).

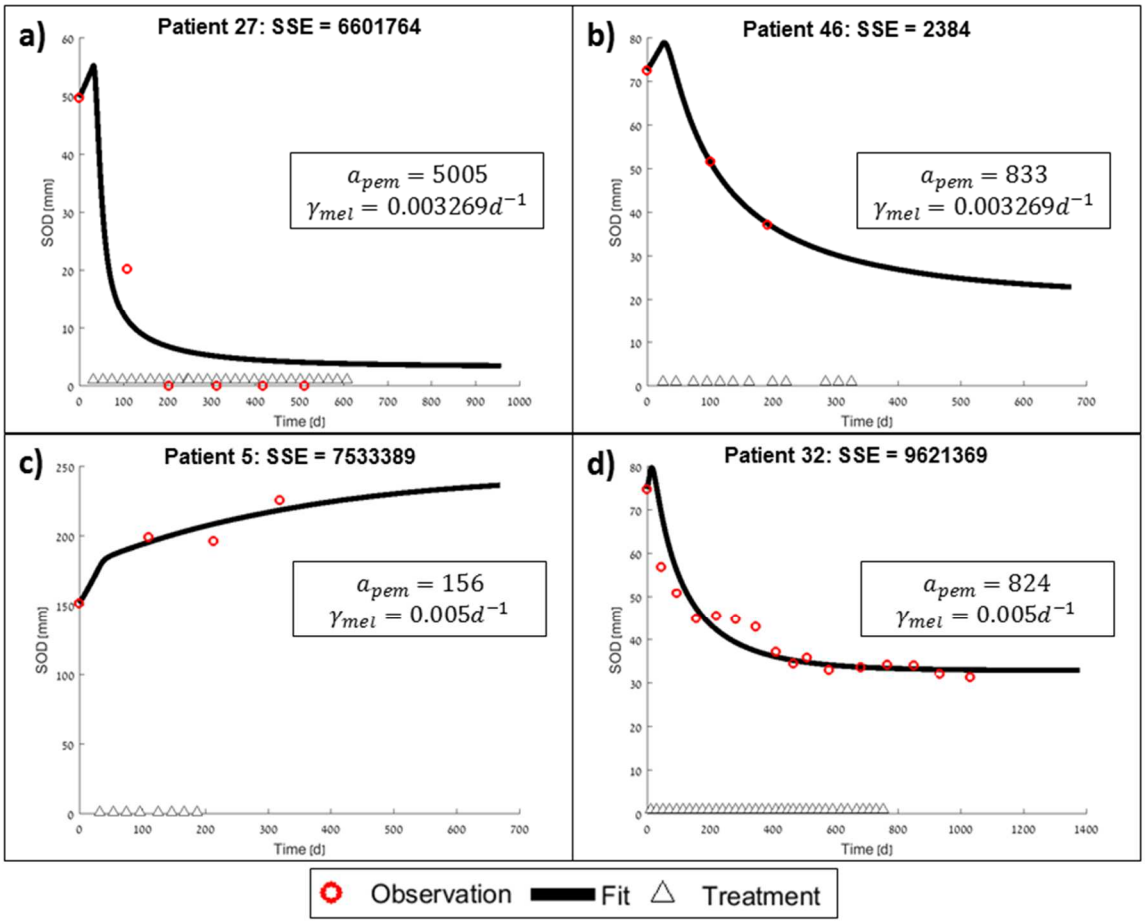

Figure 3.8. Representative fitting results of four different patients.
(a) All target lesions completely shrunk under treatment with pembro. (b) Target lesions shrunk by more than 30% from baseline size. (c) Target lesions increased by over 20%, relative to the nadir measurement. (d) The disease was stabilized, as determined when the conditions for disease progression, partial response and complete response, were not met. The ranges of the personalization parameters used for the simulations are specified in Table 2.4. SOD = Sum of Diameters. Extended fitting results beyond the last time point of the clinical data was plotted for technical reasons, namely in order to make sure that no abnormal patterns appear in the simulated tumor size for a decent time period after the end of the clinical data. Still, only the fitting results within the clinical data time range were used for the following analyses.

In order to estimate the goodness of the fit of the models, the clinically observed and the fitted tumor sizes of all the patients in the cohort were compared (Figure 3.9). Comparison of the absolute and log-scaled sizes yielded R^2 = 0.94 and R^2 = 0.96, respectively.

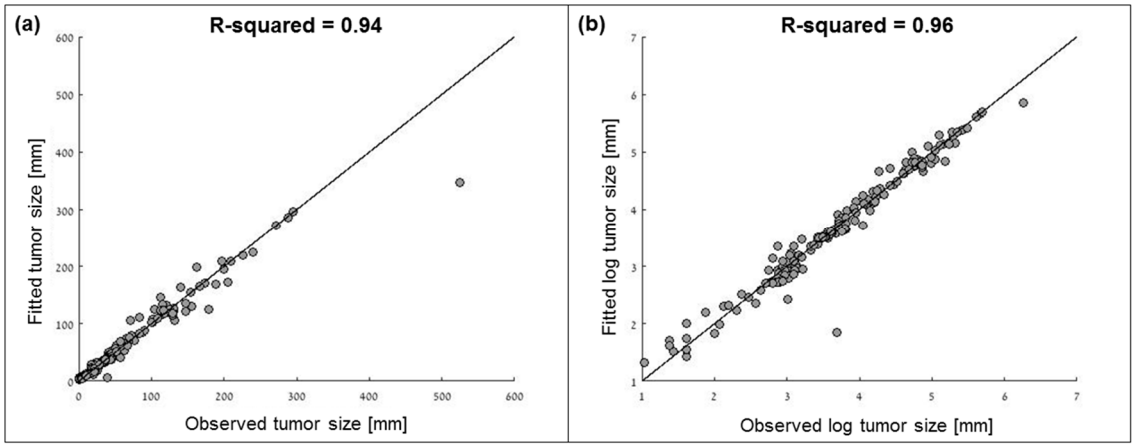

Figure 3.9. Fitting results of the model -simulated tumor size in the patients' cohort (N=54), versus the clinically observed tumor sizes.
(a) Each point shows the fitted versus the clinically measured Sum of Diameters (SOD) of a patient, at the time an imaging assessment took place in the clinic. The observed SOD on the reference line equals to the fitted values. The personalization parameter ranges used for the simulation are specified in Table 2.4, and the values of the other model parameters are summarized in Table 2.1. (b) Fitted versus observed SOD on a log scale. Values of 0 were excluded from the dataset for calculation of R-squared.

In the following, the TTP derived from the fitting results was compared to the clinically observed TTP, by counting the number of disease progression events in each one of three different time intervals, as described in the Methods section 2.8, and summarized in Table 3.2.

Table 3.2. Model-simulated (Simul.) versus clinically- measured (Clinic.) time to progression (TTP).
The simulated TTP was obtained by fitting the simulations of the mathematical model in Equation (1). Each table cell includes the number of cases (above) and the percentage of the total number of patients in the cohort (in brackets below; N = 54), which satisfy one of the six outcomes described in the Methods section 2.8. The bold numbers represent the number of cases, for which the algorithm correctly predicted that progression will occur, and correctly predicted the time interval during which progression would occur; ***Cohen's κ = 0.773****.*

Clinic. TTP / Simul. TTP	0 – 90 days	91 – 150 days	151 – 365 days	No PD during follow-up
0 – 90 days	**8** (14.8 %)	0 (0 %)	2 (3.7 %)	0 (0 %)
91 – 150 days	0 (0 %)	**3** (5.6 %)	0 (0 %)	0 (0 %)
151 – 365 days	0 (0 %)	0 (0 %)	**2** (3.7 %)	0 (0 %)
No PD during follow-up	2 (3.7%)	1 (1.85 %)	1 (1.85 %)	**35** (64.8 %)

From the histogram of the fitted a_{pem} values (Figure 3.10), it is deduced that the distribution of this parameter in the patient population is approximately logarithmic. This implies that lower values are more frequently encountered than large ones. Thus, in order to reduce the bias in the prediction of this parameter, a logarithmic transformation was applied to the values of a_{pem}.

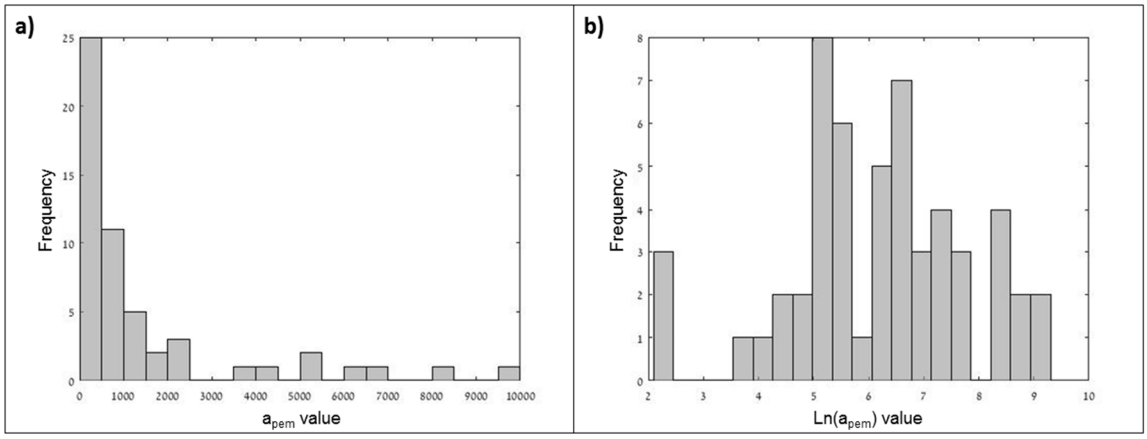

Figure 3.10. Histogram of the values of the maximum effect of pembro on activation of CD8⁺ T cells.
The values of this parameter, denoted a_{pem}, were obtained from fitting of the mathematical model to the clinically observed tumor size. The initial range of a_{pem} for the fit is defined in Table 2.4. (a) Absolute values of a_{pem}. (b) Transformed values of $ln(a_{pem})$.

3.2.3. Predictions of the personal models

In order to predict the individual values of the personal model parameters in new patients, correlations between the values of the model parameters of the patients in the training set, and different combinations of the potential covariates, available in the clinical database, were first analyzed.

Table 3.3 shows that the value of a_{pem} is most correlative with the baseline SOD (Table 3.3.a), and the value of γ_{mel} is most correlative with the Breslow tumor thickness and the status of nodular melanoma (Table 3.3.b).

Table 3.3. Correlations between model parameters and the clinical measures from Table 2.5 (see Methods section 2.7.2).

Table 3.3.a. Pearson correlations between the values of model parameter $\boldsymbol{ln(a_{pem})}$ and clinical measures.
Among the tested clinical measures, the baseline Sum of Diameters (SOD) was found to be most significantly correlated with $\boldsymbol{ln(a_{pem})}$ (in bold).

Potential clinical covariate	Pearson correlation coefficient	Significance (p-value)
Age	0.051	0.77
Breslow tumor thickness	-0.089	0.53
LDH	-0.573	$9.2 \cdot 10^{-6}$
LY%	0.370	0.01
SOD at the baseline	**-0.703**	**$3.5 \cdot 10^{-9}$**

Table 3.3.b. Correlation between the model parameter $\boldsymbol{\gamma_{mel}}$ and the clinical measures.

Table 3.3.b.1. Relationships between $\boldsymbol{\gamma_{mel}}$ and clinical measures, with multiple potential values.
The maximal AUC and Cohen's kappa (κ) values, obtained from ROC analysis were obtained for Breslow tumor thickness (in bold).

Potential clinical covariate	ROC AUC	Maximal Cohen's kappa (κ)
Age	0.56	0.219
Breslow tumor thickness	**0.63**	**0.304**
LDH	0.52	0.128
LY %	0.52	0.156
SOD at the baseline	0.61	0.251

Table 3.3.b.2. Relationships between $\boldsymbol{\gamma_{mel}}$ and binary covariates.
The status of nodular melanoma had the largest kappa value (in bold).

Potential clinical covariate	Cohen's kappa (κ),
Malignant melanoma status	0.185
Nodular melanoma status	**0.258**
BRAF V600 status	0.124

Using k-NN regression and classification methods, we estimated the values of a_{pem} and γ_{mel} of each patient in the validation set, from the covariate values of the patients in the training set (LOO CV, see Methods section 2.7.2). We then simulated the tumor size dynamics for each personal model with the patient-specific parameter values. From the simulation results we obtained the personal response as determined by RECIST 1.1, and consequently the TTP. We repeated this analysis for all the covariates listed in Table 3.3, and their combinations, and evaluated the quality of the prediction of disease progression events. The R^2 value of the k-NN algorithm-derived parameter values versus the fitted ones was calculated, in order to estimate the goodness of fit. The value of $R^2 = 0.47$ obtained for the baseline SOD, refers to results of LOO CV. The plot of the fitted $ln(a_{pem})$ value for each patient, versus the k-NN algorithm-derived value is shown in Figure 3.11.

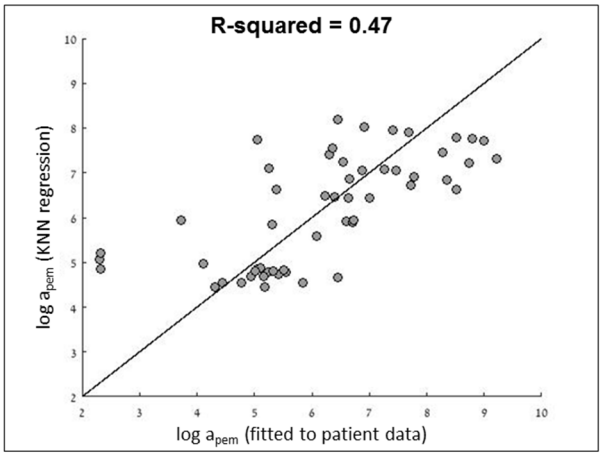

Figure 3.11. Patient-specific logarithmic values of the maximum effect of pembro on activation of CD8⁺ T cells.
This parameter, denoted $ln(a_{pem})$, was obtained from fitting the mathematical model to the data of each patient in the training set. It is compared to the estimated values of $ln(a_{pem})$ by a Leave-One-Out cross-validation of the k-NN algorithm. Each point represents the parameter values of one patient and the reference line satisfies equality between the fitted and regression-derived parameter values.

Using all the clinical factors listed in Table 2.5 to train and optimize a classification tree and validating the classification by LOO CV, it was found that the tree, which most correctly classified the values of γ_{mel} was obtained from the data of Breslow tumor thickness and status of nodular melanoma. The comparison between the classified

and fitted values of γ_{mel}, with the use of these two covariates, are summarized in Table 3.4.

Table 3.4. Confusion table for the classification of the tumor growth rate.
The parameter γ_{mel} can obtain two numeric values, namely 0.005 d^{-1} (value 1) or 0.003269 d^{-1} (value 2). Presented in the table are the number of cases in which value 1 of γ_{mel} was fitted, and identified as value 1 by the classification algorithm (true positive; upper-left cell), or value 2 (false negative; lower left cell), and the number of cases in which value 2 of γ_{mel} was fitted, as well as classified as value 2 (true negative; right lower cell), or misclassified as value 1 (false positive; right upper cell). The calculated Cohen's kappa, κ, suggests a fair agreement of predictions to the fitting results.

$\kappa = 0.222$		Fitted value of γ_{mel}	
		Value 1	Value 2
Classification-derived value of γ_{mel}	Value 1	19	13
	Value 2	8	14

Based on the above results, the personalization functions were constructed, estimating the values of a_{pem} and γ_{mel} of each patient in the validation set, from the baseline SOD for a_{pem}, and Breslow tumor thickness, and status of nodular melanoma for γ_{mel} (Table 3.3). The personalization algorithm was completed by implementing in it the personalization functions.

3.3. Prediction of the time to progression by use of the personalization algorithm

The simulation results obtained by the personalization algorithm were compared with the clinically measured tumor sizes in all patients. The goodness of fit of the algorithm-predicted and clinically-measured tumor size was evaluated, as shown in Figure 3.12.

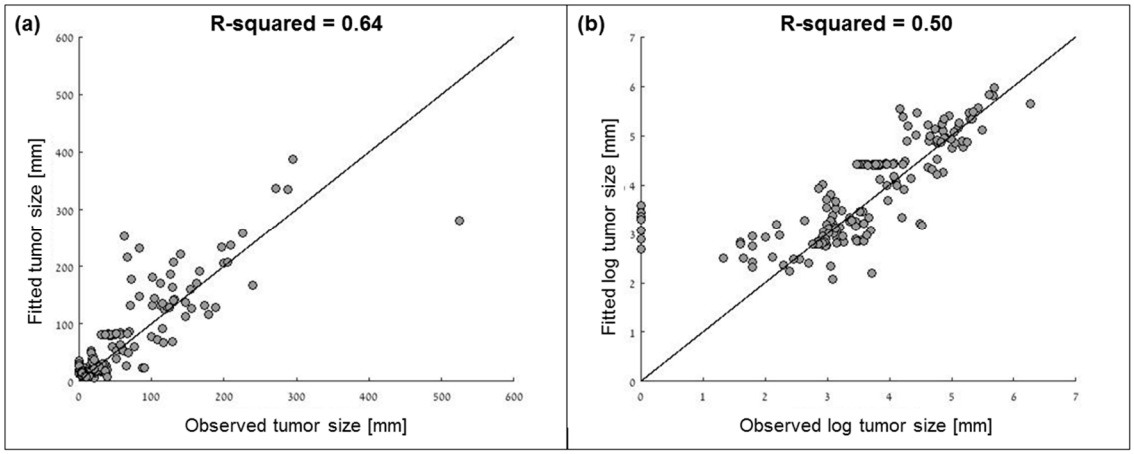

Figure 3.12. Comparison between the Sum of Diameters (SOD), derived by the personalization algorithm, and the value measured from imaging assessments, at each clinically measured time point, and for all patients.
(a) On a normal scale. (b) On a log scale. Values of 0 were excluded from the logarithmic dataset for calculation of R-squared. The reference line marks equality between the fitted and predicted SOD values.

From the predicted tumor size dynamics, the TTP was also predicted, and compared to the value estimated according to the clinically assessed disease progression. Results are shown in Table 3.5. The evaluation of the Cohen's kappa, $\kappa = 0.489$, suggests a moderate agreement between the prediction and clinical data.

Table 3.5. Personal predictions of the time to progression (TTP).
Comparison between the TTP derived from model predictions (pred.) of the personalization algorithm, and the clinically measured (clinic.) TTP. Each cell includes the number of cases (above) and percentage from the total number of patients in the cohort (in brackets below; N = 54), which satisfy one of the six outcomes (see Methods section 2.8). The bold numbers represent the cases, for which the algorithm correctly predicted whether disease progression will occur, and the correct time interval of the TTP. ***Cohen's κ = 0.489****.*

Clinic. TTP / Pred. TTP	0 – 90 days	91 – 150 days	151 – 365 days	No PD during follow-up
0 – 90 days	**6** (11.1 %)	0 (0 %)	2 (3.7 %)	2 (3.7 %)
91 – 150 days	0 (0 %)	**2** (3.7%)	0 (0 %)	3 (5.6 %)
151 – 365 days	0 (0 %)	0 (0 %)	**1** (1.8 %)	0 (0 %)
No PD during follow-up	4 (7.4 %)	2 (3.7 %)	2 (3.7 %)	**30** (55.6 %)

For the patients who had PD according to the personalization algorithm, the predicted TTP was compared to the clinically observed one (Figure 3.13). The results show moderate agreement of the predictions with the clinical observations (R^2=0.505).

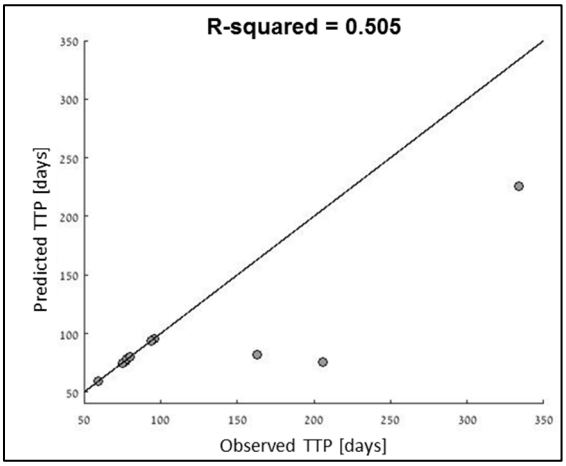

Figure 3.13. Comparison between the predicted TTP and the clinically measured clinical TTP.
The comparison includes only the cases in which disease progression was determined clinically, as well as by the personalization algorithm. Points on the reference line satisfy equality between the observed and computationally derived TTP.

In conclusion, the results of the algorithm development suggest that a mathematical mechanistic model can be applied together with baseline clinical data, to predict response of patients with advanced melanoma to pembro, prior to its administration. To this end, the prediction accuracy of the TTP of individual patients is moderate.

3.4. Conclusions

This section describes the development of a mathematical model for interaction between pembro, melanoma, and the immune system. This model was applied, together with clinical data, for the development of a prediction algorithm for response of patients with advanced melanoma to pembro. Stability analysis of the treatment-free model revealed three PFPs, one is trivial and the other two are non-trivial. Stability of these PFPs depends on the model parameters, such that an increase in the activation rate of $CD8^+$ T cells, and changes in the tumor growth rate, can lead to local stability of the PFP. Biologically, this means tumor control by the immune system. Moreover, a set of parametric conditions for local stability of a PFP was obtained from analysis of the eigenvalues of the Jacobi matrix of the model. This means that if one can identify the model parameters, the possibility of melanoma control by the immune system can be determined. Increase in the function of the immune system can be also induced by pembro. Inclusion of it in the model imposes a similar effect,

as increase in the activation, as well as decrease in the exhaustion rates of $CD8^+$ T cells. Therefore, identification of this effect, as well as the tumor growth rate, can serve for prediction of the tumor dynamic by simulation of the model. In the algorithm, the mathematical model is personalized with the use of clinical data, to predict the TTP of each patient. It was found that the baseline SOD, Breslow tumor thickness, as well as the status of nodular melanoma can serve as markers for personalization of the mathematical model. Based on these markers, the algorithm correctly predicted the time interval of the TTP for 39 out of 54 patients (72%).

4. Discussion

Treatment with ICI has proven successful, as it induces a significant clinical benefit in a subset of patients. However, identification of these patients prior to treatment initiation still remains a challenge and the availability of personal response predictors has been pointed out as an unmet clinical need [121-124]. This thesis was aimed at developing a predictive algorithm to be used by oncologists prior to treatment, for singling out individual patients with advanced melanoma, who would benefit from the immunotherapeutic drug pembro. The algorithm incorporates a new mathematical model, describing the tumor dynamics, as affected by interactions with the immune system of the patient and pembro. The model was personalized by training it using clinical data from patients with advanced melanoma, under treatment with pembro.

In this discussion, the contributions of this thesis towards improving the prediction of disease progression, and response to immunotherapy in melanoma, are summarized, and limitations and further steps for improvement of the outcome prediction are pointed out.

4.1. Insights from the mathematical model on response to pembrolizumab and immune checkpoint inhibitors

The mathematical model presented in this thesis and its analysis within the bio-medically relevant parameter ranges, show that the ratio between activation and exhaustion rates of $CD8^+$ T cells can determine the outcomes of melanoma immunotherapy. Based on the results it is suggested to evaluate $CD8^+$ T cell activation and exhaustion rates in individual patients for improved prediction of their treatment response.

The theoretical and numerical analyses suggest that under realistic assumptions on tumor growth and immune efficacy in an untreated host, the cancer always evades the control of the immune system, and, indeed, spontaneous regression of melanoma is rarely observed [125]. However, the analysis also indicates that if the efficacy of the immune system increases under immunotherapy with ICI, which causes increased

activation or decreased mortality of effector $CD8^+$ T cells, stabilization of the tumor size is possible. Increased activation of effector $CD8^+$ T cells has been clinically observed in response to immunotherapy. For instance, vaccination of patients with melanoma with a LAG-3 antibody resulted in enhanced proliferation of tumor-specific $CD8^+$ T cells in 13 out of 16 patients [126]. Similar findings were made also in Non-Small Cell Lung Cancer, with a proliferative burst of effector $PD\text{-}1^+CD8^+$ T cells observed in 70% of the patients upon treatment with anti-PD-1 [127]. Furthermore, analysis of melanoma biopsies from 46 patients, before and during anti-PD-1 treatment, showed an increase in proliferation of intra-tumor $PD\text{-}1^+CD8^+$ T cells following treatment [128]. Association of therapy outcomes with ICI-caused $CD8^+$ T cell proliferation was examined in the clinical setting, observing enhanced and early proliferation mostly among responders [114, 127, 128]. However, samples from some responders did not show increased proliferation of $CD8^+$ T cells. Clearly, then, it is not sufficient to measure only the activation rate of $CD8^+$ T cells for accurately predicting the ICI outcomes. Integrating the impact of $CD8^+$ T cells on the tumor size in mathematical models, which consider the intricate dynamics affecting the response, can better serve for individualization of response prediction.

The model analysis indicates that extended periods of disease stability can result from increased activation of immune cells, while oscillatory tumor growth is induced by reduced exhaustion of the immune cells, for example, due to immunotherapy. From this finding it is inferred that immunotherapy by ICI could yield different patterns of change in the disease burden. The amplitude of the modelled oscillations is in the order of 10^6 cells. Considering that a tumor lesion with 1 cm diameter comprises about 10^9 cells [129], and that a lesion is confidently measurable if its diameter is at least 1 cm [113], the oscillations are likely averaged out in clinical size assessments. However, small oscillations in the population size of tumor and immune cells have been previously reported. For example, Coventry et al. [130] measured CRP levels in patients with melanoma and other cancer indications, and for most cases reported oscillatory patterns, with periodicity of 6-7 days. These oscillations were linked to changes in the disease intensity and strength of inflammatory signatures. According to their rationale, tumor cells induce infection, which leads to a deficit of T cells, and

increased proliferation of effector T cells. The effector cells in turn eliminate tumor cells. Other tumor cells proliferate rapidly, thereby driving the feedback between immune cells and cancer cells. Of note, similar feedback was discussed by d'Onforio et al. [131], who applied a family of mathematical models to analyze tumor-immune interactions. In their study, d'Onforio et al. analyzed the effect of time delays between the tumor size at a given moment and its effect on the stimulation of immune effector cells. They show that exponentially distributed time delays can induce sustained oscillations in the number of cells. Correspondingly, the oscillation observed in this study can be explained by an exponentially distributed time lag between the tumor-induced stimulation term in Equation (1a), namely $\alpha_A \cdot \frac{M}{M+b}$, and oscillations in the number of functional APCs, $A(t)$.

Stability analysis of the model emphasizes the effect of tumor growth rate and baseline tumor burden on the success of immunotherapy. Tumor shrinkage is possible only if the initial number of tumor cells and the initial number of immune cells are located within the basin of attraction of the lower PFP. For patients with a significantly larger initial tumor burden, a larger effect of the ICI is required to induce tumor shrinkage. From a mathematical point of view, as the immune efficacy increases, the ratio between the efficacy of the immune response and the tumor growth rate increases, which, as shown in Figure 3.2, leads to a larger difference between both FPs, and thus a larger basin of attraction of the stable FP. These results imply that patients with initially small tumor burden should benefit more from this therapy, supporting reports that high tumor burden is associated with poorer outcome to ICI [70, 132, 133]. The results point to a need to clinically test the effect of adjuvant therapy with ICI. The reduction of tumor load prior to treatment by ICI, either by resection or by radiation, is believed to augment the clinical benefit of ICI-based therapy. Interestingly, the benefit of immunotherapy and resection combination, but in an inverse sequence to the one suggested here, was clinically shown in a study reporting that administration of pembro as an adjuvant therapy for patients with completely resected high-risk stage III melanoma increased the recurrence-free survival of treated patients, as compared to patients who received placebo [134]. Confirming the model findings on the relation between immune cell activity and initial

tumor load, it was shown that the ratio between immune activation and baseline tumor burden can be associated with enhanced functionality of $CD8^+$ T cells and response to ICI in patients with advanced melanoma [114]. In [114], Huang and colleagues checked a combined emergent parameter - the ratio between the reinvigoration rate of $CD8^+$ T cells (as measured by the percentage of $CD8^+$ T cells expressing Ki67), and the tumor burden at baseline. They correlated this ratio with the observed clinical response of patients to pembro. Their conclusion is that the combined ratio can better distinguish clinical outcomes and predict response than each one of these parameters taken alone, and that this ratio can serve as a calibrated parameter, predicting response to PD-1 blockade.

4.1.1. The reasoning behind a simplified mechanistic model in purpose of outcome prediction

To facilitate the mathematical analyses, the model was deliberately kept simple, taking into account only the main effects of pembro on $CD8^+$ T cells and the melanoma tumor. In particular, the effects of treatment were modeled by assigning bigger or smaller values to the activation rate of $CD8^+$ T cells, α_e, and to their elimination rate, μ_e. The immune system, as well as the consequences of ICI-based therapy, are obviously far more complex. For example, the mechanism of action of pembro includes effects on interactions with additional cell populations, such as myeloid-derived suppressor cells (MDSCs), NK cells, and helper $CD4^+$ T cells [33]. Similarly to $CD8^+$ T cells, NK cells have a cytotoxic effect on tumor cells. Since they express PD-1, treatment with pembro may increase the abundance of functional NK cells, and thereby also contribute to the tumor growth control [135]. Moreover, cytometric analysis of blood samples from patients with advanced melanoma under pembro and nivolumab show that the anti-PD-1 treatment reduces the frequency of circulating MDSCs, and increases the frequency of circulating NK cells among responders [136]. Such additional processes can be considered for inclusion in the model in future extensions.

4.1.2. Summary and future perspective

In summary, this work provides new insight into the interactions between the immune system and melanoma, enabling a better understanding of the potential outcomes of individual patients with metastatic melanoma under ICI treatment. Analysis of the mechanistic model showed that while the natural immunity is not sufficient to control the growth of melanoma tumors in the absence of treatment, administration of ICIs increases the elimination of tumor cells by $CD8^+$ T cells. The resulting response to ICI can turn the uncontrollable tumor growth into shrinkage or stabilization, depending on the individual patient characteristics. This can provide a basis for future studies in which model-based predictors for response to ICI treatment could be developed to address the need for improved and personalized prognosis in melanoma.

4.2. The predictive power of the personalization algorithm

To this end, the personalization algorithm developed and described in this thesis can serve as a virtual response predictor, along with clinical information about the baseline tumor size, Breslow tumor thickness, and status of nodular melanoma. Taking into account the low life expectancy of untreated patients with advanced melanoma, and the involved side effects and high therapy costs [137], the ability to select patients for these treatments can significantly improve the quality of life of the patients.

One of the major goals in medical biomathematics is to propose algorithms that can be of aid in the medical practice. Specifically, there are two significant challenges to mathematical models of cancer growth, which become clinically useful. First is that the necessary input information cannot be extracted in a straightforward manner from data that are routinely collected in the clinics. Second is that in most cases, the output information is not instructive for the physician's decision-making process. Wishing to overcome these hardships, the algorithm was developed and tested using data that are routinely collected in the clinics, namely, SOD, as prescribed by the RECIST 1.1. To increase the physical and mechanistic realism of the description of tumor growth, it would have been preferred that radiologists would measure, with little additional effort, the total tumor volume. But the current standards in the field involve longitudinal measurement of SOD. As the goal of this work commands, the

developed tools should be adjusted to the reality in the field, rather than develop an idealized solution.

4.2.1. Contribution of the algorithm development to the currently-available techniques and biomarkers for response evaluation

The personalization algorithm enables personalized predictions of the period in which disease progression will occur, as defined by RECIST 1.1. Nowadays, the first response assessment in the clinic takes place at around three months into the treatment. As many patients progress within these first three months [133, 138, 139], the algorithm predicting the TTP prior to treatment can save several months of administration of an incompatible and expensive drug. For patients who benefit from the treatment, the algorithm provides information on the duration of the response. Even though the discretization policy of the TTP entails loss of information, this approach is inevitable. The treating oncologists do not evaluate the patient's disease progression status continuously, but rather, every 2-4 months, using imaging technology (CT/MRI). As stated above, the goal of this work was to generate clinically relevant output. For that it would be sufficient to coincide the prediction of disease progression with the time of its effective substantiation by imaging. For this reason, the resolution of TTP predictions is as coarse as the planned CT/MRI scanning schedule. Still, it would be of a significant help to the doctor to know whether the patient is expected to progress early, or will have moderately long TTP, or a very long TTP, as evaluated by RECIST1.1. The discrete categories of TTP used in this study roughly correspond to these possibilities of response duration.

Prediction of the type and duration of response is a unique addition of this study to the knowledge gained from previously developed biomarkers for ICI. As summarized by [140], several markers in the tumor microenvironment and peripheral blood are associated with response to ICI in patients with malignant melanoma. However, as yet, there is no way to quantify the relationships between the biomarker levels and the expected response. For example, elevation of the baseline LDH level is associated with shorter overall survival (OS) of patients with malignant melanoma under anti-PD-1 treatments [141]. Therefore, the baseline LDH level can possibly serve for patients' stratification, but the survival time of each patient cannot be predicted by this marker.

In this study, clinical disease progression was observed in all patients (11 out of 29, 38%), who had an elevated LDH level before treatment onset and more than 10% increase of the LDH level on the first CT scan. In contrast, disease progression occurred in only 4 out of 18 patients who initially had elevated LDH levels, but less than 10% LDH change from baseline on the first CT scan. Therefore, the change from baseline of LDH levels can serve to predict disease progression within the first year of ICI initiation, but for many patients, the prediction does not precede much the detection of progression by imaging scans. Another study reports that an increase in tumor burden of less than 20% from baseline during three months into treatment with pembro, is associated with longer OS of patients with advanced melanoma [142]. However, it may be problematic to use early increase in tumor load as a response predictor, as it can be detected only after initiation of the treatment, when many patients may have already experienced disease progression. The ability to predict ICI treatment outcomes at baseline by use of the suggested personalization algorithm can complete the currently available methodology for response evaluation during the treatment, by assessment of imaging data and other biomarkers for patients' stratification.

The results show that Breslow tumor thickness, status of nodular melanoma and baseline tumor burden can serve as markers for TTP prediction under pembro, when integrated and processed by the personalization algorithm, which implements the mechanistic model. It was found that different values of Breslow tumor thickness and status of nodular melanoma are associated with different rates of tumor growth. Breslow tumor thickness has been known as a prognostic biomarker for melanoma [143, 144], and here it is shown that it has a predictive power. Using the baseline tumor burden as a potential biomarker is supported by Joseph et al. [145], who analyzed the relationships between baseline tumor burden and overall survival of 583 patients with advanced melanoma under pembro. In addition, Huang et al. [114] analyzed peripheral blood from patients with advanced melanoma, and found that response to pembro is associated with the ratio between the baseline tumor burden and restored activation of $CD8^+$ T cells.

4.2.2. Limiting factors of outcome prediction by the personalization algorithm

Using a small patient cohort (54 patients) for its training, the personalization algorithm yields moderately accurate predictions. It is believed that by increasing the size of the training set, the performance of the regression and classification, used for identification of the individual model parameters, will be significantly improved. Yet, considering the limited clinical information and the simple mathematical model implemented at the core of the algorithm, the results are encouraging. Notably, it is believed that model simplicity is a prerequisite for generating a successful algorithm, since it requires evaluation of only a small number of personal parameters. In contrast, a more complex model would entail the evaluation of a relatively large number of clinical measurements in the patient, in order to determine the personal models. It should be stressed that, *a priori*, the evaluation of disease progression was not required to be more sensitive than that of RECIST 1.1, which takes into account only significant changes in the tumor load. Such a simple model is well suited for the estimation of similarly rough changes in disease progression.

Another limitation of the personalization algorithm developed here is that it uses the RECIST 1.1 criteria, one of which being the appearance of new lesions. However, this option was not evaluated in the algorithm and disease progression was determined only by the change in size of the target lesions between consecutive imaging scans. Inspecting the clinical patient data, it was noted that in about 50% of those in whom new lesions were detected, treatment with pembro was continued after detection, practically implying that often clinicians do not consider the new lesion criterion as PD. This finding is in line with the recent understanding that formation of new lesions under immunotherapy does not necessarily indicate actual PD [146, 147]. Accordingly, in the recently developed immune-related RECIST (irRECIST) criteria, pertinent to immunotherapy, appearance of new lesions is not a criterion for PD [142]. The indicated response is then “unconfirmed PD”, and validation is required in another imaging scan, at least 4 weeks later. Adaptation of the algorithm to the irRECIST criteria will be made upon clinical validation of these criteria as part of the clinical follow-up routine.

4.2.3. Transferring the personalization algorithm into a clinical device

Future recommendations for improving the predictive power of the personalization algorithm include training by a larger dataset, as well as validation of the algorithm by clinical data from an independent dataset. Following improvements in the accuracy, the algorithm can be used as a tool in personal treatment selection. In addition, this innovative methodology can be adapted to other available immunotherapies, including anti-CTLA-4 and its combination with anti-PD-1. In summary, this study demonstrates that using computational algorithms for prediction of response to immunotherapy in patients with metastatic melanoma is feasible.

5. Overall Conclusion

In 1992, the Israeli singer and songwriter Shalom Hanoch wrote in his song “Mevia hakol”:

“If I could only give you solutions, all that’s possible would have been here long ago…”

-Shalom Hanoch

He dedicated the song to his close friend- the actress Talia Shapira, who died of cancer. By that he raised the awareness of the constant searching for possible and good solutions to battle cancer in our society.

The new mathematical model presented in this work and its theoretical analysis imply that increase in the functionality of $CD8^+$ T cells, as well as a low tumor growth rate can induce tumor stabilization. This can induce disease control by the immune system. Considering that an increase in the functionality of $CD8^+$ T cells is possible by treatment with pembro, the mathematical mechanistic model can serve as a powerful tool for simulation of the tumor dynamic. Thereby, this thesis suggests that personalization of a mathematical mechanistic model by various clinical and molecular pretreatment measurements, can serve for predicting of the individual TTP. Using the here-developed algorithm to predict the TTP prior to treatment could guide the physicians in the process of decision-making, save several months of administration of an incompatible treatment, and significantly improve the quality of life of the patients. Following validation by a new dataset of pembro-treated patients with advanced melanoma, this algorithm could serve as a tool for treatment selection in pembro-treated patients. In the future, the algorithm can be adapted to other available therapies, by adjustment of the mathematical mechanistic model to describe interaction between the host, the disease, and the treatment, and by using pertinent clinical data. The resulting algorithm can serve as a tool for selection of the most beneficial treatment out of the clinically available options.

6. References

1. Abraham, C. and R. Medzhitov, *Interactions between the host innate immune system and microbes in inflammatory bowel disease.* Gastroenterology, 2011. **140**(6): p. 1729-1737.
2. Sperandio, B., N. Fischer, and P.J. Sansonetti. *Mucosal physical and chemical innate barriers: Lessons from microbial evasion strategies*. in *Seminars in immunology*. 2015. Elsevier.
3. Elias, P.M. *The skin barrier as an innate immune element*. in *Seminars in immunopathology*. 2007. Springer.
4. Ganz, T., *Epithelia: not just physical barriers.* Proceedings of the National Academy of Sciences, 2002. **99**(6): p. 3357-3358.
5. JANEWAY Jr, C., *Immunobiology.* The Immune System in Health and Disease, 2001: p. 35-91.
6. Casadevall, A. and L.-a. Pirofski, *A new synthesis for antibody-mediated immunity.* Nature immunology, 2012. **13**(1): p. 21.
7. Shishido, S.N., et al., *Humoral innate immune response and disease.* Clinical immunology, 2012. **144**(2): p. 142-158.
8. Ehrnthaller, C., et al., *New insights of an old defense system: structure, function, and clinical relevance of the complement system.* Molecular medicine, 2011. **17**(3): p. 317.
9. Du Clos, T.W. and C. Mold, *C-reactive protein.* Immunologic research, 2004. **30**(3): p. 261-277.
10. Burnet, S.F.M., *The clonal selection theory of acquired immunity.* 1959.
11. Roquiz, W., S. Al Diffalha, and A.R. Kini, *Leukocyte Development, Kinetics, and Functions.* Rodak's Hematology: Clinical Principles and Applications, 2015: p. 149.
12. Villani, A.-C., et al., *Single-cell RNA-seq reveals new types of human blood dendritic cells, monocytes, and progenitors.* Science, 2017. **356**(6335): p. eaah4573.
13. Italiani, P. and D. Boraschi, *From monocytes to M1/M2 macrophages: phenotypical vs. functional differentiation.* Frontiers in immunology, 2014. **5**: p. 514.
14. Oczypok, E.A., T.D. Oury, and C.T. Chu, *It'sa cell-eat-cell world: autophagy and phagocytosis.* The American journal of pathology, 2013. **182**(3): p. 612-622.
15. Mantovani, A., et al., *Cancer-related inflammation.* Nature, 2008. **454**(7203): p. 436.
16. Mantovani, A., et al., *Macrophage polarization: tumor-associated macrophages as a paradigm for polarized M2 mononuclear phagocytes.* Trends in immunology, 2002. **23**(11): p. 549-555.
17. Mantovani, A., et al., *Tumor-associated macrophages and the related myeloid-derived suppressor cells as a paradigm of the diversity of macrophage activation.* Human immunology, 2009. **70**(5): p. 325-330.
18. Mellman, I., *Dendritic cells: master regulators of the immune response.* Cancer immunology research, 2013. **1**(3): p. 145-149.

19. Bosisio, D., et al., *Dendritic cells in inflammatory angiogenesis and lymphangiogenesis.* Current opinion in immunology, 2018. **53**: p. 180-186.
20. Welch, D.R., et al., *Tumor-elicited polymorphonuclear cells, in contrast to" normal" circulating polymorphonuclear cells, stimulate invasive and metastatic potentials of rat mammary adenocarcinoma cells.* Proceedings of the National Academy of Sciences, 1989. **86**(15): p. 5859-5863.
21. Coffelt, S.B., M.D. Wellenstein, and K.E. de Visser, *Neutrophils in cancer: neutral no more.* Nature Reviews Cancer, 2016. **16**(7): p. 431.
22. Fridlender, Z.G., et al., *Polarization of tumor-associated neutrophil phenotype by TGF-β:"N1" versus "N2" TAN.* Cancer cell, 2009. **16**(3): p. 183-194.
23. Davis, B.P. and M.E. Rothenberg, *Eosinophils and cancer.* Cancer immunology research, 2014. **2**(1): p. 1-8.
24. Wedemeyer, J., M. Tsai, and S.J. Galli, *Roles of mast cells and basophils in innate and acquired immunity.* Current opinion in immunology, 2000. **12**(6): p. 624-631.
25. Sektioglu, I.M., et al., *Basophils promote tumor rejection via chemotaxis and infiltration of CD8+ T cells.* Cancer research, 2017. **77**(2): p. 291-302.
26. Blumenreich, M.S., *The white blood cell and differential count*, in *Clinical Methods: The History, Physical, and Laboratory Examinations. 3rd edition*. 1990, Butterworths.
27. Caligiuri, M.A., *Human natural killer cells.* Blood, 2008. **112**(3): p. 461-469.
28. Crouse, J., et al., *NK cells regulating T cell responses: mechanisms and outcome.* Trends in immunology, 2015. **36**(1): p. 49-58.
29. Waldhauer, I. and A. Steinle, *NK cells and cancer immunosurveillance.* Oncogene, 2008. **27**(45): p. 5932.
30. Tseng, S.-Y., et al., *T cell-dendritic cell immunological synapses contain TCR-dependent CD28-CD80 clusters that recruit protein kinase Cθ.* The Journal of Immunology, 2008. **181**(7): p. 4852-4863.
31. Dustin, M.L. and C.T. Baldari, *The immune synapse: past, present, and future*, in *The Immune Synapse*. 2017, Springer. p. 1-5.
32. Jenkins, M.R. and G.M. Griffiths, *The synapse and cytolytic machinery of cytotoxic T cells.* Current opinion in immunology, 2010. **22**(3): p. 308-313.
33. Nguyen, L.T. and P.S. Ohashi, *Clinical blockade of PD1 and LAG3 [mdash] potential mechanisms of action.* Nature Reviews Immunology, 2015. **15**(1): p. 45-56.
34. Marin-Acevedo, J.A., et al., *Next generation of immune checkpoint therapy in cancer: new developments and challenges.* Journal of hematology & oncology, 2018. **11**(1): p. 39.
35. Jago, C., et al., *Differential expression of CTLA-4 among T cell subsets.* Clinical & Experimental Immunology, 2004. **136**(3): p. 463-471.
36. Walker, L.S. and D.M. Sansom, *The emerging role of CTLA4 as a cell-extrinsic regulator of T cell responses.* Nature reviews Immunology, 2011. **11**(12): p. 852-863.
37. Ott, P.A., F.S. Hodi, and C. Robert, *CTLA-4 and PD-1/PD-L1 blockade: new immunotherapeutic modalities with durable clinical benefit in melanoma patients.* Clinical Cancer Research, 2013. **19**(19): p. 5300-5309.

38. Sugamura, K., N. Ishii, and A.D. Weinberg, *Therapeutic targeting of the effector T-cell co-stimulatory molecule OX40.* Nature Reviews Immunology, 2004. **4**(6): p. 420-431.
39. Pardoll, D.M., *The blockade of immune checkpoints in cancer immunotherapy.* Nature Reviews Cancer, 2012. **12**(4): p. 252-264.
40. Walker, L.S. and D.M. Sansom, *Confusing signals: Recent progress in CTLA-4 biology.* Trends in immunology, 2015. **36**(2): p. 63-70.
41. Keir, M.E., et al., *PD-1 and its ligands in tolerance and immunity.* Annu. Rev. Immunol., 2008. **26**: p. 677-704.
42. Buchbinder, E.I. and A. Desai, *CTLA-4 and PD-1 pathways: similarities, differences, and implications of their inhibition.* American journal of clinical oncology, 2016. **39**(1): p. 98.
43. Sharpe, A.H. and K.E. Pauken, *The diverse functions of the PD1 inhibitory pathway.* Nature Reviews Immunology, 2018. **18**(3): p. 153.
44. Muñoz-Unceta, N., et al., *Durvalumab in NSCLC: latest evidence and clinical potential.* Therapeutic advances in medical oncology, 2018. **10**: p. 1758835918804151.
45. Sallusto, F., J. Geginat, and A. Lanzavecchia, *Central memory and effector memory T cell subsets: function, generation, and maintenance.* Annu. Rev. Immunol., 2004. **22**: p. 745-763.
46. Arnold, M., et al., *Global burden of cutaneous melanoma attributable to ultraviolet radiation in 2012.* International journal of cancer, 2018. **143**(6): p. 1305-1314.
47. Blankenstein, T., et al., *The determinants of tumour immunogenicity.* Nature Reviews Cancer, 2012. **12**(4): p. 307.
48. Schumacher, T.N. and R.D. Schreiber, *Neoantigens in cancer immunotherapy.* Science, 2015. **348**(6230): p. 69-74.
49. Friedman, R.J., D.S. Rigel, and A.W. Kopf, *Early detection of malignant melanoma: The role of physician examination and self-examination of the skin.* CA: a cancer journal for clinicians, 1985. **35**(3): p. 130-151.
50. Terushkin, V. and A.C. Halpern, *Melanoma early detection.* Hematology/Oncology Clinics, 2009. **23**(3): p. 481-500.
51. Lo, J.A. and D.E. Fisher, *The melanoma revolution: From UV carcinogenesis to a new era in therapeutics.* Science, 2014. **346**(6212): p. 945-949.
52. Miller, A.J. and M.C. Mihm Jr, *Melanoma.* New England Journal of Medicine, 2006. **355**(1): p. 51-65.
53. Clark, W.H., et al., *A study of tumor progression: the precursor lesions of superficial spreading and nodular melanoma.* Human pathology, 1984. **15**(12): p. 1147-1165.
54. Chudnovsky, Y., P.A. Khavari, and A.E. Adams, *Melanoma genetics and the development of rational therapeutics.* Journal of clinical Investigation, 2005. **115**(4): p. 813.
55. Mackie, R., T. Freudenberger, and T. Aitchison, *Personal risk-factor chart for cutaneous melanoma.* The Lancet, 1989. **334**(8661): p. 487-490.
56. Kraemer, K.H. and J.J. DiGiovanna, *Xeroderma pigmentosum*, in *GeneReviews®[Internet]*. 2016, University of Washington, Seattle.

57. Soura, E., et al., *Hereditary melanoma: Update on syndromes and management: Genetics of familial atypical multiple mole melanoma syndrome.* Journal of the American Academy of Dermatology, 2016. **74**(3): p. 395-407.
58. Gershenwald, J.E. and R.A. Scolyer, *Melanoma staging: American Joint committee on cancer (AJCC) and beyond.* Annals of surgical oncology, 2018. **25**(8): p. 2105-2110.
59. AlAsadi, A.H.H. and B.M.R. AL-Safy, *Early detection and classification of melanoma skin cancer*. 2016: LAP LAMBERT Academic Publishing.
60. Kaliki, S. and C. Shields, *Uveal melanoma: relatively rare but deadly cancer.* Eye, 2017. **31**(2): p. 241.
61. Tacastacas, J.D., et al., *Update on primary mucosal melanoma.* Journal of the American Academy of Dermatology, 2014. **71**(2): p. 366-375.
62. Schadendorf, D., et al., *Melanoma.* The Lancet, 2018. **392**(10151): p. 971-984.
63. Prieto, P.A., et al., *CTLA-4 blockade with ipilimumab: long-term follow-up of 177 patients with metastatic melanoma.* Clinical Cancer Research, 2012. **18**(7): p. 2039-2047.
64. Hodi, F.S., et al., *Improved survival with ipilimumab in patients with metastatic melanoma.* New England Journal of Medicine, 2010. **363**(8): p. 711-723.
65. Wolchok, J.D., et al., *Ipilimumab monotherapy in patients with pretreated advanced melanoma: a randomised, double-blind, multicentre, phase 2, dose-ranging study.* The lancet oncology, 2010. **11**(2): p. 155-164.
66. Robert, C., et al., *Pembrolizumab versus ipilimumab in advanced melanoma.* New England Journal of Medicine, 2015.
67. Schachter, J., et al., *Pembrolizumab versus ipilimumab for advanced melanoma: final overall survival results of a multicentre, randomised, open-label phase 3 study (KEYNOTE-006).* The Lancet, 2017. **390**(10105): p. 1853-1862.
68. Larkin, J., et al., *Combined nivolumab and ipilimumab or monotherapy in untreated melanoma.* New England Journal of Medicine, 2015. **373**(1): p. 23-34.
69. Wolchok, J.D., et al., *Overall survival with combined nivolumab and ipilimumab in advanced melanoma.* New England Journal of Medicine, 2017. **377**(14): p. 1345-1356.
70. Robert, C., et al., *Durable Complete Response After Discontinuation of Pembrolizumab in Patients With Metastatic Melanoma.* Journal of Clinical Oncology, 2017: p. JCO. 2017.75. 6270.
71. Wang, W., et al., *Biomarkers on melanoma patient T cells associated with ipilimumab treatment.* J Transl Med, 2012. **10**(1): p. 146-146.
72. Weide, B., et al., *Baseline biomarkers for outcome of melanoma patients treated with pembrolizumab.* Clinical Cancer Research, 2016: p. clincanres. 0127.2016.
73. Fusi, A., et al., *PD-L1 expression as a potential predictive biomarker.* The Lancet Oncology, 2015. **16**(13): p. 1285-1287.
74. Vilain, R.E., et al., *Dynamic changes in PD-L1 expression and immune infiltrates early during treatment predict response to PD-1 blockade in melanoma.* Clinical Cancer Research, 2017. **23**(17): p. 5024-5033.

75. Zou, W., J.D. Wolchok, and L. Chen, *PD-L1 (B7-H1) and PD-1 pathway blockade for cancer therapy: Mechanisms, response biomarkers, and combinations.* Science translational medicine, 2016. **8**(328): p. 328rv4-328rv4.
76. Sunshine, J. and J.M. Taube, *PD-1/PD-L1 inhibitors.* Current opinion in pharmacology, 2015. **23**: p. 32-38.
77. Nosrati, A., et al., *Evaluation of clinicopathological factors in PD-1 response: derivation and validation of a prediction scale for response to PD-1 monotherapy.* British journal of cancer, 2017. **116**(9): p. 1141.
78. Dronca, R.S., et al., *T cell Bim levels reflect responses to anti–PD-1 cancer therapy.* JCI insight, 2016. **1**(6).
79. Chen, P.-L., et al., *Analysis of immune signatures in longitudinal tumor samples yields insight into biomarkers of response and mechanisms of resistance to immune checkpoint blockade.* Cancer Discovery, 2016. **6**(8): p. 827-837.
80. Jacquelot, N., et al., *Predictors of responses to immune checkpoint blockade in advanced melanoma.* Nature communications, 2017. **8**(1): p. 592.
81. Adam, J. and N. Bellomo, *A survey of models for tumor-immune system dynamics*. 2012: Springer Science & Business Media.
82. Agur, Z., et al., *Employing dynamical computational models for personalizing cancer immunotherapy.* Expert Opinion on Biological Therapy, 2016. **16**(11): p. 1373-1385.
83. d'Onofrio, A., *A general framework for modeling tumor-immune system competition and immunotherapy: Mathematical analysis and biomedical inferences.* Physica D: Nonlinear Phenomena, 2005. **208**(3-4): p. 220-235.
84. d'Onofrio, A., *Metamodeling tumor–immune system interaction, tumor evasion and immunotherapy.* Mathematical and Computer Modelling, 2008. **47**(5): p. 614-637.
85. Eftimie, R., J.J. Gillard, and D.A. Cantrell, *Mathematical Models for Immunology: Current State of the Art and Future Research Directions.* Bulletin of Mathematical Biology, 2016. **78**(10): p. 2091-2134.
86. Eladdadi, A. and A. Radunskaya, *Modeling cancer-immune responses to therapy.* Journal of pharmacokinetics and pharmacodynamics, 2014. **41**(5): p. 461-478.
87. Foryś, U., M. Bodnar, and Y. Kogan, *Asymptotic dynamics of some t-periodic one-dimensional model with application to prostate cancer immunotherapy.* Journal of mathematical biology, 2016. **73**(4): p. 867-883.
88. Kogan, Y., et al., *Reconsidering the paradigm of cancer immunotherapy by computationally aided real-time personalization.* Cancer research, 2012. **72**(9): p. 2218-2227.
89. Kronik, N., et al., *Predicting outcomes of prostate cancer immunotherapy by personalized mathematical models.* PLoS One, 2010. **5**(12): p. e15482.
90. Elishmereni, M., et al., *Predicting time to castration resistance in hormone sensitive prostate cancer by a personalization algorithm based on a mechanistic model integrating patient data.* The Prostate, 2016. **76**(1): p. 48-57.
91. Chen, L., et al., *Tumor immunogenicity determines the effect of B7 costimulation on T cell-mediated tumor immunity.* The Journal of experimental medicine, 1994. **179**(2): p. 523-532.

92. Rizvi, N.A., et al., *Mutational landscape determines sensitivity to PD-1 blockade in non–small cell lung cancer.* Science, 2015. **348**(6230): p. 124-128.
93. Snyder, A., et al., *Genetic basis for clinical response to CTLA-4 blockade in melanoma.* New England Journal of Medicine, 2014. **371**(23): p. 2189-2199.
94. Dustin, M.L., *The immunological synapse.* Arthritis Res, 2002. **4**(Suppl 3): p. S119-125.
95. Dustin, M.L., *The Immunological Synapse.* Cancer immunology research, 2014. **2**(11): p. 1023-1033.
96. Cipponi, A., et al., *Tumor-infiltrating lymphocytes: apparently good for melanoma patients. But why?* Cancer Immunology, Immunotherapy, 2011. **60**(8): p. 1153-1160.
97. Barrio, M.M., et al., *Human macrophages and dendritic cells can equally present MART-1 antigen to CD8+ T cells after phagocytosis of gamma-irradiated melanoma cells.* PloS one, 2012. **7**(7): p. e40311.
98. Von Euw, E.M., et al., *Monocyte-derived dendritic cells loaded with a mixture of apoptotic/necrotic melanoma cells efficiently cross-present gp100 and MART-1 antigens to specific CD8+ T lymphocytes.* Journal of translational medicine, 2007. **5**(1): p. 19.
99. Lee, T.-H., Y.-H. Cho, and M.-G. Lee, *Larger numbers of immature dendritic cells augment an anti-tumor effect against established murine melanoma cells.* Biotechnology letters, 2007. **29**(3): p. 351-357.
100. de Pillis, L., A. Gallegos, and A. Radunskaya, *A model of dendritic cell therapy for melanoma.* Frontiers in oncology, 2013. **3**.
101. Ludewig, B., et al., *Determining control parameters for dendritic cell-cytotoxic T lymphocyte interaction.* European journal of immunology, 2004. **34**(9): p. 2407-2418.
102. Bossi, G., et al., *Examining the presentation of tumor-associated antigens on peptide-pulsed T2 cells.* Oncoimmunology, 2013. **2**(11): p. e26840.
103. Taylor, G.P., et al., *Effect of lamivudine on human T-cell leukemia virus type 1 (HTLV-1) DNA copy number, T-cell phenotype, and anti-tax cytotoxic T-cell frequency in patients with HTLV-1-associated myelopathy.* Journal of virology, 1999. **73**(12): p. 10289-10295.
104. Carlson, J.A., *Tumor doubling time of cutaneous melanoma and its metastasis.* The American journal of dermatopathology, 2003. **25**(4): p. 291-299.
105. Joseph, W.L., D.L. Morton, and P.C. Adkins, *Variation in tumor doubling time in patients with pulmonary metastatic disease.* Journal of surgical oncology, 1971. **3**(2): p. 143-149.
106. Kuznetsov, V., *A mathematical model for the interaction between cytotoxic T lymphocytes and tumour cells. Analysis of the growth, stabilization, and regression of a B-cell lymphoma in mice chimeric with respect to the major histocompatibility complex.* Biomedical science, 1990. **2**(5): p. 465-476.
107. Kuznetsov, V., V. Zhivoglyadov, and L. Stepanova, *Kinetic approach and estimation of the parameters of cellular interaction between the immunity system and a tumor.* Archivum immunologiae et therapiae experimentalis, 1992. **41**(1): p. 21-31.

108. Kuznetsov, V.A., et al., *Nonlinear dynamics of immunogenic tumors: parameter estimation and global bifurcation analysis.* Bulletin of mathematical biology, 1994. **56**(2): p. 295-321.
109. Kronik, N., et al., *Improving alloreactive CTL immunotherapy for malignant gliomas using a simulation model of their interactive dynamics.* Cancer Immunology, Immunotherapy, 2008. **57**(3): p. 425-439.
110. de Vries, I.J.M., et al., *Effective migration of antigen-pulsed dendritic cells to lymph nodes in melanoma patients is determined by their maturation state.* Cancer research, 2003. **63**(1): p. 12-17.
111. de Vries, I.J.M., et al., *Magnetic resonance tracking of dendritic cells in melanoma patients for monitoring of cellular therapy.* Nature biotechnology, 2005. **23**(11): p. 1407-1413.
112. Kamath, A.T., et al., *The development, maturation, and turnover rate of mouse spleen dendritic cell populations.* The Journal of Immunology, 2000. **165**(12): p. 6762-6770.
113. Eisenhauer, E., et al., *New response evaluation criteria in solid tumours: revised RECIST guideline (version 1.1).* European journal of cancer, 2009. **45**(2): p. 228-247.
114. Huang, A.C., et al., *T-cell invigoration to tumour burden ratio associated with anti-PD-1 response.* Nature, 2017.
115. Warrens, M.J., *A comparison of Cohen's kappa and agreement coefficients by Corrado Gini.* International Journal, 2013. **16**: p. 7.
116. Hassard, B.D., N.D. Kazarinoff, and Y.-H. Wan, *Theory and applications of Hopf bifurcation*. Vol. 41. 1981: CUP Archive.
117. Brauer, F. and J.A. Nohel, *The qualitative theory of ordinary differential equations: an introduction*. 2012: Courier Corporation.
118. Yang, X., *Generalized form of Hurwitz-Routh criterion and Hopf bifurcation of higher order.* Applied mathematics letters, 2002. **15**(5): p. 615-621.
119. Liu, W.-m., *Criterion of Hopf bifurcations without using eigenvalues.* Journal of Mathematical Analysis and Applications, 1994. **182**(1): p. 250-256.
120. Douskos, C. and P. Markellos, *Complete Coefficient Criteria for Five-Dimensional Hopf Bifurcations, with an Application to Economic Dynamics.* Journal of Nonlinear Dynamics, 2015. **2015**.
121. Fujii, T., et al., *Biomarkers of response to immune checkpoint blockade in cancer treatment.* Critical reviews in oncology/hematology, 2018.
122. Sharma, P. and J.P. Allison, *The future of immune checkpoint therapy.* Science, 2015. **348**(6230): p. 56-61.
123. Garrido, M.J., P. Berraondo, and I.F. Trocóniz, *Commentary on Pharmacometrics for Immunotherapy.* CPT: Pharmacometrics & Systems Pharmacology, 2016.
124. Nishino, M., et al., *Monitoring immune-checkpoint blockade: response evaluation and biomarker development.* Nature reviews Clinical oncology, 2017. **14**(11): p. 655.
125. Everson, T.C., *Spontaneous regression of cancer.* Annals of the New York Academy of sciences, 1964. **114**(2): p. 721-735.
126. Legat, A., et al., *Vaccination with LAG-3Ig (IMP321) and peptides induces specific CD4 and CD8 T-cell responses in metastatic melanoma patients—*

report of a phase I/IIa clinical trial. Clinical Cancer Research, 2016. **22**(6): p. 1330-1340.

127. Kamphorst, A.O., et al., *Proliferation of PD-1+ CD8 T cells in peripheral blood after PD-1–targeted therapy in lung cancer patients.* Proceedings of the National Academy of Sciences, 2017: p. 201705327.
128. Tumeh, P.C., et al., *PD-1 blockade induces responses by inhibiting adaptive immune resistance.* Nature, 2014. **515**(7528): p. 568-571.
129. Del Monte, U., *Does the cell number 109 still really fit one gram of tumor tissue?* Cell Cycle, 2009. **8**(3): p. 505-506.
130. Coventry, B.J., et al., *CRP identifies homeostatic immune oscillations in cancer patients: a potential treatment targeting tool?* Journal of translational medicine, 2009. **7**(1): p. 102.
131. d'Onofrio, A., et al., *Delay-induced oscillatory dynamics of tumour–immune system interaction.* Mathematical and Computer Modelling, 2010. **51**(5-6): p. 572-591.
132. Joseph, R.W., et al., *Baseline Tumor Size Is an Independent Prognostic Factor for Overall Survival in Patients With Melanoma Treated With Pembrolizumab.* Clinical Cancer Research, 2018: p. clincanres. 2386.2017.
133. Ribas, A., et al., *Association of pembrolizumab with tumor response and survival among patients with advanced melanoma.* Jama, 2016. **315**(15): p. 1600-1609.
134. Eggermont, A.M., et al., *Adjuvant Pembrolizumab versus placebo in resected stage III melanoma.* New England Journal of Medicine, 2018. **378**(19): p. 1789-1801.
135. Beldi-Ferchiou, A. and S. Caillat-Zucman, *Control of NK cell activation by immune checkpoint molecules.* International journal of molecular sciences, 2017. **18**(10): p. 2129.
136. De Coaña, Y.P., et al., *Abstract LB-116: Myeloid derived suppressor cells and NK cells are correlated with clinical benefit and survival in advanced melanoma patients treated with PD-1 blocking antibodies nivolumab and pembrolizumab*. 2018, AACR.
137. Kohn, C.G., et al., *Cost-effectiveness of immune checkpoint inhibition in BRAF wild-type advanced melanoma.* Journal of Clinical Oncology, 2017. **35**(11): p. 1194.
138. Robert, C., et al., *Anti-programmed-death-receptor-1 treatment with pembrolizumab in ipilimumab-refractory advanced melanoma: a randomised dose-comparison cohort of a phase 1 trial.* The Lancet, 2014. **384**(9948): p. 1109-1117.
139. Ribas, A., et al., *Pembrolizumab versus investigator-choice chemotherapy for ipilimumab-refractory melanoma (KEYNOTE-002): a randomised, controlled, phase 2 trial.* The lancet oncology, 2015. **16**(8): p. 908-918.
140. Kitano, S., T. Nakayama, and M. Yamashita, *Biomarkers for immune checkpoint inhibitors in Malignant melanoma.* Frontiers in oncology, 2018. **8**: p. 270.
141. Diem, S., et al., *Serum lactate dehydrogenase as an early marker for outcome in patients treated with anti-PD-1 therapy in metastatic melanoma.* British journal of cancer, 2016. **114**(3): p. 256.

142. Nishino, M., et al., *Immune-Related Tumor Response Dynamics in Melanoma Patients Treated with Pembrolizumab: Identifying Markers for Clinical Outcome and Treatment Decisions.* Clinical Cancer Research, 2017.
143. Breslow, A., *Thickness, cross-sectional areas and depth of invasion in the prognosis of cutaneous melanoma.* Annals of surgery, 1970. **172**(5): p. 902.
144. Morton, D.L., et al., *Multivariate analysis of the relationship between survival and the microstage of primary melanoma by Clark level and Breslow thickness.* Cancer, 1993. **71**(11): p. 3737-3743.
145. Joseph, R.W., et al., *Baseline tumor size as an independent prognostic factor for overall survival in patients with metastatic melanoma treated with the anti-PD-1 monoclonal antibody MK-3475*. 2014, American Society of Clinical Oncology.
146. Wolchok, J.D., et al., *Guidelines for the evaluation of immune therapy activity in solid tumors: immune-related response criteria.* Clinical cancer research, 2009. **15**(23): p. 7412-7420.
147. Hodi, F.S., et al., *Evaluation of immune-related response criteria and RECIST v1. 1 in patients with advanced melanoma treated with pembrolizumab.* Journal of Clinical Oncology, 2016. **34**(13): p. 1510-1517.

List of Figures

List of Tables

Giving of thanks

First and foremost, I am deeply grateful to Markus Morrison and Zvia Agur for mentoring the project and giving me the opportunity to work in an exciting research area. Our many discussions definitely stimulated my scientific curiosity. I am tremendously thankful to Markus for giving me the confidence to freely study and work on my own, but guide me whenever I needed it. The opportunities you provided me were key to my graduate pursuits and successes. I am also thankful to your assistance in publication and dissertation writing. To Zvia, many thanks for providing me the scaffold upon which I have built my scientific knowledge and passion. I acknowledge your help and support in planning and developing the algorithm, as well as your assistance in publication writing.

I want to thank the thesis committee for accepting the review of my dissertation. Special thanks to Thomas Sauter from the University of Luxembourg for the fruitful discussions about Systems Biology, and for accepting the evaluation my dissertation.

I am grateful for the teams of Optimata Ltd and the Institute for Medical Biomathematics (IMBM) for your support and lively conversations on science. Special thanks to Yuri Kogan for participation in the mentoring of the project, the planning and developing of the algorithm, and revising the publications. I acknowledge Marina Kleiman (Optimata Ltd.) for participating in the clinical trial design and execution, and Moran Elishmereni (Optimata Ltd.) for sharing knowledge about parameter estimation techniques. I am also very thankful for the Israel Brain Gain Program of Israel Innovation Authority for connecting me with the MEL PLEX network.

It was a pleasure to work in the supportive environment during my secondments at HMC and UMM. I am incredibly grateful to Michal Lotem from HMC and Jochen Utikal from UMM and the Deutsches Krebsforschungszentrum (DKFZ) for your assistance to receive permission to access to the patient data at HMC and UMM. In addition, many thanks to both of you for your general support during the clinical data collection, and contribution of your clinical knowledge to the data analysis. In addition, my sincerest thanks to Evgenia Avizov-Khodak for performing the tumor size assessments from

imaging scans of the patients at HMC, and Désirée Vaeth and Nils Vogler for performing the tumor size assessments from imaging scans of the patients at UMM. I want to acknowledge and thank Christoffer Gebhardt, and Mirko Gries (UMM) for sharing clinical knowledge. And special thanks to Beate Eisenecker, Christianne Schmidt, Carmen Weiler and Yvonne Nowak (UMM), Tamar Hamburger and Hani Steinberg (HMC) for assisting in the data collection, and for taking good care of me during my secondments.

I am grateful to my friends and colleagues in MEL PLEX for the enriching courses, seminars, conferences and fruitful meetings, as well as the fun adventures and conversations about science and non-science.

My dear family and friends Shraga Tsur, Yuval Tsur, Clemens Schwingshackl, Paul Bauer and Avi Gillis, thanks for proofreading parts of my dissertation, I appreciate it!

Finally, I want to thank my family for your support and belief in me. Ima, Aba, Yuval, Adi, Eyal and Itamar, I am truly lucky because you are my family.